

# Generalized Fourier Analyses of Semi-Discretizations of the Advection-Diffusion Equation<sup>1</sup>

Mark A. Christon and Thomas E. Voth  
Computational Physics R & D Department

Mario J. Martinez  
Multiphase Transport Processes Department

Sandia National Laboratories  
P. O. Box 5800  
Albuquerque, NM 87185-0819

## Abstract

This report presents a detailed multi-methods comparison of the spatial errors associated with finite difference, finite element and finite volume semi-discretizations of the scalar advection-diffusion equation. The errors are reported in terms of non-dimensional phase and group speeds, discrete diffusivity, artificial diffusivity, and grid-induced anisotropy. It is demonstrated that Fourier analysis (aka von Neumann analysis) provides an automatic process for separating the spectral behavior of the discrete advective operator into its symmetric dissipative and skew-symmetric advective components. Further it is demonstrated that streamline upwind Petrov-Galerkin and its control-volume finite element analogue, streamline upwind control-volume, produce both an artificial diffusivity and an artificial phase speed in addition to the usual semi-discrete artifacts observed in the discrete phase speed, group speed and diffusivity. For each of the numerical methods considered, asymptotic truncation error and resolution estimates are presented for the limiting cases of pure advection and pure diffusion. The Galerkin finite element method

---

<sup>1</sup>Keywords and Phrases: Advection-diffusion, phase error, dispersion, discrete diffusivity, artificial viscosity

and its streamline upwind derivatives are shown to exhibit super-convergent behavior in terms of phase and group speed when a consistent mass matrix is used in the formulation. In contrast, the CVFEM method and its streamline upwind derivatives yield strictly second-order behavior. While this work can only be considered a first step in a comprehensive multi-methods analysis and comparison, it serves to identify some of the relative strengths and weaknesses of multiple numerical methods in a common mathematical framework.

## Acknowledgments

The authors would like to acknowledge Tim Trucano and Tom Smith for their helpful comments during the preparation of this report. This work was supported under the ASCI Advanced Spatial Discretization project.

# Contents

<b>Executive Summary</b>	<b>15</b>
<b>1 Introduction</b>	<b>19</b>
<b>2 Formulation Issues</b>	<b>25</b>
2.1 Fourier Analysis . . . . .	27
2.1.1 Preliminaries . . . . .	27
2.1.2 Fourier Analysis and Truncation Error . . . . .	30
2.2 Second-Order Upwind as a Prototype . . . . .	31
2.2.1 Semi-Discrete Equations . . . . .	32
2.2.2 Dispersion Relations . . . . .	33
2.2.3 Discrete Diffusivity . . . . .	41
2.2.4 Artificial Diffusivity . . . . .	42
2.2.5 Effects of Artificial Diffusivity . . . . .	44
2.3 Semi-Discrete Methods Analyzed in this Work . . . . .	48
<b>3 One-Dimensional Results</b>	<b>51</b>
3.1 Phase Speed . . . . .	52
3.2 Group Speed . . . . .	61
3.3 Discrete Diffusivity . . . . .	68
3.4 Artificial Diffusivity . . . . .	71
3.5 Effects of Artificial Diffusivity . . . . .	75
<b>4 Two-Dimensional Results</b>	<b>79</b>
4.1 Metrics . . . . .	79
4.2 Phase Speed . . . . .	82
4.2.1 2D Phase Speed Formulae . . . . .	82
4.2.2 2D Phase Speed Results . . . . .	85
4.3 Discrete Diffusivity . . . . .	99
4.3.1 2D Discrete Diffusivity Formulae . . . . .	99
4.3.2 2D Discrete Diffusivity Results . . . . .	100
4.4 Artificial Diffusivity . . . . .	109
4.4.1 2D Artificial Diffusivity Formulae . . . . .	109

4.4.2	2D Artificial Diffusivity Results . . . . .	111
<b>5</b>	<b>Summary and Conclusions</b>	<b>121</b>
<b>A</b>	<b>Operator Stencils</b>	<b>127</b>
A.1	First-Order Upwind (FOU) . . . . .	127
A.2	Second-Order Central Difference (CD) . . . . .	128
A.3	Second-Order Upwind (SOU) . . . . .	129
A.4	Third-Order Upwind (TOU) . . . . .	130
A.5	Fromm's Method . . . . .	130
A.6	QUICK . . . . .	131
A.7	Node Centered Finite Volume with Least Squares Gradient Reconstruction (LSR) . . . . .	132
A.8	Galerkin Finite Element Method (FEM) . . . . .	133
A.9	Finite Element Method with SUPG (FEM-SUPG) . . . . .	134
A.10	Control Volume Finite Element Method (CVFEM) . . . . .	135
A.11	Control-Volume Finite Element Method with SUCV (CVFEM- SUCV) . . . . .	135
	<b>Bibliography</b>	<b>135</b>

# List of Figures

2.1	Fundamental solution with wavelength $\lambda$ , propagation speed $c$ , wavenumber $k$ , and propagation direction $\theta$ . . . . .	26
2.2	Propagation direction: (a) on a finite difference grid; (b) on a 2x2 patch of a finite element mesh; (c) on a control-volume finite element mesh. . . . .	28
2.3	Non-dimensional phase speed for the second-order upwind method: a) phase vs. non-dimensional wavenumber for $\theta = 0, 22.5, 45, 67.5, 90^\circ$ , b) phase vs. non-dimensional wavenumber and propagation direction (in degrees). . . . .	35
2.4	Component of the group velocity in the $x$ -coordinate direction: a) $\tilde{v}_{gx}$ vs. non-dimensional wavenumber along $\theta = 0, 22.5, 45, 67.5, 90^\circ$ , b) $x$ -velocity component vs. non-dimensional wavenumber and direction (All angles presented in degrees.) . . . . .	37
2.5	Component of the group velocity in the $y$ -coordinate direction: a) $\tilde{v}_{gy}$ vs. non-dimensional wavenumber along $\theta = 0, 22.5, 45, 67.5, 90^\circ$ , b) $y$ -velocity component vs. non-dimensional wavenumber and direction. (All angles presented in degrees.) . . . . .	38
2.6	Snapshots of the temperature profile for the pure advection problem calculated using the skew-symmetric second-order upwind advective operator at a) $t = 0$ , b) $t = 3.75u\Delta t/\Delta x$ , and c) $t = 7.5u\Delta t/\Delta x$ . . . . .	39
2.7	Snapshots of the temperature profile for the pure advection problem calculated using the second-order upwind advective operator at a) $t = 0$ , b) $t = 3.75u\Delta t/\Delta x$ , and c) $t = 7.5u\Delta t/\Delta x$ . . . . .	40
2.8	Group angle, $\Theta$ , for the second-order upwind method. (All angles presented in degrees.) . . . . .	41
2.9	Non-dimensional discrete diffusivity for the second-order upwind method: a) discrete diffusivity vs. non-dimensional wavenumber for $\theta = 0, 22.5, 45, 67.5, 90^\circ$ , b) discrete diffusivity vs. non-dimensional wavenumber and propagation direction. . . . .	43

2.10	Non-dimensional artificial diffusivity for the second-order upwind method: a) artificial diffusivity vs. non-dimensional wavenumber for $\theta = 0, 22.5, 45, 67.5, 90^\circ$ , b) artificial diffusivity vs. non-dimensional wavenumber and propagation direction. . . . .	45
2.11	Non-dimensional quadratic temperature increment for the second-order upwind method: a) quadratic temperature increment vs. non-dimensional wavenumber for $\theta = 0, 22.5, 45, 67.5, 90^\circ$ , b) quadratic temperature increment vs. non-dimensional wavenumber and propagation direction. . . . .	49
3.1	Non-dimensional phase speed for a variety of finite-difference (node-centered finite-volume) methods. . . . .	54
3.2	Non-dimensional phase speed for finite element method with a consistent mass matrix (FEM - $\mathbf{M}_c$ ), lumped mass (FEM - $\mathbf{M}_l$ ), consistent mass matrix and FEM-SUPG with $\beta_{opt}$ and $\beta = 1/2$ . . . . .	55
3.3	Non-dimensional phase speed for control-volume finite element method with a consistent mass matrix (CVFEM - $\mathbf{M}_c$ ), lumped mass (CVFEM - $\mathbf{M}_l$ ), consistent mass matrix and SUCV with $\beta_{opt}$ and $\beta = 1/2$ . . . . .	55
3.4	Non-dimensional phase speed for control-volume finite element and finite element methods using streamline upwinding (CVFEM-SUCV and FEM-SUPG). . . . .	56
3.5	Non-dimensional phase speed for finite element method with a consistent mass matrix and FEM-SUPG with $\beta_{opt}$ for $\mathbf{P}_e = 1, 2, 5, 10, 100$ . . . . .	57
3.6	Non-dimensional phase speed for control-volume finite element method with a consistent mass matrix and SUCV with $\beta = 1/2$ for $\mathbf{P}_e = 1, 2, 5, 10, 100$ . . . . .	57
3.7	Doubly-asymptotic stabilization parameter for FEM-SUPG – see Tezduyar [26]. . . . .	58
3.8	Non-dimensional phase speed for the finite element method with a consistent mass matrix and FEM-SUPG using $\beta_{opt}$ and $\xi = \coth(\mathbf{P}_e) - 1/\mathbf{P}_e$ for $\mathbf{P}_e = 1, 2, 5, 10, 100$ . . . . .	58
3.9	Non-dimensional phase speed for control-volume finite element method with a consistent mass matrix and SUCV with $\beta = 1/2$ and $\xi = \coth(\mathbf{P}_e) - 1/\mathbf{P}_e$ for $\mathbf{P}_e = 1, 2, 5, 10, 100$ . . . . .	59
3.10	Non-dimensional group speed for a variety of finite-difference (node-centered finite-volume) methods. . . . .	63

3.11	Non-dimensional group speed for finite element method using a consistent mass matrix (FEM - $\mathbf{M}_c$ ), lumped mass (FEM - $\mathbf{M}_l$ ), consistent mass matrix and SUPG with $\beta_{opt}$ and $\beta = 1/2$ .	64
3.12	Non-dimensional group speed for finite element method using a consistent mass matrix and SUPG with $\beta_{opt}$ for $\mathbf{P}_e = 1, 2, 5, 10, 100$ .	64
3.13	Non-dimensional group speed for finite element method using a consistent mass matrix and SUPG using $\beta_{opt}$ and $\xi = \coth(\mathbf{P}_e) - 1/\mathbf{P}_e$ for $\mathbf{P}_e = 1, 2, 5, 10, 100$ .	65
3.14	Non-dimensional group speed for control-volume finite element method using a consistent mass matrix (CVFEM - $\mathbf{M}_c$ ), lumped mass (CVFEM - $\mathbf{M}_l$ ), consistent mass matrix and SUCV with $\beta_{opt}$ and $\beta = 1/2$ .	65
3.15	Non-dimensional group speed for control-volume finite element method with a consistent mass matrix and SUCV with $\beta = 1/2$ for $\mathbf{P}_e = 1, 2, 5, 10, 100$ .	66
3.16	Non-dimensional group speed for control-volume finite element method using a consistent mass matrix and SUCV with $\beta = 1/2$ and $\xi = \coth(\mathbf{P}_e) - 1/\mathbf{P}_e$ for $\mathbf{P}_e = 1, 2, 5, 10, 100$ .	66
3.17	Non-dimensional discrete diffusivity for Galerkin finite element (FEM) and control-volume finite element methods (CVFEM).	70
3.18	Non-dimensional discrete diffusivity for FEM with SUPG and CVFEM with SUCV.	70
3.19	Non-dimensional artificial diffusivity for a variety of finite-difference (node-centered finite-volume) methods.	73
3.20	Non-dimensional artificial diffusivity for FEM-SUPG and CVFEM-SUCV.	73
3.21	Non-dimensional change in incremental quadratic temperature, $\Delta QT$ , for a variety of finite-difference (node-centered finite-volume) methods.	76
3.22	Non-dimensional change in incremental quadratic temperature, $\Delta QT$ , for FEM-SUPG and CVFEM-SUCV with $\beta = \beta_{opt}$ and $1/2$ .	77
4.1	Non-dimensional phase speed ( $\tilde{c}/c$ ; radial coordinate) as a function of $\theta$ (azimuthal coordinate).	80
4.2	Non-dimensional phase speed ( $\tilde{c}/c$ ; radial) as a function of $\theta$ (azimuthal) for the consistent mass Galerkin finite element method (FEM - $\mathbf{M}_c$ ) with a) $\gamma = 1$ and b) $\gamma = 1/2$ .	87
4.3	Non-dimensional phase speed ( $\tilde{c}/c$ ; radial) as a function of $\theta$ (azimuthal) for consistent mass matrix finite element method SUPG with $\beta_{opt}$ ; a) $\gamma = 1$ and b) $\gamma = 1/2$ .	88

4.4	Non-dimensional phase speed ( $\tilde{c}/c$ ; radial) as a function of $\theta$ (azimuthal) for consistent mass matrix finite element method SUPG with $\beta = 1/2$ ; a) $\gamma = 1$ and b) $\gamma = 1/2$ . . . . .	88
4.5	Non-dimensional phase speed ( $\tilde{c}/c$ ; radial) as a function of $\theta$ (azimuthal) for the consistent mass control volume finite element method (CVFEM) with a) $\gamma = 1$ and b) $\gamma = 1/2$ . . . .	89
4.6	Non-dimensional phase speed ( $\tilde{c}/c$ ; radial) as a function of $\theta$ (azimuthal) for consistent mass matrix control volume finite element method SUCV with $\beta_{opt}$ ; a) $\gamma = 1$ and b) $\gamma = 1/2$ . . .	89
4.7	Non-dimensional phase speed ( $\tilde{c}/c$ ; radial) as a function of $\theta$ (azimuthal) for consistent mass matrix control volume finite element method SUCV with $\beta = 1/2$ ; a) $\gamma = 1$ and b) $\gamma = 1/2$ . . .	90
4.8	Non-dimensional phase speed ( $\tilde{c}/c$ ; radial) as a function of $\theta$ (azimuthal) for the central difference method (also FOU). Results for aspect ratios of a) $\gamma = 1$ and b) $\gamma = 1/2$ are shown. . . . .	90
4.9	Non-dimensional phase speed ( $\tilde{c}/c$ ; radial) as a function of $\theta$ (azimuthal) for the consistent mass matrix central difference discretization (CD- $\mathbf{M}_c$ ). Results for aspect ratios of a) $\gamma = 1$ and b) $\gamma = 1/2$ are shown. . . . .	91
4.10	Non-dimensional phase speed ( $\tilde{c}/c$ ; radial) as a function of $\theta$ (azimuthal) for the second-order upwind finite difference discretization (SOU). Results are shown for aspect ratios of a) $\gamma = 1$ and b) $\gamma = 1/2$ . . . . .	91
4.11	Non-dimensional phase speed ( $\tilde{c}/c$ ; radial) as a function of $\theta$ (azimuthal) for the finite difference discretization with third-order-upwind differencing. Results for aspect ratios of a) $\gamma = 1$ and b) $\gamma = 1/2$ are shown. . . . .	92
4.12	Non-dimensional phase speed ( $\tilde{c}/c$ ; radial) as a function of $\theta$ (azimuthal) for Fromm's method. Results for a) $\gamma = 1$ and b) $\gamma = 1/2$ are shown. . . . .	92
4.13	Non-dimensional phase speed ( $\tilde{c}/c$ ; radial) as a function of $\theta$ (azimuthal) for the QUICK scheme with a) $\gamma = 1$ and b) $\gamma = 1/2$ . . . . .	93
4.14	Non-dimensional phase speed ( $\tilde{c}/c$ ; radial) as a function of $\theta$ (azimuthal) for the node-centered finite volume method with least squares gradient reconstruction ( $\theta = 1.$ , $\kappa = 0$ ) with a) $\gamma = 1$ and b) $\gamma = 1/2$ . . . . .	93
4.15	Non-dimensional phase speed ( $\tilde{c}/c$ ; radial) as a function of $\theta$ (azimuthal) for the node-centered finite volume method with least squares gradient reconstruction ( $\theta = 1.$ , $\kappa = -1$ )) with a) $\gamma = 1$ and b) $\gamma = 1/2$ . . . . .	94



4.16	Non-dimensional discrete diffusivity for the consistent mass Galerkin finite element method with a) $\gamma = 1$ and b) $\gamma = 1/2$ .	101
4.17	Non-dimensional discrete diffusivity ( $\tilde{\alpha}/\alpha$ ; radial) as a function of $\theta$ (azimuthal) for consistent mass matrix finite element method SUPG with $\beta_{opt}$ with a) $\gamma = 1$ and b) $\gamma = 1/2$ . . . . .	102
4.18	Non-dimensional discrete diffusivity ( $\tilde{\alpha}/\alpha$ ; radial) as a function of $\theta$ (azimuthal) for consistent mass matrix finite element method SUPG with $\beta = 1/2$ with a) $\gamma = 1$ and b) $\gamma = 1/2$ . . . . .	102
4.19	Non-dimensional discrete diffusivity for the consistent mass control volume finite element method with a) $\gamma = 1$ and b) $\gamma = 1/2$ . . . . .	103
4.20	Non-dimensional discrete diffusivity ( $\tilde{\alpha}/\alpha$ ; radial) as a function of $\theta$ (azimuthal) for consistent mass matrix control volume finite element method SUCV with $\beta_{opt}$ with a) $\gamma = 1$ and b) $\gamma = 1/2$ . . . . .	103
4.21	Non-dimensional discrete diffusivity ( $\tilde{\alpha}/\alpha$ ; radial) as a function of $\theta$ (azimuthal) for consistent mass matrix control volume finite element method SUCV with $\beta = 1/2$ with a) $\gamma = 1$ and b) $\gamma = 1/2$ . . . . .	104
4.22	Non-dimensional discrete diffusivity for the finite difference method with first-order upwind and aspect ratios of a) $\gamma = 1$ and b) $\gamma = 1/2$ . . . . .	104
4.23	Non-dimensional discrete diffusivity ( $\tilde{\alpha}/\alpha$ ; radial) as a function of $\theta$ (azimuthal) for the node-centered finite volume method with second order gradient approximation and consistent mass matrix with a) $\gamma = 1$ and b) $\gamma = 1/2$ . . . . .	105
4.24	Non-dimensional artificial diffusivity ( $1/\mathbf{P}_e^{art}$ ; radial) as a function of $\theta$ (azimuthal) for consistent mass matrix finite element method SUPG with $\beta_{opt}$ with a) $\gamma = 1$ and b) $\gamma = 1/2$ . . . . .	112
4.25	Non-dimensional artificial diffusivity ( $1/\mathbf{P}_e^{art}$ ; radial) as a function of $\theta$ (azimuthal) for consistent mass matrix finite element method SUPG with $\beta = 1/2$ with a) $\gamma = 1$ and b) $\gamma = 1/2$ . . . . .	113
4.26	Non-dimensional artificial diffusivity ( $1/\mathbf{P}_e^{art}$ ; radial) as a function of $\theta$ (azimuthal) for consistent mass matrix control volume finite element method SUCV with $\beta_{opt}$ with a) $\gamma = 1$ and b) $\gamma = 1/2$ . . . . .	113
4.27	Non-dimensional artificial diffusivity ( $1/\mathbf{P}_e^{art}$ ; radial) as a function of $\theta$ (azimuthal) for consistent mass matrix control volume finite element method SUCV with $\beta = 1/2$ with a) $\gamma = 1$ and b) $\gamma = 1/2$ (right). . . . .	114

4.28	Non-dimensional artificial diffusivity ( $1/\mathbf{P}_e^{art}$ ; radial) as a function of $\theta$ (azimuthal) for the first-order upwind (FOU) semi-discretization. Results for aspect ratios of a) $\gamma = 1$ and b) $\gamma = 1/2$ are shown. . . . .	114
4.29	Non-dimensional artificial diffusivity ( $1/\mathbf{P}_e^{art}$ ; radial) as a function of $\theta$ (azimuthal) for the second-order upwind (SOU) semi-discretization. Results are shown for a) $\gamma = 1$ and b) $\gamma = 1/2$ . . . . .	115
4.30	Non-dimensional artificial diffusivity ( $1/\mathbf{P}_e^{art}$ ; radial) as a function of $\theta$ (azimuthal) for the third-order upwind (TOU) semi-discretization. Results are shown for a) $\gamma = 1$ and b) $\gamma = 1/2$ . . . . .	116
4.31	Non-dimensional artificial diffusivity ( $1/\mathbf{P}_e^{art}$ ; radial) as a function of $\theta$ (azimuthal) for Fromm's method. Results for a) $\gamma = 1$ and b) $\gamma = 1/2$ are shown. . . . .	116
4.32	Non-dimensional artificial diffusivity ( $1/\mathbf{P}_e^{art}$ ; radial) as a function of $\theta$ (azimuthal) for the QUICK semi-discretization. Results for a) $\gamma = 1$ and b) $\gamma = 1/2$ are shown. . . . .	117
4.33	Non-dimensional artificial diffusivity ( $1/\mathbf{P}_e^{art}$ ; radial) as a function of $\theta$ (azimuthal) for the least squares reconstruction (LSR(0); $\theta = 1$ , $\kappa = 0$ ). Results for a) $\gamma = 1$ and b) $\gamma = 1/2$ are shown. . . . .	117
4.34	Non-dimensional artificial diffusivity ( $1/\mathbf{P}_e^{art}$ ; radial) as a function of $\theta$ (azimuthal) for the least squares reconstruction (LSR(-1); $\theta = 1$ , $\kappa = -1$ ). Results for a) $\gamma = 1$ and b) $\gamma = 1/2$ are shown. . . . .	118

# List of Tables

3.1	Mass matrix contribution for FEM and CVFEM methods where $\mathbf{M}_l$ indicates a lumped mass matrix and $\mathbf{M}_c$ indicates a consistent mass matrix. . . . .	52
3.2	Formulae for one-dimensional phase speed. . . . .	53
3.3	Asymptotic estimates of truncation error and resolution requirements based on the phase error for pure advection. (Note that the FEM-SUPG and CVFEM-SUCV results are presented only for a consistent mass matrix $\mathbf{M}_c$ .) . . . . .	61
3.4	Formulae for one-dimensional group speed. . . . .	63
3.5	Asymptotic estimates of truncation error and resolution requirements based on the group error for pure advection. (Note that the SUPG and SUCV results are presented only for a consistent mass matrix $\mathbf{M}_c$ .) . . . . .	68
3.6	Formulae for one-dimensional discrete diffusivity. . . . .	69
3.7	Asymptotic estimates of truncation error and resolution requirements based on the discrete diffusivity for thermal diffusion. . . . .	71
3.8	Formulae for one-dimensional artificial diffusivity. . . . .	72
3.9	Asymptotic estimates of truncation error for artificial diffusivity. . . . .	75
4.1	Coefficient of Variation of phase speed, $\varsigma_{\bar{c}}$ , as a function of $2\Delta x/\lambda$ , and its average, $\overline{\varsigma_{\bar{c}}}$ , for the two-dimensional, $\gamma = 1$ semi-discretizations. . . . .	95
4.2	Coefficient of Variation of phase speed, $\varsigma_{\bar{c}}$ , as a function of $2\Delta x/\lambda$ , and its average, $\overline{\varsigma_{\bar{c}}}$ , for the two-dimensional, $\gamma = 1/2$ semi-discretizations. . . . .	96
4.3	RMS error of discrete phase speed, $\varepsilon_{\bar{c}}$ , as a function of $2\Delta x/\lambda$ , and its average, $\overline{\varepsilon_{\bar{c}}}$ , for the two-dimensional, $\gamma = 1$ semi-discretizations. . . . .	97
4.4	RMS error of discrete phase speed, $\varepsilon_{\bar{c}}$ , as a function of $2\Delta x/\lambda$ , and its average, $\overline{\varepsilon_{\bar{c}}}$ , for the two-dimensional, $\gamma = 1/2$ semi-discretizations. . . . .	98

4.5	Coefficient of Variation of discrete diffusivity, $\varsigma_{\tilde{\alpha}}$ , as a function of $2\Delta x/\lambda$ , and its average, $\overline{\varsigma_{\tilde{\alpha}}}$ , for the two-dimensional, $\gamma = 1$ , semi-discretizations considered here. . . . .	106
4.6	Coefficient of Variation of discrete diffusivity, $\varsigma_{\tilde{\alpha}}$ , as a function of $2\Delta x/\lambda$ , and its average, $\overline{\varsigma_{\tilde{\alpha}}}$ , for the two-dimensional, $\gamma = 1/2$ semi-discretizations considered here. . . . .	107
4.7	RMS discrete diffusivity error, $\varepsilon_{\tilde{\alpha}}$ , as a function of $2\Delta x/\lambda$ , and its average, $\overline{\varepsilon_{\tilde{\alpha}}}$ , for the two-dimensional, $\gamma = 1$ semi-discretizations considered here. . . . .	107
4.8	RMS discrete diffusivity error, $\varepsilon_{\tilde{\alpha}}$ , as a function of $2\Delta x/\lambda$ , and its average, $\overline{\varepsilon_{\tilde{\alpha}}}$ , for the two-dimensional, $\gamma = 1/2$ semi-discretizations considered here. . . . .	108
4.9	Coefficient of Variation of $1/\mathbf{P}_e^{art}$ , $\varsigma_{art}$ , as a function of $2\Delta x/\lambda$ , and its average, $\overline{\varsigma_{art}}$ , for the two-dimensional, $\gamma = 1$ semi-discretizations considered here. . . . .	118
4.10	Coefficient of Variation of $1/\mathbf{P}_e^{art}$ , $\varsigma_{art}$ , as a function of $2\Delta x/\lambda$ , and its average, $\overline{\varsigma_{art}}$ , for the two-dimensional, $\gamma = 1/2$ semi-discretizations considered here. . . . .	119
4.11	RMS value of $1/\mathbf{P}_e^{art}$ , $\varepsilon_{art}$ , as a function of $2\Delta x/\lambda$ , and its average, $\overline{\varepsilon_{art}}$ , for the two-dimensional $\gamma = 1$ semi-discretizations considered here. . . . .	119
4.12	RMS value of $1/\mathbf{P}_e^{art}$ , $\varepsilon_{art}$ , as a function of $2\Delta x/\lambda$ , and its average, $\overline{\varepsilon_{art}}$ , for the two-dimensional, $\gamma = 1/2$ semi-discretizations. . . . .	120

## Executive Summary

In recent years, there has been a significant shift toward simulation-based design and away from test-based design and development procedures. As a consequence, the accuracy with which numerical methods can simulate physical processes such as fluid flow and material deformation has become the topic of a great deal of speculation and debate. The fact that there are a large number of competing numerical methods (and zealots for these methods) has only served to obfuscate an already confusing picture of numerical methods and their true abilities to simulate complex physical phenomena.

In order to understand the differences between numerical methods, a direct side-by-side comparison of each method on a select number of problems is possible, but the investment in manpower to effect such a comparison is prohibitive. There are also deep questions surrounding the choice of comparison problems and the scientific implications (or lack thereof) of such comparisons. This is further complicated by differences in formulations, i.e., some methods are based on Taylor series, while most weighted residual methods (e.g., finite element methods) are not subservient to Taylor series.

In the work reported here, we use a generalized Fourier analysis to place all methods on an equal theoretical footing to perform a comparison that is independent of Taylor series, specific error norms, choices in grids, and data smoothness. This effort constitutes a *first step* in a multi-methods comparison, and is intended to identify some of the relative strengths and weaknesses of multiple numerical methods in the context of time-dependent advection-diffusion. This problem class was selected because it represents a fundamental building-block required to assemble more complicated solution methods for nonlinear problems such as high-Reynolds number, time-dependent, viscous flow.

The results of this *first step* show that:

- There are a number of competing methods that are all of second-order accuracy or better and that should perform adequately in the hands of an experienced analyst. However, the grid resolution requirements to attain a certain level of error among these methods can be vastly different.
- There is no *single* best method, but there are at least two methods that are clearly the worst. The first-order upwind method is excessively diffusive, while the second-order upwind method is extremely dispersive – of which both results are well known to experienced numerical analysts.
- The Galerkin finite element method and its streamline-upwind derivatives exhibit remarkable super-convergent behavior in terms of phase

and group accuracy, i.e., the ability to accurately propagate waves at the correct speed and in the correct direction.

- Analysis of several control-volume finite element methods and their streamline-upwind derivatives revealed that their behavior is strictly second-order resulting in more than double the resolution requirements of the finite element method for an equivalent 1% error in phase and group speed.

The work presented here will permit other analyses and comparisons that we have not carried out. In addition, we hope that this work will be useful in a number of ways – a few of which are outlined here.

- In the selection of numerical solution methods based on specific desired performance characteristics, e.g., non-dispersive, high-phase accuracy, or minimal dissipation, this report may be used as a reference for a wide variety of methods.
- The results found here may also be used to understand the benefits of certain formulation aspects, e.g., the spatial coupling of time derivatives that yields super-convergent phase and group accuracy, which will hopefully yield refined numerical methods.
- For the analyst performing computations, the results found here may be used as a guide in determining bounding limits on the grid resolution required to obtain an accurate solution, i.e., calculating grid budgets. Resolution requirements from 1-D analyses are provided; the 2-D dispersion formulae could also be used to compute full 2-D grid resolution requirements in terms of wavenumber and flow orientation. Alternatively, the 1-D estimates may be used to bound both 2-D and 3-D grid resolution requirements for a desired accuracy.
- For developers of sub-grid scale models, the spectral characterization of phase and group errors as well as artificial diffusivity will hopefully lead to the understanding that connecting such models at the  $2\Delta x$  limit, i.e., the Nyquist limit, of the grid is likely to introduce significant errors.
- In terms of verification of new and existing codes, this report provides detailed data that can be used in checking the behavior of codes, understanding and interpreting their limiting behavior, and in defining well-designed numerical verification experiments that respect the limitations of finite grid resolution.
- This report also identifies fundamental error modes, i.e., the wavelength dependent behavior of discrete wave propagation and diffusion

processes that are typically ignored in traditional computational model uncertainty quantification. It is hoped that, in the future, these error modes will be accounted for directly in uncertainty quantification since their behavior is well characterized here.





# Chapter 1

## Introduction

The evolution of numerical methods for the solution of partial differential equations has come to the point where the end-user is faced with choosing from a plethora of formulations, each with its own strengths and weaknesses. A developer embarking on a new code effort is faced with choosing between structured or unstructured methods, mesh-full or mesh-free, finite element or finite volume. In order to understand the differences and similarities between competing methods, an initiative to perform a multi-methods comparison based on numerical and computational performance has been launched.

Numerical performance is a broad term, and is defined here to include the following: truncation error, consistency and stability, rate of convergence, and dispersive and diffusive character. In contrast, computational performance attempts to quantify the computational efficiency, sequential scaling (computational complexity), compatibility with unstructured grid data structures, and spatial adaptivity. Limitations in numerical methods, particularly for computational fluid dynamics (CFD), are related to the dispersion and dissipation introduced by the numerical scheme.

This work constitutes a *first step* in a multi-methods comparison, and is intended to identify some of the relative strengths and weaknesses of multiple numerical methods in the context of advective-diffusive processes. This problem class has been selected because it constitutes the primary component required to assemble more complicated solution methods for nonlinear problems such as high-Reynolds number, time-dependent, viscous flow.

As the starting point for a multi-methods comparison, a generalized Fourier analysis (also referred to as von Neumann analysis) is used to assess errors in the advective phase and group speed and discrete diffusivity. The analysis provides a convenient mechanism to identify any artificial diffusivity introduced by the spatial discretization and also to quantify its spectral behavior. In addition, the asymptotic behavior of the phase speed and discrete diffusivity provide estimates of the truncation error. While a gener-

alized Fourier analysis is considered only a starting point, it was chosen as the starting point because it provides a suitable means for assessing multiple numerical methods on a relatively equal theoretical footing.

For this effort, a variety of finite difference, finite volume and finite element methods are considered. Each method is considered on both one-dimensional and two-dimensional periodic Cartesian grids. In this limit, several of the node-centered finite volume methods yield equivalent finite difference schemes. For the ensuing analysis, attention has been restricted to the following advective schemes: first through third-order upwind, second-order centered, QUICK, and Fromm's method. Here, Fromm's method is considered in a semi-discrete form, i.e., in the limit as  $\Delta t \rightarrow 0$ , for the purposes of analysis rather than in its original fractional-step form[9]. For the finite element methods both Galerkin (FEM) and streamline-upwind Petrov-Galerkin (FEM-SUPG) formulations are considered. The finite volume methods include the control-volume finite element method (CVFEM) with and without the stream-line upwind analogue of SUPG known as SUCV (CVFEM-SUCV)[24, 25]. In addition, two finite volume schemes derived using least squares gradient reconstruction (LSR) are also considered.

The results of the Fourier analysis will be used to show that 1) the advective and diffusive parts of the problem can be considered independently except where FEM-SUPG and CVFEM-SUCV methods are concerned, 2) Fourier analysis provides the means to automatically segregate the advective operators into skew-symmetric (non-dissipative) and symmetric (dissipative) components, and 3) resolution estimates for a given accuracy may be set based on the dispersive or the diffusion errors. Ultimately, consideration of the wavelength dependent behavior of upwind advective algorithms should be viewed with an eye toward developing more accurate methods.

## Historical Perspective

Before proceeding with a discussion of the numerical analysis, a brief historical review of investigations into the dispersive errors associated with discrete solution methods is presented. In general, the application of discrete methods to hyperbolic partial differential equations, e.g., pure advection, can result in solutions that are dispersive even though the physical model for wave propagation is non-dispersive. Dispersion errors are typically characterized by the differences between the apparent, i.e., numerical, phase and group speed of waves and their exact counterparts. Phase and group speed errors represent some of the most constraining numerical errors associated with the simulation of advection dominated processes.

In contrast to the phase speed, the group speed describes the propagation of wave packets that are comprised of short wavelength signals modulating

a slowly varying, longer wavelength envelope. Because the energy associated with a wave packet travels with the packet, the group speed is often referred to as the “energy” velocity. The group speed is also referred to as the speed of modulation. For a non-dispersive medium the phase and group speed are identical.

In discrete advection, the group speed may be used to study and explain the propagation of short wavelength signals that are typically  $2\Delta x$  in wavelength where  $\Delta x$  is the characteristic mesh spacing. Vichnevetsky [33, 30, 31] has demonstrated that spurious  $2\Delta x$  oscillations, that are induced by rapid changes in mesh resolution and at physical boundaries, propagate at a group speed associated with a  $2\Delta x$  wavelength.

The accurate simulation of advection dominated processes using discrete numerical schemes hinges upon having a clear understanding of the constraining numerical errors, and sufficient computational resources to effect solutions at the requisite grid scale. Examples of this may be seen when attempting to compute turbulent flow fields via direct numerical simulation (DNS) or large eddy simulation (LES). Controlling the dispersive errors, i.e., phase speed error, to within 5% for a first-order hyperbolic equation requires approximately 11 to 12 cells per wavelength when using traditional finite difference or lumped-mass finite element methods (see Table 2.6.2 in Gresho and Sani [11]). Thus, the simulation of advection dominated problems is limited by the wavelength that the grid can accurately represent. A failure to respect the so-called grid Nyquist limit can introduce deleterious aliasing effects that corrupt the simulation fidelity.

In contrast to the phase and group errors, the application of a discrete method to the diffusive side of the advection-diffusion equation results in a discrete diffusivity that is not equivalent to the prescribed diffusivity in the partial differential equation. The discrete diffusivity exhibits wavelength dependent behavior, and in multiple dimensions is directionally dependent.

The use of a generalized Fourier analysis to assess dispersive and diffusive errors is not new and has been used by numerous researchers to characterize the performance of numerical methods. The effects of consistent, lumped and higher-order mass matrices on the phase speed for linear and quadratic finite elements were investigated by Belytschko and Mullen [4] for linear elastic wave propagation in one dimension. Here, it was verified that the period elongation errors associated with a trapezoidal rule time integrator can be nearly matched with the leading phase errors introduced by a consistent mass matrix. Similarly, the period shortening associated with central differences in time can be matched with the lagging phase errors associated with mass lumping for linear elements. This compensatory interaction between the time integrator and mass matrix yielded the class of methods typically referred to as “matched” methods found in many explicit solid dynamics codes today.

Vichnevetsky et al. [36, 35, 31] have investigated the dispersive nature of both finite difference and finite element methods for the first-order wave equation. In Reference [34], the dispersive errors introduced by nonuniform grid spacing and “hard” boundaries are discussed, and the possibility of using artificial viscosity to damp short wavelength spurious waves is investigated. Similar analysis techniques have been applied to wave propagation in periodic domains [32]. Trefethen [28] has considered the role of group velocity in understanding the propagation of wave packets, the generation of parasitic waves at interfaces, and stability. Here, the influence of group velocity in two-dimensional finite difference discretizations with uniform aspect ratio was considered. Karni [16] has characterized the group speed errors associated with symmetric upwind schemes for pure advection, i.e., a first order wave equation.

Fourier analysis has also been applied to finite element discretizations in order to understand the dispersive nature of elastic wave propagation in bars and locking phenomena in beams [20]. This analysis technique was applied by Park and Flaggs [21] in an effort to understand and ameliorate locking phenomena in  $C^0$  plate elements. Alvin and Park [1] have also used Fourier analysis to tailor the frequency response of beams and bars discretized with the finite element method.

More recently, Shakib and Hughes [23] have applied Fourier analysis to the space-time Galerkin least-squares method for advection-diffusion problems. Harari [14] presents the phase error associated with the Galerkin least-squares discretization for the second-order wave equation in a finite domain. Deville and Mund [8] have used Fourier analysis to investigate the spectral behavior of the iteration matrix for finite element preconditioning. Thompson and Pinsky [27] extended the concepts of Fourier analysis in order to treat p-version finite element discretizations. This work provides practical guidelines for the number of elements per wavelength in terms of the spectral order. Similarly, Grosh and Pinsky [13] have applied Fourier dispersion analysis to fluid loaded plates for structural acoustics simulations. Christon [6] considered the influence of the finite element mass matrix on the dispersion characteristics of second-order wave equation for acoustic fluid-structure interaction. Christon and Voth [37, 7] have applied von Neumann analyses to assess the numerical performance of reproducing kernel semi-discretizations in one and two-dimensions and considered both hyperbolic and parabolic partial differential equations.

In the ensuing discussion, the Formulation section presents an overview of the generalized Fourier analysis used in this study to compute the phase and group speed, discrete and artificial diffusivity, and truncation error for the semi-discretizations. In the subsequent sections, the phase and group speed, discrete diffusivity, and artificial diffusivity results are presented for

the finite element, control-volume finite element, and finite difference/volume semi-discretizations, in one and two dimensions, respectively. Finally, the results of the analysis are summarized and conclusions are outlined.



# Chapter 2

## Formulation Issues

The comparison of numerical methods can be based on a number of metrics such as truncation error, rate of convergence, and dispersive and diffusive behavior. Such a comparison between dissimilar methods is difficult because it may not be possible to select criteria that “fairly” represent each method. For example, the best way to compare finite difference methods that are based on Taylor series with finite element methods that may be best represented by errors measured in the energy norm is an open question.

As a first step in this multi-methods analysis and comparison, we chose to apply Fourier analysis because it provides a general methodology that is capable of analyzing multiple methods in a single mathematical framework while providing a great deal of information and insight into each method. In this work, we use Fourier analysis to probe the following aspects of each method:

- numerical dispersion, i.e., phase and group velocity errors,
- apparent, i.e., discrete, diffusivities that are wavelength dependent – spatial discretization introduces this often-ignored error, even though many schemes are under-diffusive at short-wavelengths,
- the limiting behavior of short wavelength information for both wave propagation and diffusion,
- the identification and characterization of artificial diffusivity introduced via upwinding,
- grid bias errors in phase, group, discrete diffusivity and artificial diffusivity, and
- asymptotic convergence properties and resolution requirements.

Here, Fourier analysis provides the ability to identify and characterize the artificial diffusivity of upwind methods because it automatically segregates the discrete advection operators into symmetric and skew-symmetric parts. In addition, this technique also provides insight into the asymptotic convergence of the methods without the ambiguities associated with the choice of a single norm for multiple methods.

Fourier analysis can be applied to spatially-discrete, temporally-discrete, and fully-discrete (space and time are both discrete) systems. For our purposes, we chose to consider the one- and two-dimensional semi-discrete equations which correspond to the fully-discrete situation in the limit as  $\Delta t \rightarrow 0$ . The analysis proceeds by choosing either an infinite computational domain or alternatively a periodic domain. A fundamental solution to the continuous problem is selected for a fixed wavenumber or wavelength and placed on the computational domain as shown in Figure 2.1. In general, the wave number vector  $\mathbf{k}$  and velocity vector  $\mathbf{c}$  need not be aligned, but to simplify our analysis, we assume the wave vector and velocity vector are aligned.

The response of the discrete system, discretized via finite differences, finite elements, etc., may then be computed in terms of the grid aspect ratio, mesh resolution, wavenumber, propagation speed and direction. The response of the discrete system is wavelength dependent, and is used to identify and characterize the phase and group speed, discrete thermal diffusivity, artificial diffusivity, grid bias, and asymptotic convergence rates.

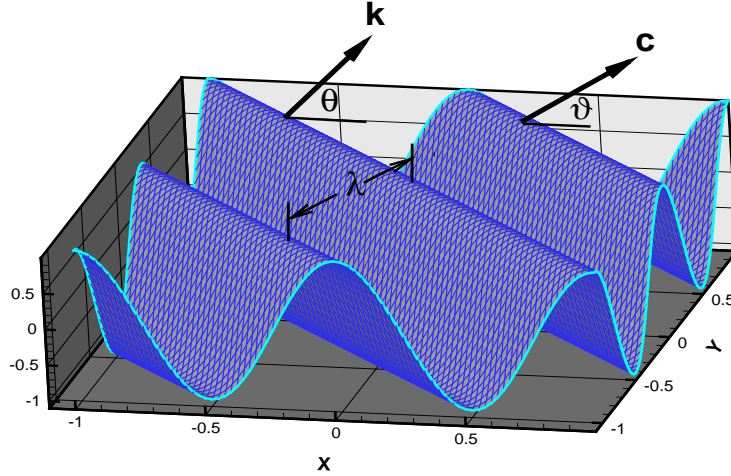


Figure 2.1: Fundamental solution with wavelength  $\lambda$ , propagation speed  $c$ , wavenumber  $k$ , and propagation direction  $\theta$ .



## 2.1 Fourier Analysis

The starting point for the Fourier analysis is the linear advection-diffusion equation,

$$\frac{\partial T}{\partial t} + \mathbf{c} \cdot \nabla T = \alpha \nabla^2 T. \quad (2.1)$$

Here,  $T$  is the temperature (or any other passive scalar),  $\mathbf{c} = u\hat{i} + v\hat{j}$  is the prescribed advective velocity,  $\hat{i}$  and  $\hat{j}$  are unit vectors in the  $x$  and  $y$ -coordinate directions respectively, and  $\alpha$  is the thermal diffusivity. The advective velocity field is assumed to be div-free, i.e.,  $\nabla \cdot \mathbf{c} = 0$ , in both the continuous and discrete sense. For the ensuing analysis, both the advective velocity and thermal diffusivity are constant.

The semi-discrete form of Eq. (2.1) is required for the Fourier analysis and is written as

$$\mathbf{M}\dot{T} + \mathbf{A}(c)T + \mathbf{K}T = 0, \quad (2.2)$$

where  $\mathbf{M}$  is a generalized unit-mass matrix,  $\mathbf{A}(c)$  is the advection operator, and  $\mathbf{K}$  is the diffusivity operator.

For a typical finite-difference method, the generalized unit-mass matrix is simply the identity matrix,  $\mathbf{I}$ , and  $\mathbf{K}$  is the standard five-point difference representation of the Laplacian operator (cf. Eq. (A.3)). For the upwind methods, the advective operator and mass matrix vary according to the specific scheme under consideration.

For the finite element method, the generalized unit-mass matrix is

$$\mathbf{M} = \phi \mathbf{M}_c + (1 - \phi) \mathbf{M}_l, \quad (2.3)$$

where  $\mathbf{M}_c$  is the consistent mass matrix,  $\mathbf{M}_l$  is the row-sum lumped (diagonal) mass matrix, and  $0 \leq \phi \leq 1$ . The details for obtaining the weak form of the advection-diffusion equation and the associated mass, advection and diffusion operators are well known (see for example Gresho and Sani [11]), and are not repeated here. Appendix A lists the stencils for the various methods analyzed in this work.

### 2.1.1 Preliminaries

In the ensuing analysis, a “regular” Cartesian grid is considered where the mesh spacing in the  $x$  and  $y$ -coordinate directions is  $\Delta x$  and  $\Delta y$  respectively. This is illustrated in Figure 2.2a for a five-point finite difference stencil, Figure 2.2b for a patch of four quadrilateral finite elements, and Figure 2.2c for control-volume finite elements. The wave propagation direction is denoted by  $\theta$ , and the nodal  $x$  and  $y$  locations are given by  $x_m = m\Delta x$ , and  $y_n = n\Delta y$ , with the aspect ratio,  $\gamma = \Delta y/\Delta x$ . The spatial domain is considered to be finite with periodic boundary conditions.

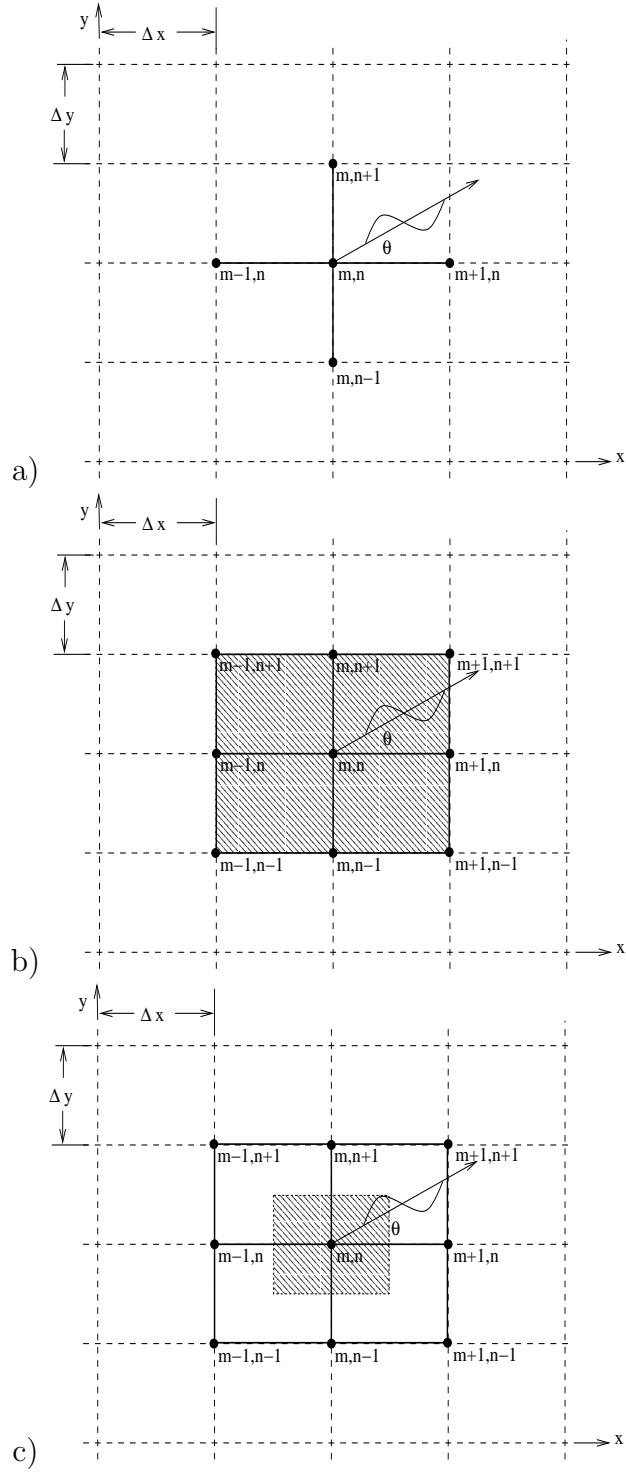


Figure 2.2: Propagation direction: (a) on a finite difference grid; (b) on a 2x2 patch of a finite element mesh; (c) on a control-volume finite element mesh.

By casting the semi-discrete equations on a Cartesian grid, the mass, advection and diffusivity matrices have a banded structure where the non-zero entries in the matrices are equal along lines parallel to the main diagonal, i.e., they are Toeplitz matrices.

Proceeding with the analysis, we begin with a pure advection problem where

$$\mathbf{M} \left\{ \frac{dT}{dt} \right\} + \mathbf{A}(c)T = 0, \quad (2.4)$$

and, consider a sinusoidal trial solution of the form

$$T_{k,(m,n)}(t) = \hat{T}_k(t) \exp[\iota \mathbf{k} \cdot \mathbf{x}_{(m,n)}], \quad (2.5)$$

where  $\mathbf{k}$  is the wave number vector,  $k = \|\mathbf{k}\|$  is the wave number,  $\mathbf{x}_{(m,n)} = x_m \hat{i} + y_n \hat{j}$ , and  $\iota = \sqrt{-1}$ . Here,  $(m, n)$  corresponds to the grid location at  $x_m = m\Delta x$  and  $y_n = n\Delta y$ . This is a solution to Eq. (2.4) provided that

$$\frac{d\hat{T}_k}{dt} = \hat{A}(k)\hat{T}_k, \quad (2.6)$$

where  $\hat{A}(k)$  is the symbol (also referred to as the spectrum) and is defined here as

$$\hat{A}(k) = \frac{-\mathbf{A}(c) \cdot \exp[\iota \mathbf{k} \cdot \mathbf{x}_{(m,n)}]}{\mathbf{M} \cdot \exp[\iota \mathbf{k} \cdot \mathbf{x}_{(m,n)}]}, \quad (2.7)$$

where  $\mathbf{A}(c)$  and  $\mathbf{M}$  are square matrices suitably arranged to multiply the vector,

$$\begin{aligned} \exp[\iota \mathbf{k} \cdot \mathbf{x}_{(m,n)}] &= [\exp[\iota \mathbf{k} \cdot \mathbf{x}_{(1,1)}], \exp[\iota \mathbf{k} \cdot \mathbf{x}_{(2,1)}] \dots, \\ &\exp[\iota \mathbf{k} \cdot \mathbf{x}_{(M,1)}], \dots, \exp[\iota \mathbf{k} \cdot \mathbf{x}_{(1,N)}], \dots, \exp[\iota \mathbf{k} \cdot \mathbf{x}_{(M,N)}]]^T, \end{aligned} \quad (2.8)$$

and  $M$  and  $N$  are the number of grid points in the x- and y-directions respectively.

As noted by Vichnevetsky[33],  $\exp[\iota \mathbf{k} \cdot \mathbf{x}_{(m,n)}]$  are the eigenvectors of the discrete Toeplitz operator  $\mathbf{M}^{-1} \cdot \mathbf{A}(c)$ , and  $\hat{A}(k)$  are the corresponding eigenvalues.

The solution to Eq. (2.4), found by direct integration, is

$$T_{k,(m,n)}(t) = \hat{T}_k(0) \exp[Re(\hat{A}(k))t] \exp[\iota \{\mathbf{k} \cdot \mathbf{x}_{(m,n)} + Im(\hat{A}(k))t\}]. \quad (2.9)$$

where  $Re(\hat{A})$  is the real part of the symbol, and  $Im(\hat{A})$  is the imaginary part. A similar equation is true for the continuous advection equation. So, as demonstrated by Vichnevetsky[33], the sinusoidal trial solutions, with the proper time-dependent coefficients, are solutions to both the semi-discrete and continuous equations. Based on this fact, the difference between the

continuous and semi-discrete solutions may be compared one wave number at a time in order to assess the artifacts introduced by the spatial discretization.

For the pure advection problem, there are two effects to be considered: dissipation and dispersion. The semi-discrete solution does not decay with time if

$$|\hat{T}_k(t)| = |\hat{T}_k(0)| \exp[\operatorname{Re}(\hat{A}(k))], \quad (2.10)$$

which can only be true if  $\operatorname{Re}(\hat{A}(k)) = 0$ . In this situation, the semi-discretization is said to be *energy conserving*. This is the case when  $\mathbf{A}(c)$  is skew-symmetric and  $\mathbf{M}$  is symmetric, although, it is only necessary that  $\mathbf{A}(c)$  be anti-symmetric and  $\mathbf{M}$  symmetric. In either case, when the amplitudes of the signal do not decay with time, the semi-discretization is also referred to as *neutrally dissipative*.

In contrast, there is amplitude decay when at least some of the real eigenvalues are negative. That is, if  $\operatorname{Re}(\hat{A}(k)) \leq 0$  for all  $k$ , and  $\operatorname{Re}(\hat{A}(k)) < 0$  for some of  $k$ , then the amplitudes of the solution will decay in time, and the semi-discretization is *dissipative*. The introduction of a non-symmetric  $\mathbf{M}$  can result in a scheme that is dissipative even if  $\mathbf{A}(c)$  is skew-symmetric. If  $\operatorname{Re}(\hat{A}(k)) > 0$  for some  $k$ , then the amplitudes of the signal will grow in time, and the semi-discretization is considered to be *unstable*.

When  $\operatorname{Re}(\hat{A}_k) = 0$ , i.e., the discretization is energy conserving, the only remaining numerical artifact is the difference between the speed that signals propagate in the continuous and discrete sense. In order to assess this effect, Eq. (2.5) is written as

$$T_{k,(m,n)}(t) = \hat{T}_k(0) \exp[\iota k(m\Delta x \cos \theta + n\Delta y \sin \theta + \operatorname{Im}(\hat{A}(k)) t/k)]. \quad (2.11)$$

From this, the discrete, or apparent advective velocity is

$$\tilde{c}(k) = \frac{\operatorname{Im}(\hat{A}(k))}{k} \quad (2.12)$$

which reveals the wavenumber dependence of the discrete advective or phase velocity. Thus, it is clear that each wavelength will propagate at its own unique velocity on the computational grid.

### 2.1.2 Fourier Analysis and Truncation Error

There is a relationship between Fourier analysis and classical truncation error analysis as pointed out by Vichnevetsky and Bowles [33] (see pp. 24-26, pp. 103-108). We repeat the salient points of this discussion here.

Given a solution to the one-dimensional continuous advection problem,  $T(x, t)$ , the truncation error may be written as

$$\mathcal{T} = \frac{dT_m}{dt} - \mathbf{M}^{-1} \mathbf{A}(c) T_m, \quad (2.13)$$

where

$$T_m(t) = T(x_m, t), \quad (2.14)$$

i.e.,  $T_m(t)$  are the values of  $T(x, t)$  evaluated at the discrete points  $x_m$ .

As demonstrated by Vichnevetsky and Bowles, the truncation error for the semi-discretizations considered in this work can be generalized as

$$\mathcal{T} = C\Delta x^p \left( \frac{\partial^{p+1} T}{\partial x^{p+1}} \right) + H.O.T. \quad (2.15)$$

where  $C$  is a constant independent of the data, grid spacing and order of accuracy.

The direct relationship between the order of accuracy and the “flatness” of the phase speed near  $k\Delta x = 0$  may be seen by taking the Fourier transform of the truncation error.

$$\mathcal{F}(\mathcal{T}) = -\iota\omega(c - \tilde{c})\hat{T}(\omega, t). \quad (2.16)$$

From this, it can be seen that the truncation error is

$$\tilde{c} - c = C\Delta x^p(\iota\omega)^p + H.O.T. \quad (2.17)$$

and behaves like  $\omega^p$  near  $k\Delta x = 0$  where  $p$  is the order of accuracy.

In the ensuing discussion, we make use of this relationship to identify the order of accuracy for the advective and diffusive discretizations considered in this work.

## 2.2 Second-Order Upwind as a Prototype

In this section, Fourier analysis is applied to a typical finite difference discretization with a second-order upwind scheme applied to the advective terms and a second-order centered stencil applied to the diffusive terms. Following Vichnevetsky and Bowles [33] and Mullen and Belytschko [19], a general solution to Eq. (2.1) is developed in the following form,

$$T(x, y, t) = A \exp[\iota k(x \cos \theta + y \sin \theta) - \iota\omega t - k^2 \alpha t]. \quad (2.18)$$

Here,  $k$  denotes the wave number, and  $\omega$  is the circular frequency associated with the advective solution. The wave vector is  $\mathbf{k} = k \cos \theta \hat{i} + k \sin \theta \hat{j}$ .

**Remark.** The general solution in Eq. (2.18) incorporates two fundamental solutions. The advective component of the solution is assumed to be a plane wave propagating in the direction of the wave vector. In contrast, the diffusive component assumes that the continuous diffusion problem is a planar one-dimensional problem in the direction of the wave vector.

Now, turning to the semi-discrete case, the general solution may be written in terms of the grid-spacing as

$$T_{m,n}(t) = A \exp[\iota k(m\Delta x \cos \theta + n\Delta y \sin \theta) - \iota \tilde{\omega} t - k^2 \tilde{\alpha} t], \quad (2.19)$$

where  $\tilde{\omega}$  is the discrete wavelength-dependent circular frequency,  $\tilde{\alpha}$  is the discrete wavelength-dependent diffusivity, and the subscript  $k$  has been suppressed for notational convenience.

In the ensuing discussion, the phase speed (or advective speed) is defined as

$$c = \frac{\omega}{k}, \quad (2.20)$$

and represents the magnitude of the phase velocity vector  $\mathbf{c}$  which is oriented in the direction of the wave vector  $\mathbf{k}$ . In the continuum, the phase velocity is simply the advective velocity. As this analysis will demonstrate, the effect of spatial discretization is to make the discrete or apparent phase velocity a function of both the wavenumber and the propagation direction on the grid. That is to say, while the continuum may be non-dispersive, the spatially-discrete representation of the continuum will be dispersive.

The group velocity,  $\mathbf{v}_g = v_{g_x} \hat{i} + v_{g_y} \hat{j}$ , often referred to as the energy velocity, describes how local disturbances that are modulated by a longer-wavelength signal propagate. The group velocity is defined as

$$\mathbf{v}_g = \frac{\partial \omega}{\partial k_x} \hat{i} + \frac{\partial \omega}{\partial k_y} \hat{j}, \quad (2.21)$$

where,  $k_x = k \cos(\theta)$  and  $k_y = k \sin(\theta)$ . For a non-dispersive continuum the group velocity is simply the advective velocity, i.e.,  $v_{g_x} = u$  and  $v_{g_y} = v$ . In the discrete or dispersive case, the group velocity is not always aligned with the wave vector, but instead has a propagation direction defined by

$$\Theta = \arctan \left( \frac{\tilde{v}_{g_y}}{\tilde{v}_{g_x}} \right), \quad (2.22)$$

where  $\tilde{v}_{g_x} = \partial \tilde{\omega} / \partial k_x$ , and  $\tilde{v}_{g_y} = \partial \tilde{\omega} / \partial k_y$  are the components of the discrete group velocity. In the ensuing analysis it will be demonstrated that short wavelength signals exhibit the largest errors in phase, group and propagation direction.

### 2.2.1 Semi-Discrete Equations

In order to use the general solution to the advection-diffusion equation, the complete semi-discrete finite-difference equation at node  $(m, n)$  in the pe-

periodic grid is required. For a second-order upwind scheme with a central-difference discretization of the diffusion, the semi-discrete equation is

$$\begin{aligned}
\dot{T}_{m,n} &+ \frac{u}{2\Delta x} \{T_{m-2,n} - 4T_{m-1,n} + 3T_{m,n}\} \\
&+ \frac{v}{2\gamma\Delta x} \{T_{m,n-2} - 4T_{m,n-1} + 3T_{m,n}\} \\
&+ \left\{ \frac{\alpha}{(\gamma\Delta x)^2} \right\} 2(\gamma^2 + 1)T_{m,n} \\
&- \left\{ \frac{\alpha}{(\gamma\Delta x)^2} \right\} \{ \gamma^2(T_{m-1,n} + T_{m+1,n}) + (T_{m,n-1} + T_{m,n+1}) \} = 0,
\end{aligned} \tag{2.23}$$

where  $\gamma = \Delta y / \Delta x$ .

In terms of Eq. (2.2), here the mass matrix,  $M$ , is simply the identity ( $M_{m,n} = 1$ ), while the non-zero entries in the advective operators are those associated with the advective velocity components  $u$  and  $v$  in Eq. (2.23), and the terms in the diffusion matrix  $K$  are the penta-diagonal entries  $2(\gamma^2 + 1)$ ,  $-\gamma^2$  and  $-1$  with leading multiplier  $\alpha/(\gamma\Delta x)^2$ . The complete semi-discrete nodal equation for the second-order upwind method, as well as the other methods considered in this work, may be found in Appendix A.

### 2.2.2 Dispersion Relations

With the semi-discrete equation defined, attention is now turned to computing the dispersion formulae for the prototype second-order upwind finite difference scheme. With the semi-discrete nodal equation defined in Eq. (2.23) and the general solution defined in Eq. (2.19), there are two ways of proceeding with the analysis. The first uses linear superposition to segregate the advection and diffusion terms in Eq. (2.19). The second approach proceeds by simply substituting the general solution, Eq. (2.19), into Eq. (2.23). As will be demonstrated below, this approach yields real (diffusive) and imaginary (advective) parts, and further, segregates the advective operator into skew-symmetric (non-dissipative) and symmetric (dissipative) components. For this reason the second, i.e., direct substitution, approach is adopted because it permits characterization of the artificial diffusivity associated with the semi-discrete method.

**Remark.** An alternative approach to the decomposition of the advection operator into symmetric and skew-symmetric parts proceeds as follows. Given an arbitrary advection operator,  $\mathbf{A}$ , the symmetric (diffusive) part is  $\mathbf{A}_{sym} = 1/2(\mathbf{A} + \mathbf{A}^T)$  and the skew-symmetric part is  $\mathbf{A}_{skew} = 1/2(\mathbf{A} - \mathbf{A}^T)$ . Appendix A presents the semi-discrete operators in a *stencil* format with the  $x$  and

$y$ -advection operators split into symmetric and skew-symmetric components for all of the methods considered in this report.

After the direct substitution into Eq. (2.23), the result may be segregated into its real and imaginary components yielding relationships for the discrete circular frequency and discrete diffusivity. Making use of the fact that  $u = c \cos \theta$  and  $v = c \sin \theta$ , the discrete circular frequency is

$$\begin{aligned}\tilde{\omega} = & \frac{c \cos \theta}{2\Delta x} \{4 \sin(k\Delta x \cos \theta) - \sin(2k\Delta x \cos \theta)\} \\ & + \frac{c \sin \theta}{2\gamma\Delta x} \{4 \sin(k\gamma\Delta x \sin \theta) - \sin(2k\gamma\Delta x \sin \theta)\} .\end{aligned}\quad (2.24)$$

Using the definition for the phase speed in Eq. (2.20), the non-dimensional phase speed is

$$\begin{aligned}\frac{\tilde{c}}{c} = & \frac{1}{2k\Delta x} \{ \cos \theta [4 \sin(k\Delta x \cos \theta) - \sin(2k\Delta x \cos \theta)] \\ & + \frac{\sin \theta}{\gamma} [4 \sin(k\gamma\Delta x \sin \theta) - \sin(2k\gamma\Delta x \sin \theta)] \} .\end{aligned}\quad (2.25)$$

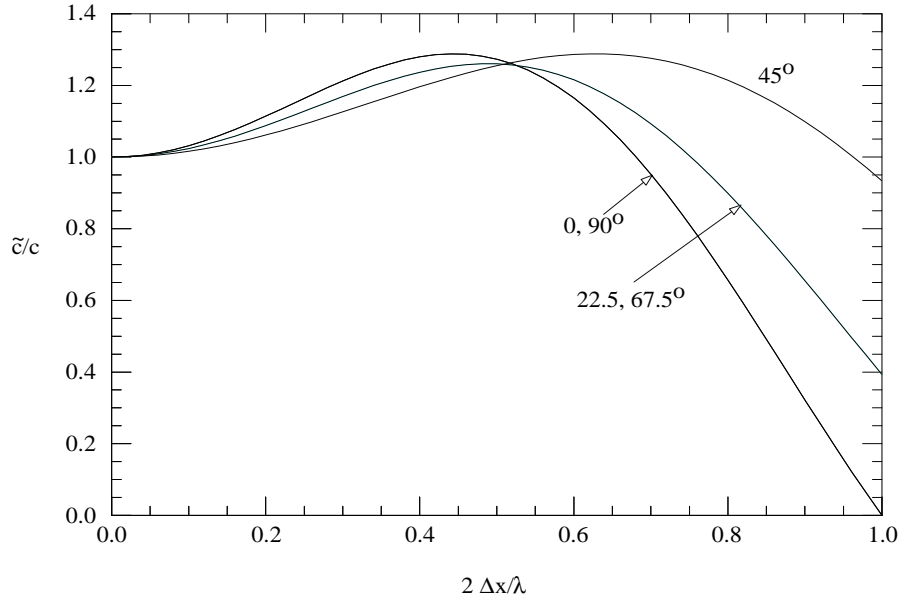
Figure 2.3 shows the non-dimensional phase speed as a function of non-dimensional wavenumber ( $k\Delta x/\pi = 2\Delta x/\lambda$ ) and propagation direction,  $\theta$ . The phase speed curves for  $\theta = 0$  and  $90^\circ$  indicate that the second-order upwind scheme results in leading phase errors ( $\tilde{c}/c > 1$ ) up to  $2\Delta x/\lambda \approx 0.68$  at which point the phase errors become strictly lagging ( $\tilde{c}/c < 1$ ). At  $\theta = 0, 90^\circ$ , the phase speed goes to zero at  $2\Delta x/\lambda = 1$  indicating that  $2\Delta x$  waves are stationary on the grid. For all other propagation directions,  $2\Delta x$  wavelengths, which correspond to the grid Nyquist limit, propagate with finite velocity. The phase speed is a strong function of propagation angle with the amount of variation increasing with decreasing wavelength.

Using equations (2.24) and (2.21), the components of the non-dimensional group speed are

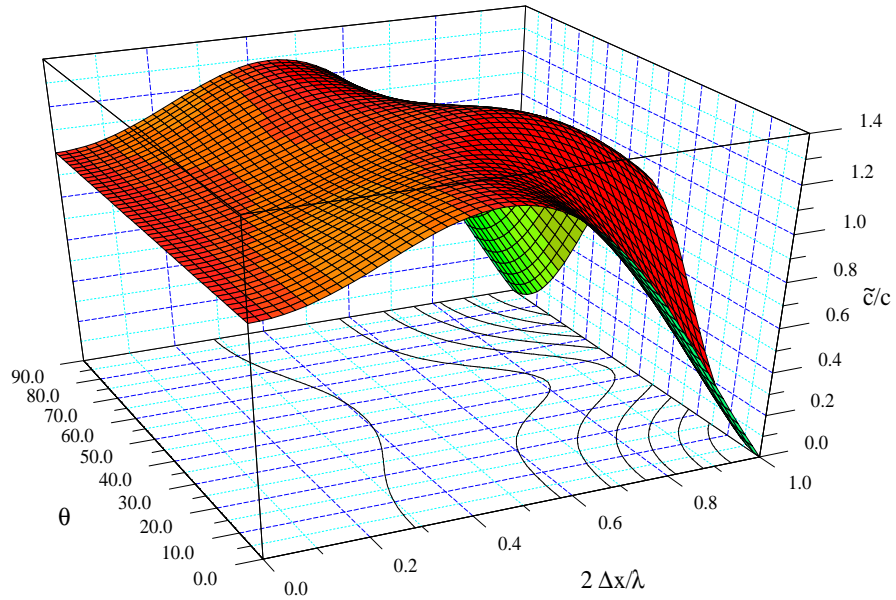
$$\begin{aligned}\frac{\tilde{v}_{gx}}{c} &= \cos \theta \{2 \cos(k \cos \theta \Delta x) - \cos(2k \cos \theta \Delta x)\} \\ \frac{\tilde{v}_{gy}}{c} &= \sin \theta \{2 \cos(k \sin \theta \gamma \Delta x) - \cos(2k \sin \theta \gamma \Delta x)\} .\end{aligned}\quad (2.26)$$

The components of the non-dimensional group velocity are shown in Figures 2.4 and 2.5 as functions of the non-dimensional wave number,  $2\Delta x/\lambda$ , and the wave-vector direction  $\theta$ . The group velocity exhibits both leading and lagging errors depending on the propagation direction and signal wavelength – with the group velocity going to zero along the coordinate directions for signals with  $\lambda = 3.2296\Delta x$  (or  $2\Delta x/\lambda = 0.6193$ ). Along the x and y-coordinate





a)



b)

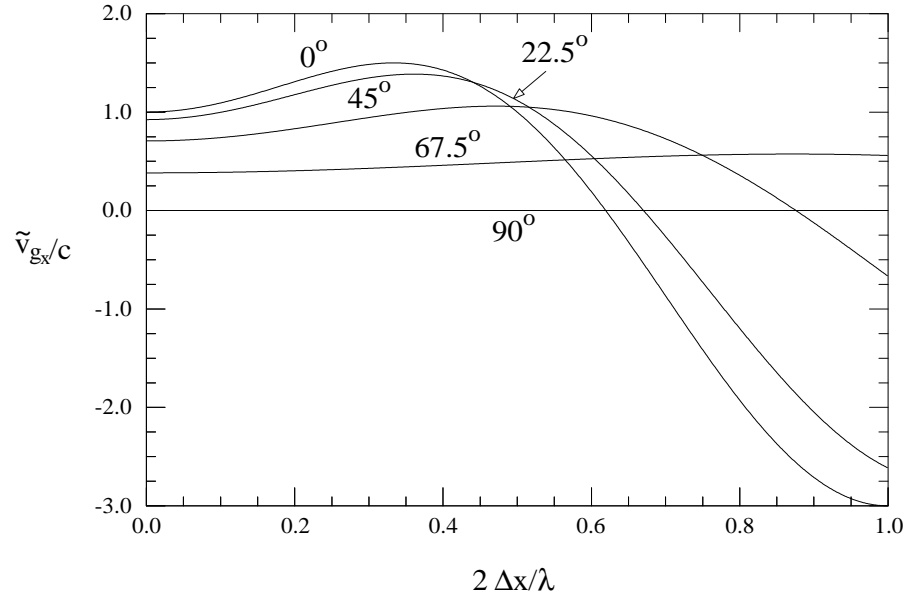
Figure 2.3: Non-dimensional phase speed for the second-order up-wind method: a) phase vs. non-dimensional wavenumber for  $\theta = 0, 22.5, 45, 67.5, 90^\circ$ , b) phase vs. non-dimensional wavenumber and propagation direction (in degrees).

directions, and at the Nyquist limit, the group velocity is negative and three times as large as the advective velocity. This would appear to be in contradiction to the phase speed plots in Figure 2.3 which indicates that  $2\Delta x$  signals are stationary. However, because the discrete advective problem is dispersive and the phase velocity is wavelength dependent, an envelope or wave-packet containing  $2\Delta x$  information may be seen to propagate upstream at the group speed for the  $2\Delta x$  signals. That is to say, the *modulated*  $2\Delta x$  signals appear to move upstream even though the individual  $2\Delta x$  signals are stationary – an artifact of the discretization. Thus, we see that the utility of the group velocity is in understanding the propagation of short-wavelength signals that may be generated at physical boundaries and in regions where the mesh resolution changes rapidly (see for example Reference [30]).

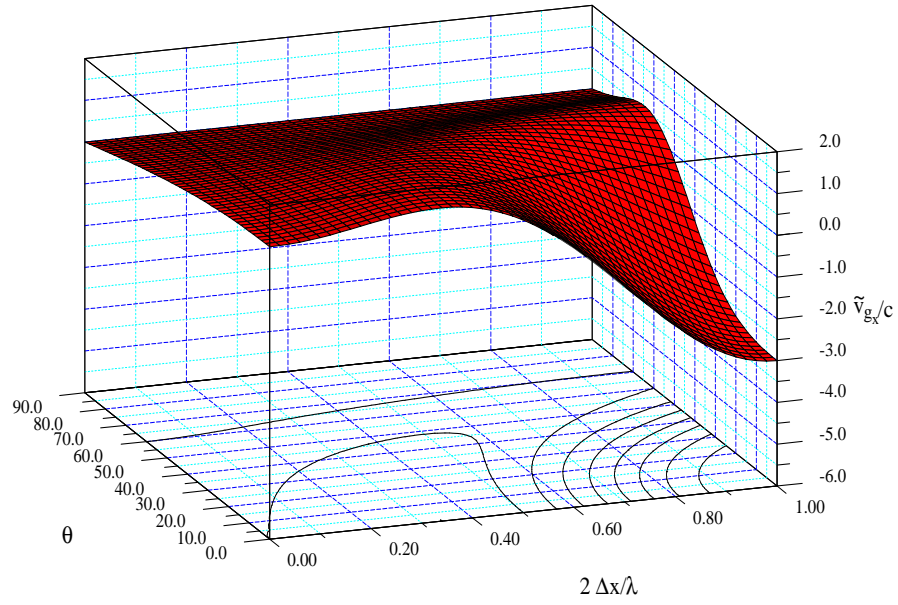
In order to demonstrate the role of group velocity in understanding discrete wave propagation phenomena, consider the pure advection problem in one-dimension with the initial conditions shown in Figure 2.6a. This computation used the skew-symmetric, i.e., energy conserving, advection operator and neglects the symmetric, i.e., diffusive, parts (cf. §A.3 for details of the second-order upwind advective operator). Figure 2.6b and 2.6c show the presence of a slow moving  $\lambda \approx 3\Delta x$  signal, and a backward-propagating signal with a  $2\Delta x$  wavelength. Based on Figure 2.4a ( $\theta = 0^\circ$ ) and the group velocity in Eq. (2.21), a modulated signal with wavelength  $\lambda/\Delta x = 3.2296$  is stationary on the grid. Here, the  $\approx 3\Delta x$  signal appears to move slowly upstream (backwards) with a non-dimensional group velocity of  $-1/2$  while the  $2\Delta x$  wave packet appears to move backwards at a group velocity of  $-3$ .

For the sake of comparison, the computation was repeated using the “full” second-order upwind scheme including the symmetric and diffusive part of the advective operator. The effect of the diffusive part of the advective operator on the computations is to damp the short wavelength signals as shown in Figure 2.7. Note the presence of a leading disturbance in both cases is indicated by the leading phase (and group) errors for the second-order upwind method.

As noted previously, for a non-dispersive continuum, the group speed would correspond to the advective speed  $c$  and the propagation direction to  $\theta$ . However, in the discrete sense, both the group speed and propagation direction vary with wavelength and wave-vector direction. The direction for the discrete group speed  $\Theta$  is shown in Figure 2.8. Here, it is seen that in the limit as  $\Delta x \rightarrow 0$ , the group velocity is aligned with the wave-vector. Similarly, for  $2\Delta x/\lambda \leq 0.6$ , the group velocity and wave-vector align along  $\theta = 0, 45, 90^\circ$ . However, for the short-wavelength signals, it is clear that the group velocity may be incorrect and oriented in the wrong direction, e.g.,  $v_{gx} = -3$  and  $\Theta = 180^\circ$  for  $\theta = 0^\circ$  and  $2\Delta x/\lambda = 1.0$ .

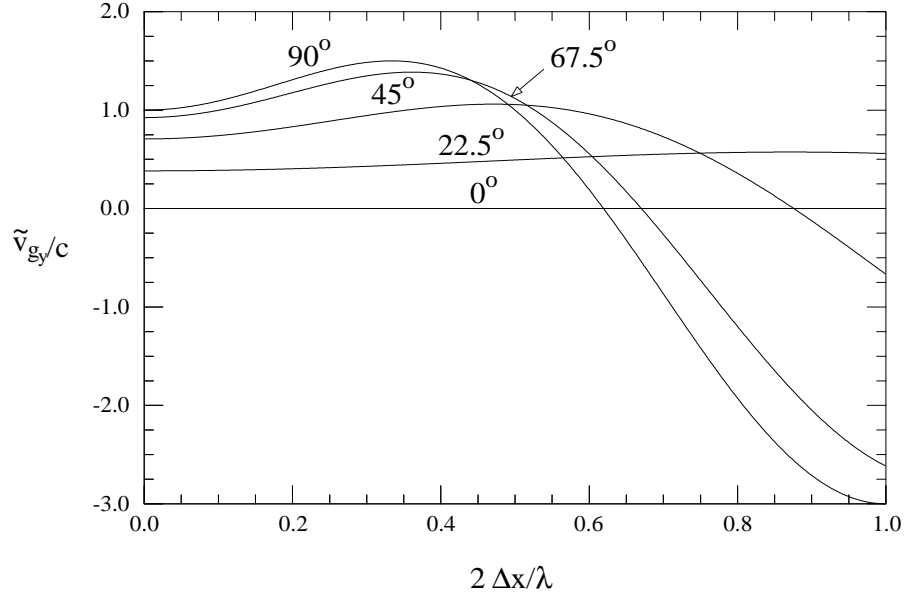


a)

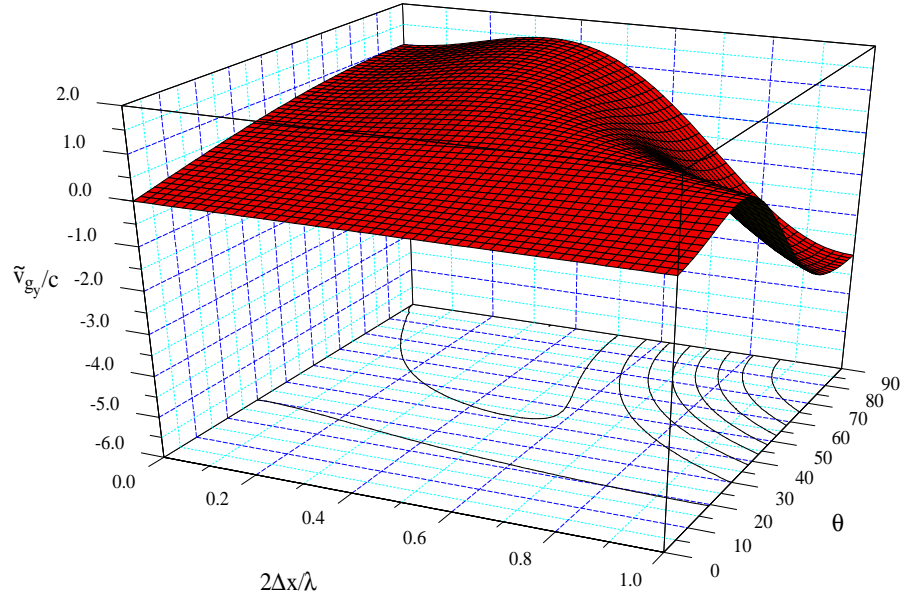


b)

Figure 2.4: Component of the group velocity in the  $x$ -coordinate direction: a)  $\tilde{v}_{gx}$  vs. non-dimensional wavenumber along  $\theta = 0, 22.5, 45, 67.5, 90^\circ$ , b)  $x$ -velocity component vs. non-dimensional wavenumber and direction (All angles presented in degrees.)



a)



b)

Figure 2.5: Component of the group velocity in the  $y$ -coordinate direction: a)  $\tilde{v}_{gy}$  vs. non-dimensional wavenumber along  $\theta = 0, 22.5, 45, 67.5, 90^\circ$ , b)  $y$ -velocity component vs. non-dimensional wavenumber and direction. (All angles presented in degrees.)

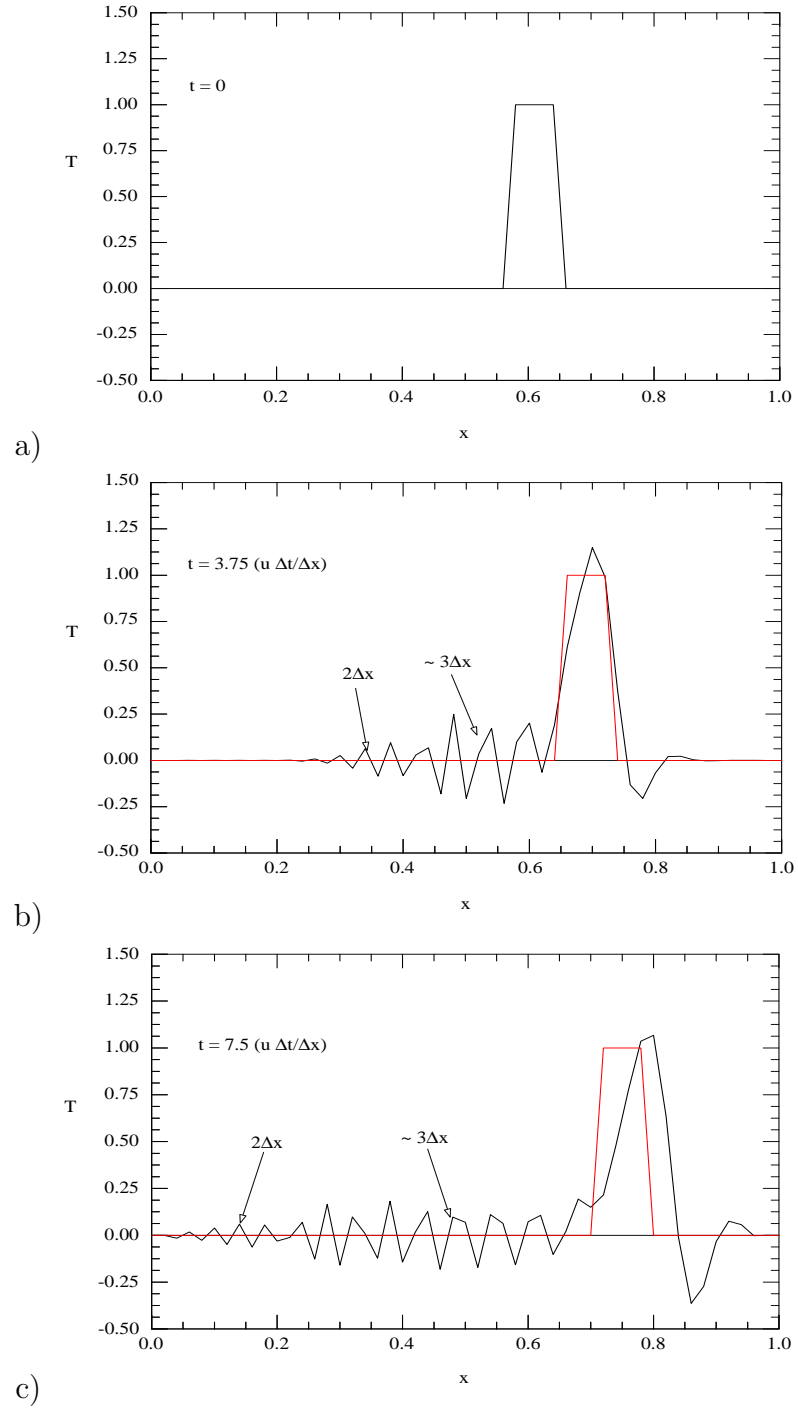


Figure 2.6: Snapshots of the temperature profile for the pure advection problem calculated using the skew-symmetric second-order upwind advective operator at a)  $t = 0$ , b)  $t = 3.75u\Delta t/\Delta x$ , and c)  $t = 7.5u\Delta t/\Delta x$ .

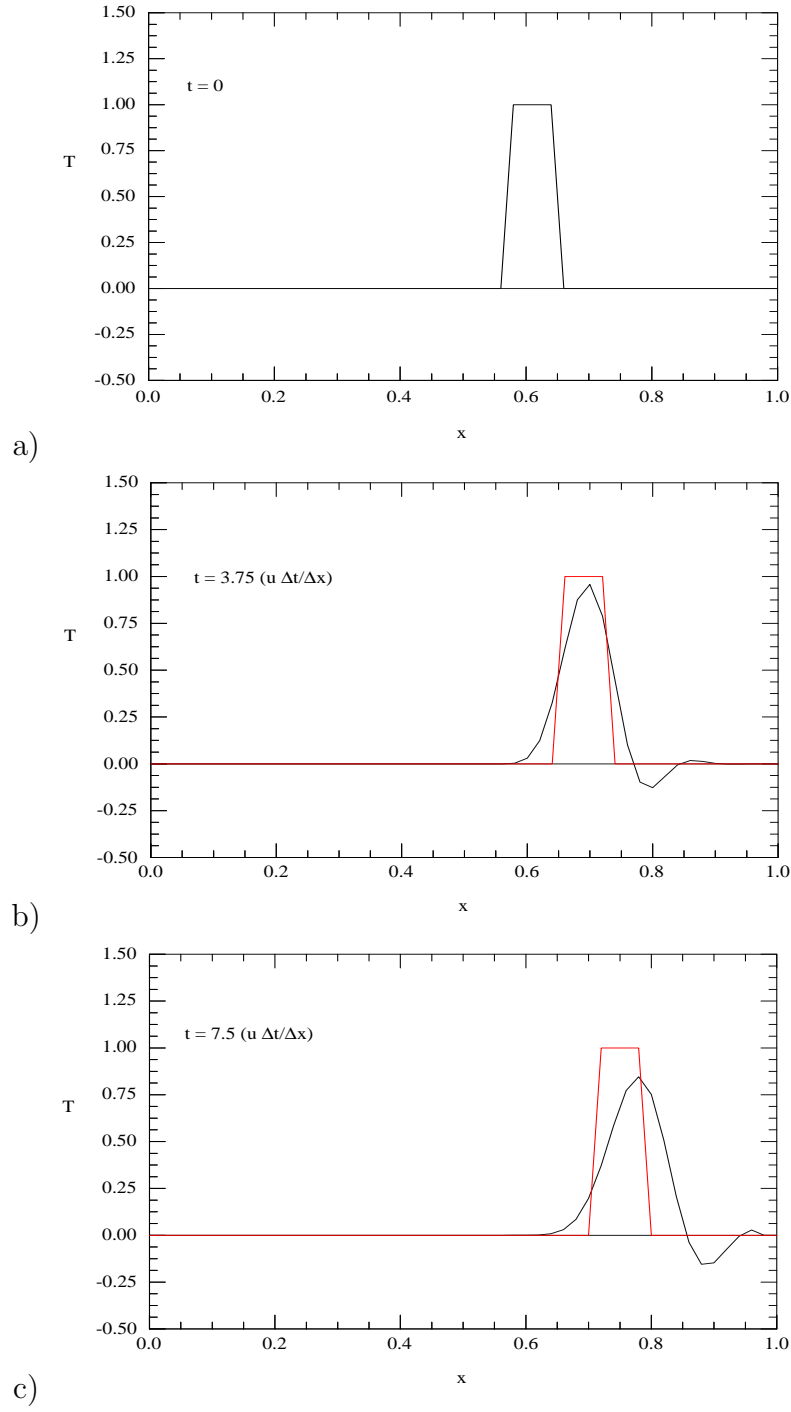


Figure 2.7: Snapshots of the temperature profile for the pure advection problem calculated using the second-order upwind advective operator at a)  $t = 0$ , b)  $t = 3.75u\Delta t/\Delta x$ , and c)  $t = 7.5u\Delta t/\Delta x$ .

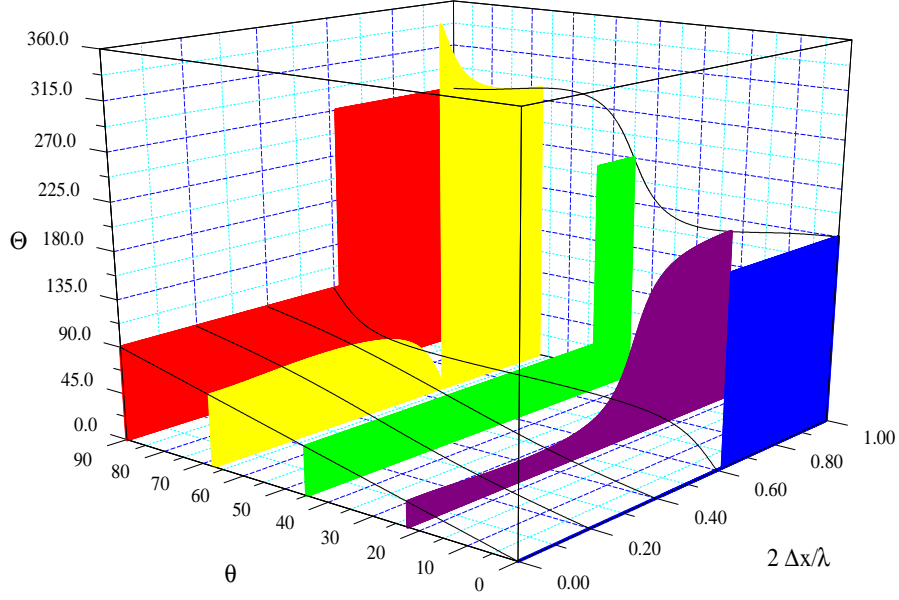


Figure 2.8: Group angle,  $\Theta$ , for the second-order upwind method. (All angles presented in degrees.)

### 2.2.3 Discrete Diffusivity

Turning attention to the real, i.e., diffusive term that derives from substitution of the general solution into the semi-discrete equation, the apparent diffusivity may be computed as

$$\begin{aligned} \bar{\alpha} = & \frac{\alpha}{(k\gamma\Delta x)^2} \left\{ 2(\gamma^2 + 1) - 2\gamma^2 \cos(k\Delta x \cos \theta) - 2 \cos(k\gamma\Delta x \sin \theta) \right\} \\ & + \frac{c \cos \theta}{2k^2\Delta x} \left\{ 3 + \cos(2k\Delta x \cos \theta) - \cos(k\Delta x \cos \theta) \right\} \\ & + \frac{c \sin \theta}{2k^2\gamma\Delta x} \left\{ 3 + \cos(2k\gamma\Delta x \sin \theta) - \cos(k\gamma\Delta x \sin \theta) \right\}. \end{aligned} \quad (2.27)$$

The apparent diffusivity is comprised of two parts. The first part (the first term in Eq. 2.27) is identified as the discrete diffusivity  $\tilde{\alpha}$ , while the second part (last two terms of the equation) derives from the specific advective scheme and may be interpreted as an artificial diffusivity  $\alpha_{art}$ . Therefore, Eq. (2.27) may be decomposed as  $\bar{\alpha} = \tilde{\alpha} + \alpha_{art}$ .

The non-dimensional discrete diffusivity is

$$\frac{\tilde{\alpha}}{\alpha} = \frac{1}{(k\gamma\Delta x)^2} \left\{ 2(\gamma^2 + 1) - 2\gamma^2 \cos(k\Delta x \cos \theta) - 2 \cos(k\gamma\Delta x \sin \theta) \right\}, \quad (2.28)$$

and is shown graphically in Figure 2.9. Here, the angular dependence, i.e., grid bias in the discrete diffusivity is apparent. The overall effect of the

discretization scheme is to reduce the discrete diffusivity relative to the prescribed physical diffusivity for all wavelengths in the spectrum. The worst-case is seen to be at  $2\Delta x$  wavelengths along the principal grid lines ( $x$  and  $y$ -coordinate directions) where the discrete diffusivity is approximately 40% of its true continuum value.

### 2.2.4 Artificial Diffusivity

The diffusive effects of the advective scheme are associated with the symmetric part of the advection operator. For the second-order upwind scheme, the symmetric part of the advection operator yields an artificial diffusivity that is presented here in a non-dimensional form as

$$\frac{1}{\mathbf{P}_e^{art}} = \frac{1}{(k\Delta x)^2} \left\{ \cos \theta [3 + \cos(2k\Delta x \cos \theta) - 4 \cos(k\Delta x \cos \theta)] + \frac{\sin \theta}{\gamma} [3 + \cos(2k\gamma\Delta x \sin \theta) - 4 \cos(k\gamma\Delta x \sin \theta)] \right\}, \quad (2.29)$$

where the Peclet number based on the artificial diffusivity,  $\mathbf{P}_e^{art}$ , is defined as

$$\mathbf{P}_e^{art} = \frac{c\Delta x}{2\alpha_{art}}. \quad (2.30)$$

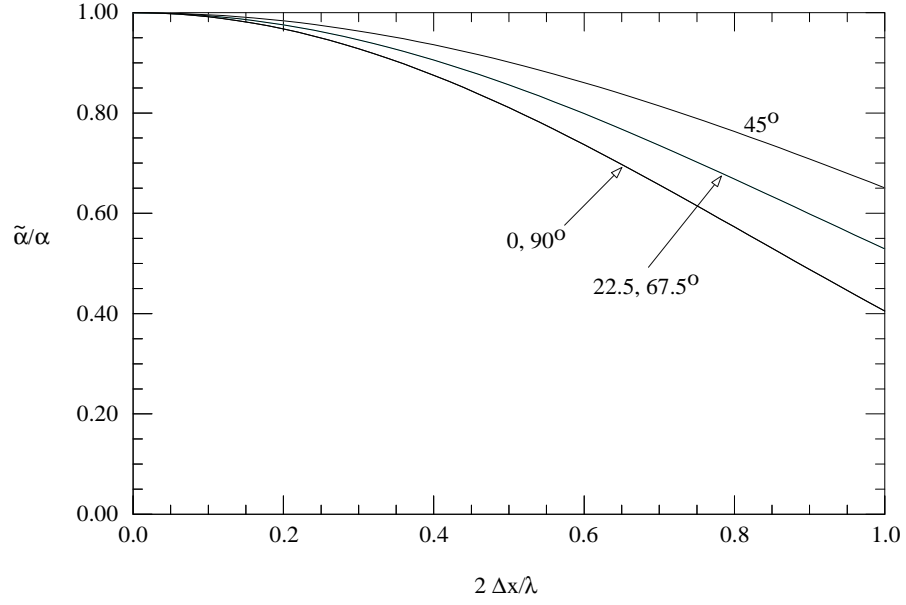
The grid Peclet number is defined as

$$\mathbf{P}_e = \frac{c\Delta x}{2\alpha}. \quad (2.31)$$

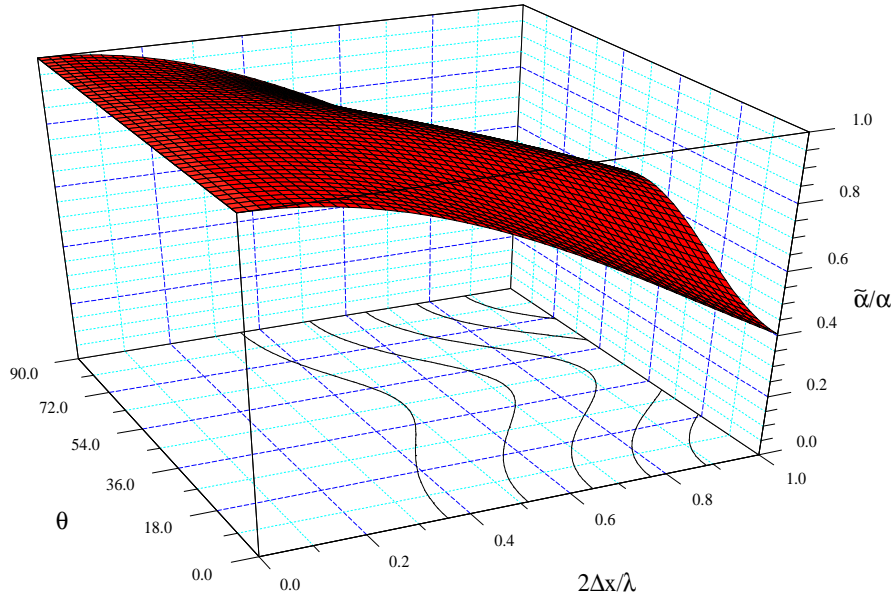
An alternative and equivalent non-dimensional scaling for the artificial diffusivity is based on the physical diffusivity, i.e.,  $\alpha_{art}/(\alpha\mathbf{P}_e)$ . However, this definition is equivalent to the scaling used in Eq. (2.29) and requires the introduction of a physical diffusivity which need not be present in the case of pure advection (although the artificial diffusivity will always be present). In addition, for the limiting case of pure advection, the scaling used in Eq. (2.30) provides an indicator of how much the discrete solution deviates from the case when  $\mathbf{P}_e \rightarrow \infty$ . In addition, this metric indicates that when artificial diffusivity is introduced, the apparent or effective Peclet number will remain finite – at least through a portion of the discrete spectrum.

The wavelength-dependent artificial diffusivity introduced by the second-order upwind scheme is shown in Figure 2.10. Again, there is a significant angular dependence, i.e., grid-bias in the artificial diffusivity. It is surprising that the artificial diffusivity vanishes only in the limit when  $2\Delta x/\lambda \rightarrow 0$ , i.e., in the limit of infinite wavelength signals (e.g., a constant mode) or conversely as  $\Delta x \rightarrow 0$ . Along the grid-lines,  $\theta = 0^\circ, 90^\circ$ , the maximum value of the artificial diffusivity does not occur at the grid Nyquist limit





a)



b)

Figure 2.9: Non-dimensional discrete diffusivity for the second-order up-wind method: a) discrete diffusivity vs. non-dimensional wavenumber for  $\theta = 0, 22.5, 45, 67.5, 90^\circ$ , b) discrete diffusivity vs. non-dimensional wavenumber and propagation direction.

( $2\Delta x$  wavelengths), but instead appears for  $2\Delta x/\lambda \approx 0.74$ . In contrast, along  $45^\circ$  lines, the maximum does occur at the grid Nyquist limit. This is somewhat surprising as it would seem desirable to introduce the largest artificial diffusivity only for the shortest wavelength signals, i.e., at the grid Nyquist limit for all propagation directions.

### 2.2.5 Effects of Artificial Diffusivity

The spectral behavior of the artificial diffusivity is revealing in that it indicates that the second-order upwind method introduces essentially no artificial diffusivity at long wavelengths while introducing increasing amounts as the wavelength is reduced. However, the spectral and directional dependence of the artificial diffusivity does not completely explain the damping effects of the artificial diffusivity on the temperature field.

In fact, from the results presented for the second-order upwind scheme, there is clearly an interplay between the artificial diffusivity, phase and group errors, and discrete diffusivity. While, it is difficult to identify an “ideal” artificial diffusivity, in our opinion, one that is active only in the high-frequency portion of the discrete spectrum is at least desirable. We can gain some additional insight into the effects of the artificial diffusivity on the discrete solution by considering its effect on the quadratic temperature,  $QT = T^2$ , where the time rate of change of  $QT$  is,

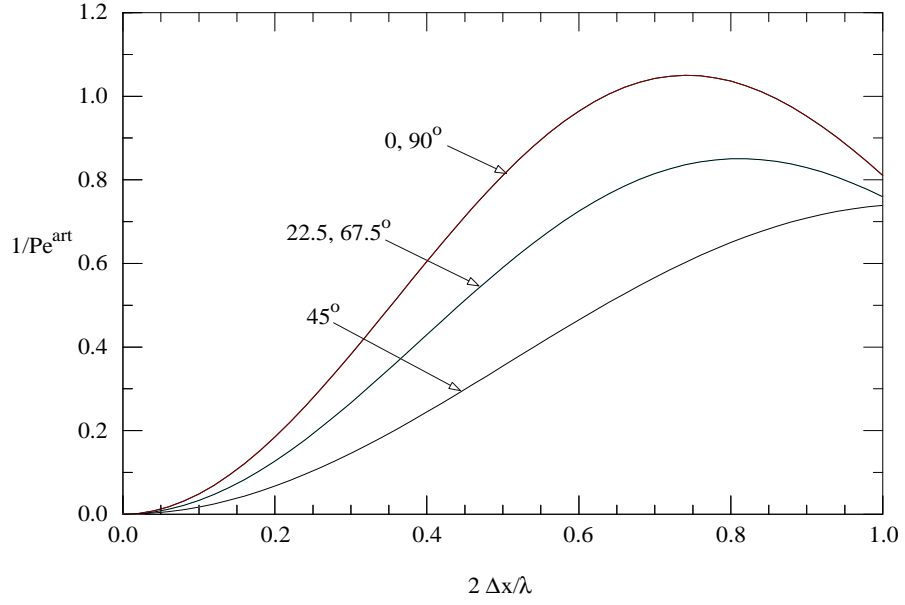
$$\frac{d}{dt}(QT) = \frac{1}{2} \frac{d}{dt} \int_{\Omega} \bar{T} T d\Omega = \frac{d}{dt} \left( \frac{1}{2} \bar{T}^T \mathbf{M}_{sym} T \right) \quad (2.32)$$

where,

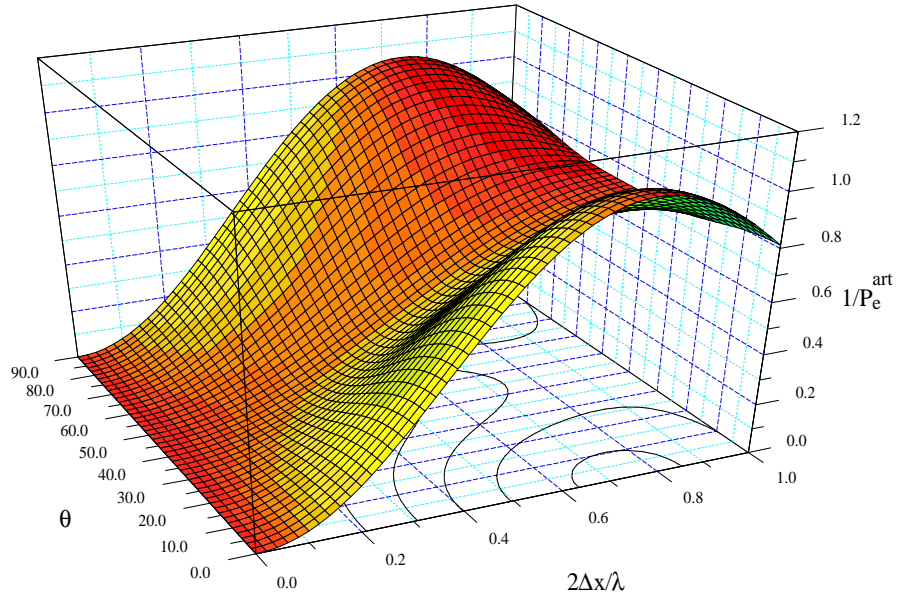
$$\overline{T_{m,n}} = A \exp[-k^2 \alpha_{art} t] \exp[-\iota k(m\Delta x \cos \theta + n\Delta y \sin \theta) + \iota \tilde{\omega} t] \quad (2.33)$$

is the complex conjugate of  $T$  and  $\mathbf{M}_{sym}$  is the symmetric part of the mass matrix.

**Remark.** The quadratic temperature is a reasonable quantity to consider because it provides a “natural” metric for quantifying the effects of artificial diffusivity. It is well-known that, for the advection-diffusion equation, methods that conserve the quadratic temperature generate stable ODE’s – an important feature for long-time integration. In addition, it was also demonstrated by Lee, et al. that conservation of  $T^2$  can be more important than other forms of conservation where stability is concerned[17].



a)



b)

Figure 2.10: Non-dimensional artificial diffusivity for the second-order up-wind method: a) artificial diffusivity vs. non-dimensional wavenumber for  $\theta = 0, 22.5, 45, 67.5, 90^\circ$ , b) artificial diffusivity vs. non-dimensional wavenumber and propagation direction.

We can show that the quadratic temperature is impacted by the symmetric and skew-symmetric parts of the advective and mass operators respectively (note that this is trivial if  $T$  is only real) by considering the pure advection problem, i.e., no physical diffusivity,

$$\mathbf{M}_{sym}\dot{T} + \mathbf{M}_{skew}\dot{T} + \mathbf{A}_{skew}(c)T + \mathbf{A}_{sym}(c)T = 0. \quad (2.34)$$

First, as  $\bar{T}$  and  $T$  are both solutions to the semi-discrete problem, we have,

$$\bar{T}^T \mathbf{M}_{sym} \dot{T} = -\bar{T}^T \mathbf{M}_{skew} \dot{T} - \bar{T}^T \mathbf{A}_{skew}(c)T - \bar{T}^T \mathbf{A}_{sym}(c)T \quad (2.35)$$

and,

$$T^T \mathbf{M}_{sym} \dot{\bar{T}} = -T^T \mathbf{M}_{skew} \dot{\bar{T}} - T^T \mathbf{A}_{skew}(c)\bar{T} - T^T \mathbf{A}_{sym}(c)\bar{T} \quad (2.36)$$

where the semi-discrete equation for  $T$  ( $\bar{T}$ ) has been pre-multiplied by  $\bar{T}^T$  ( $T^T$ ). Further, the mass matrix has been separated into skew-symmetric,  $\mathbf{M}_{skew}$ , and symmetric,  $\mathbf{M}_{sym}$ , parts in order to address the streamline-upwind finite element and control-volume finite element methods. Noting that

$$\frac{d}{dt}(QT) = \frac{d}{dt} \left( \frac{1}{2} \bar{T}^T \mathbf{M}_{sym} T \right) = \frac{1}{2} \bar{T}^T \mathbf{M}_{sym} \dot{T} + \frac{1}{2} T^T \mathbf{M}_{sym} \dot{\bar{T}} \quad (2.37)$$

and substituting from Eqs. (2.35) and (2.36) yields,

$$\frac{d}{dt}(QT) = -\frac{1}{2} \bar{T}^T \mathbf{M}_{skew} \dot{T} - \frac{1}{2} T^T \mathbf{M}_{skew} \dot{\bar{T}} - \bar{T}^T \mathbf{A}_{sym} T \quad (2.38)$$

where  $\bar{T}^T \mathbf{B}_{sym} T = T^T \mathbf{B}_{sym} \bar{T}$  and  $\bar{T}^T \mathbf{B}_{skew} T = -T^T \mathbf{B}_{skew} \bar{T}$  are employed ( $\mathbf{B}$  is any square matrix). Clearly, the quadratic temperature involves a complex interplay between artificial diffusivity (as it impacts  $T$  and  $\bar{T}$ ), the symmetric part of the advection operator and the skew-symmetric part of the mass matrix.

In order to understand the effect of the artificial diffusivity on the quadratic temperature, we consider an advective time-scale  $\tau = \Delta x/c$  and integrate Eq. (2.32) with respect to time to obtain the incremental change in  $QT$  over  $\tau$ ,

$$QT_{t+\tau} - QT_t = \int_t^{t+\tau} \frac{d}{dt} \left( \frac{1}{2} \bar{T}^T \mathbf{M}_{sym} T \right) dt. \quad (2.39)$$

Substituting the general solution and its complex conjugate, Eqs. (2.18) and (2.33) for  $T$  and  $\bar{T}$  respectively yields the quadratic temperature at some arbitrary time,  $t$ ,

$$\begin{aligned} QT_t &= A^2 \exp^2[-k^2 \alpha_{art} t] \\ &\times \sum_{m=1}^{NP} \sum_{n=1}^{NP} \left\{ \exp[-\iota k(x_{m,n} \cos \theta + y_{m,n} \sin \theta)] M_{m,n}^{sym} \right\}, \end{aligned} \quad (2.40)$$

where  $M_{m,n}^{sym}$  is the  $m^{th}$  row,  $n^{th}$  column entry in  $\mathbf{M}_{sym}$  and  $NP$  is the number of rows/columns. Note that  $QT$  is a function both of time,  $t$ , and wavenumber  $k$ .

In order to permit direct comparison between methods, we use the quadratic temperature at time  $t$  to construct a non-dimensional quadratic temperature increment over the advective time-scale  $\tau$  as

$$\Delta QT = \frac{QT_{t+\tau} - QT_t}{QT_t}. \quad (2.41)$$

In terms of this definition, it is clear that a method characterized by constant  $QT$  (i.e. no damping of quadratic temperature) produces  $\Delta QT = 0$  while  $\Delta QT = -1$  indicates a method with complete damping of the associated waveform in one advective time scale  $\tau$ .

After substitution into Eq. (2.41) and cancellation of terms, the non-dimensional quadratic temperature increment may be written as,

$$\Delta QT = \exp^2[-k^2 \Delta x^2 / (2\mathbf{P}_e^{art})], \quad (2.42)$$

where it is clear the  $\Delta QT$  is dependent on wavenumber and grid spacing (as is  $\mathbf{P}_e^{art}$ ). Finally, note that Eq. (2.42) is a general statement of the quadratic temperature increment for any of the methods considered in this document. Indeed, the only method-dependent part occurs in the artificial diffusivity contained in  $\mathbf{P}_e^{art}$ .

We can now calculate the quadratic temperature increment for the second-order upwind prototype by substituting Eq. (2.29) into Eq. (2.42) to yield,

$$\begin{aligned} \Delta QT &= \exp^2[-\{\cos \theta [3 + \cos(2k\Delta x \cos \theta) - 4 \cos(k\Delta x \cos \theta)] \\ &+ \frac{\sin \theta}{\gamma} [3 + \cos(2k\gamma\Delta x \sin \theta) - 4 \cos(k\gamma\Delta x \sin \theta)]\} / 2] \\ &- 1, \end{aligned} \quad (2.43)$$

which, again, is a measure of the decrease in (damping of)  $QT$  over the advective time scale,  $\tau = \Delta x/c$ , for the second-order upwind method.

Figure 2.11 shows  $\Delta QT$  as a function of non-dimensional wavenumber for the second-order upwind method. Here, we see modest angular dependence in the damping properties of the method. For example, it is clear that signals traveling along the  $45^\circ$  direction are completely damped in one advective time scale  $\tau$  for  $2\Delta x/\lambda > 0.80$  while waves traveling along the  $x$  or  $y$ -axes are completely damped for  $2\Delta x/\lambda > 0.65$ . Hence, for the second-order upwind scheme, high frequency oscillations will propagate further along the  $\theta = 0$  and  $90^\circ$  directions than along the  $45^\circ$  angle before being eliminated. Note that regardless of propagation direction, waves characterized by  $\lambda = 2\Delta x$  are completely damped over one characteristic time-scale,  $\tau$ .

This completes the prototype analysis of the semi-discrete second-order upwind scheme. Attention is now turned to the numerical methods compared in this report.

## 2.3 Semi-Discrete Methods Analyzed in this Work

In this work, a variety of popular finite difference, finite volume and finite element methods are considered. The Fourier analysis used to develop the baseline methods comparison is restricted to analysis on “regular” Cartesian grids – although we consider grids with non-unit aspect ratio in two-dimensions. In the Cartesian grid setting many of the finite volume methods considered here revert to familiar finite difference methods.

**Remark.** The restriction to regular grid configurations does not restrict the application of the generalized Fourier analysis to only grids comprised of quadrilaterals. For example, regular arrangements of triangular elements may be analyzed as in Mullen and Belytschko [19].

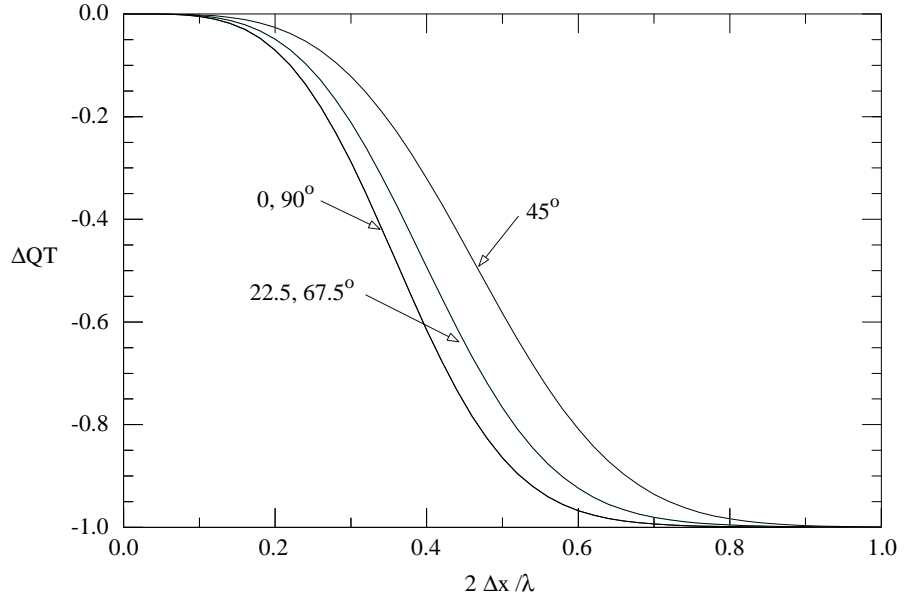
The family of finite volume methods considered in this work are, in general, developed for unstructured grids using a combination of MUSCL[29] interpolation with slope limiters and gradient reconstruction methods to model the convection terms. Two methods of gradient reconstruction are considered: application of the divergence theorem and an un-weighted least squares procedure [2]. Specifically, for the model problem under scrutiny, the finite volume methods are derived by starting with the following semi-discrete equation,

$$\begin{aligned} \Delta x \Delta y \frac{\partial T_{i,j}}{\partial t} + \Delta y u (T_{i+1/2,j} - T_{i-1/2,j}) + \Delta x v (T_{i,j+1/2} - T_{i,j-1/2}) = \\ \alpha \frac{\Delta y}{\Delta x} (T_{i+1,j} - 2T_{i,j} + T_{i-1,j}) + \alpha \frac{\Delta x}{\Delta y} (T_{i,j+1} - 2T_{i,j} + T_{i,j-1}). \end{aligned} \quad (2.44)$$

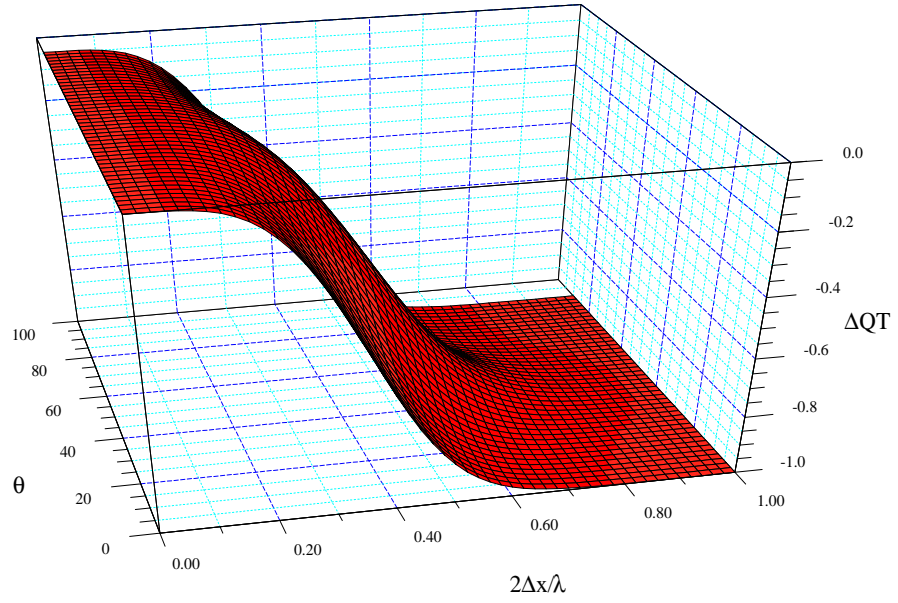
The various FVMs are derived by applying the generic MUSCL interpolation for convective terms,

$$T_{IJ} = T_I + \frac{\phi}{2} [(1 - \kappa) \nabla T_I \cdot (\mathbf{r}_J - \mathbf{r}_I) + \kappa (T_J - T_I)] \quad (2.45)$$

where  $T_{IJ}$  denotes the interpolated value between grid points  $I$  and  $J$ , for example equal to  $T_{i+1/2,j}$  where  $I = i$  and  $J = i + 1$ .  $\mathbf{r}_I$  is the position



a)



b)

Figure 2.11: Non-dimensional quadratic temperature increment for the second-order upwind method: a) quadratic temperature increment vs. non-dimensional wavenumber for  $\theta = 0, 22.5, 45, 67.5, 90^\circ$ , b) quadratic temperature increment vs. non-dimensional wavenumber and propagation direction.

vector for grid point  $I$ ,  $\phi$  is a limiter function, which will be zero or unity in this work. The various methods are derived for different combinations of the parameter  $\kappa$  and the method of gradient reconstruction to compute  $\nabla T_I$  in the interpolation formula.

For Cartesian grids, application of the divergence theorem yields a central difference approximation for the cell gradients, which when substituted into the MUSCL interpolant results in a variety of well-known higher order difference methods for  $\phi = 1$ : second-order central-difference (CD,  $\kappa = 1$ ), second-order upwind (SOU,  $\kappa = -1$ ), Fromm [9] differencing (this is the limit of Fromm’s fully discrete method for  $\Delta t \rightarrow 0$ ;  $\kappa = 0$ ), QUICK[18] ( $\kappa = 1/2$ ), and a 3rd-order upwind method (TOU) also due to Leonard [18] ( $\kappa = 1/3$ ). We also discuss an *ad-hoc* method composed of CD with a finite-element consistent mass matrix that can be derived by assuming a linear variation of the unknown within the control volume.

We also consider two finite volume schemes derived using the unweighted least squares reconstruction and  $\kappa = -1$  and  $\kappa = 0$ . For convenience we will refer to these as LSR(-1) and LSR(0) in the subsequent sections. Note that in one space dimensional, the LSR(-1) scheme corresponds to the second-order upwind (SOU) method, and the LSR(0) scheme corresponds to Fromm’s method. However, in two space dimensions, this is not the case. For the finite-element methods, we consider the well-known Galerkin finite element method (FEM) and its streamline-upwind Petrov-Galerkin (FEM-SUPG) derivative along with the more recently developed control volume finite element method (CVFEM) and its analogue to SUPG, known as SUCV (CVFEM-SUCV) [24, 25].

All of the semi-discrete operators considered in this work are presented in Appendix A.



# Chapter 3

## One-Dimensional Results

In this chapter, a summary of the discrete phase speed, group speed, diffusivity and artificial diffusivity is presented. The asymptotic truncation error associated with the phase and group speed, discrete and artificial diffusivity is presented for each method along with the resolution requirements for 5% and 1% error levels. In our opinion, errors in phase, group and discrete diffusivity of less than 5% are acceptable for many Engineering applications. In the ensuing discussion, the numerical approximation to the physical diffusivity  $\alpha$  is referred to as the discrete diffusivity  $\tilde{\alpha}$ , and the diffusivity added directly or indirectly by the advection scheme to modify the numerical scheme is referred to as the artificial diffusivity  $\alpha_{art}$ . All of the results are presented in a non-dimensional form, i.e., the phase speed ( $\tilde{c}/c$ ), group speed ( $\tilde{v}_g/c$ ), discrete diffusivity ( $\tilde{\alpha}/\alpha$ ), and artificial diffusivity ( $1/\mathbf{P}_e^{art}$ ) are presented in terms of the non-dimensional wave number,  $2\Delta x/\lambda = k\Delta x/\pi$ . For simplicity, the non-dimensional results are referred to as the phase, group, diffusivity and artificial diffusivity.

For each numerical method, the analytical expressions for the phase and group speed, discrete and artificial diffusivity are presented in a compact form as an aid to understanding the results of the Fourier analysis (see Tables 3.2, 3.4, 3.6, and 3.8). In the analytic expressions for phase and group speed, discrete and artificial diffusivity, the influence of the mass matrix in the FEM, FEM-SUPG, CVFEM, and CVFEM-SUCV methods is expressed in terms of the function  $\mathcal{M}(k\Delta x)$  as shown in Table 3.1. Note that the second-order node-centered finite difference scheme with a consistent mass matrix, referred to as the CD- $\mathbf{M}_c$  method in subsequent sections, is identical to the CVFEM formulation in one-dimension – although it is node-centered. Therefore, only the CVFEM results are presented here since the equivalent semi-discrete operators yield identical results. In addition, for the one-dimensional results, the second-order upwind (SOU) scheme corresponds to the LSR(-1) scheme, and Fromm’s method to the LSR(0) scheme. For this reason, we simply

present results for the SOU and Fromm’s methods.

As a final note, we consider errors in phase, group and diffusivity of less than 1% to be small. For the purposes of our discussion, errors between 1% to 5% are termed moderate while those that exceed 5% are deemed large. Note that this choice of error bounds is subjective, and further, depends upon the application of interest. However, we believe that this choice is generally appropriate for engineering calculations.

Method	$\mathcal{M}(k\Delta x)$
FEM/CVFEM – $\mathbf{M}_l$	1
FEM – $\mathbf{M}_c$	$(2 + \cos(k\Delta x))/3$
CVFEM – $\mathbf{M}_c$	$(3 + \cos(k\Delta x))/4$

Table 3.1: Mass matrix contribution for FEM and CVFEM methods where  $\mathbf{M}_l$  indicates a lumped mass matrix and  $\mathbf{M}_c$  indicates a consistent mass matrix.

### 3.1 Phase Speed

The analytic expressions for the non-dimensional phase speed for all of the semi-discrete methods considered may be found in Table 3.2. Here, the compact notation for the mass matrix (see Table 3.1) is used for the FEM/CVFEM phase speed. The FEM/CVFEM expression includes the effect of the streamline upwind Petrov-Galerkin formulation as indicated by the presence of the stabilization parameter,  $\beta$  (see Appendix A, Eq. (A.29) ), and the Peclet number  $\mathbf{P}_e$ . The FEM and CVFEM phase speeds are recovered for  $\beta = 0$  and the appropriate mass matrix symbol. The phase speed formulae for second-order central differences, the Galerkin finite element method and control-volume finite element method may be found in Gresho and Sani [11].<sup>1</sup> The semi-discrete stencils for all the methods considered in this work may be found in Appendix A.

The non-dimensional phase speed results for a variety of finite-difference (or node-centered finite-volume) methods are presented in Figure 3.1. For comparison, the non-dimensional phase speed for the FEM and CVFEM methods are presented in Figures 3.2 and 3.3. The phase speed for the FEM-SUPG and CVFEM-SUCV methods are presented for pure advection, i.e., when  $\mathbf{P}_e \rightarrow \infty$ , in Figures 3.2 and 3.3.

---

<sup>1</sup>The formula in Gresho and Sani [11] for phase speed (Eq. 2.6-79) contains an obvious typographical error in the numerator.

Method	Phase Speed ( $\tilde{c}/c$ )
FOU	$\sin(k\Delta x)/k\Delta x$
SOU	$[4 \sin(k\Delta x) - \sin(2k\Delta x)]/2k\Delta x$
TOU	$[8 \sin(k\Delta x) - \sin(2k\Delta x)]/6k\Delta x$
QUICK	$[10 \sin(k\Delta x) - \sin(2k\Delta x)]/8k\Delta x$
Fromm's	$[6 \sin(k\Delta x) - \sin(2k\Delta x)]/4k\Delta x$
FEM / CVFEM	$\frac{\sin(k\Delta x)[\mathcal{M}(k\Delta x) + \beta(2\beta + \mathbf{P}_e^{-1})(1 - \cos(k\Delta x))]}{k\Delta x(\mathcal{M}^2(k\Delta x) + \beta^2 \sin^2(k\Delta x))}$

Table 3.2: Formulae for one-dimensional phase speed.

In the absence of phase errors, the ideal semi-discrete phase speed would exactly replicate the continuous phase speed for the entire discrete spectrum from the limit  $\Delta x \rightarrow 0$  to the grid Nyquist limit where  $2\Delta x/\lambda = 1$ . However, all of the methods considered here introduce phase errors – either lagging or leading, with signals associated with the Nyquist limit, i.e.,  $2\Delta x$  wavelengths, being stationary. In the one-dimensional limit, the lumped mass FEM, FDM and CVFEM schemes yield identical spatial discretizations and non-dimensional phase speed results.

**Remark.** In the initial multi-methods comparison, we have not considered the effects of *ad-hoc* “tricks-of-the-trade”, such as reduced integration for the FEM and CVFEM formulations, on the phase and group speed, discrete and artificial diffusivity. The interested reader may consult Gresho, et al. [10] who has considered the effects of reduced integration for the advection-diffusion equation using a Galerkin finite element formulation.

As a reminder to the reader, recall that the first-order upwind scheme may be decomposed into a centered second-order advection scheme with concomitant second-order artificial viscosity. This is reflected in Figure 3.1 by the non-dimensional phase curve for the “Centered FDM” scheme. Both Fromm’s method and the SOU scheme introduce leading phase error for the mid-range wavelengths although the severe ( $\approx 30\%$ ) phase errors in the mid-range of the discrete spectrum for the second-order upwind method are significantly greater than for Fromm’s method.

In comparison to the finite difference schemes, the only finite element formulation that yields leading phase errors as large as the second-order upwind FDM scheme is the FEM-SUPG method with a constant stabilization parameter of  $\beta = 1/2$  (see Figure 3.2). Of interest here is the significant improvement in phase speed in moving from the baseline Galerkin FEM discretization using a consistent mass to the FEM-SUPG formulation with an

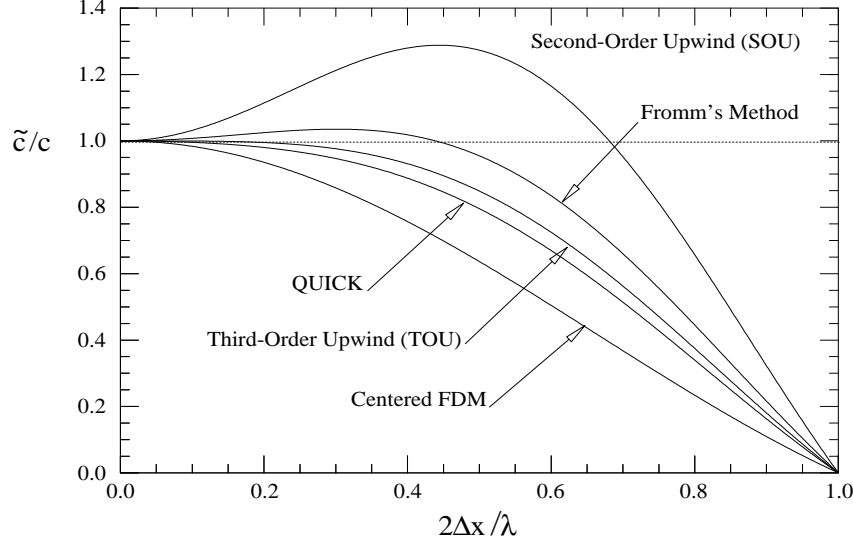


Figure 3.1: Non-dimensional phase speed for a variety of finite-difference (node-centered finite-volume) methods.

optimal stabilization parameter  $\beta_{opt} = 1/\sqrt{15}$ . This value of the stabilization parameter was shown by Raymond and Gardner [22] to annihilate all truncation error up to sixth-order; see also Gresho and Sani [11].

The CVFEM methods considered here yield strictly lagging phase error as shown in Figure 3.3. The CVFEM-SUCV method with  $\beta_{opt}$  (optimal  $\beta$  for FEM-SUPG) and a consistent mass matrix yields a non-dimensional phase speed close to the Galerkin FEM with a consistent mass matrix in the mid-range wavelengths. Although, it will be shown that CVFEM-SUCV cannot reproduce the fourth-order phase accuracy of the simple Galerkin FEM. The ad-hoc application of the streamline-upwind Petrov-Galerkin formulation also cannot be “tuned” to yield the high-order behavior associated with FEM-SUPG. In fact,  $\beta = 1/2$  appears to be an overall better stabilization parameter for SUCV, albeit with noticeable lagging errors in the phase speed thru the mid-range wavelengths of the discrete spectrum. A direct comparison between the FEM-SUPG and CVFEM-SUCV methods may be seen in Figure 3.4 where the lagging phase errors of the CVFEM-SUCV method are evident – even for the “optimal” CVFEM-SUCV stabilization parameter,  $\beta = 1/2$ .

The FEM-SUPG and CVFEM-SUCV methods exhibit a dependence on the Peclet number as shown in Figures 3.5 and 3.6 for  $1 \leq \mathbf{P}_e \leq 100$  and optimal stabilization parameters –  $\beta = 1/\sqrt{15}$  for FEM-SUPG and  $\beta = 1/2$  for CVFEM-SUCV. Both FEM-SUPG and CVFEM-SUCV yield large leading phase errors over 50% or more of the discrete spectrum for  $\mathbf{P}_e < 5$

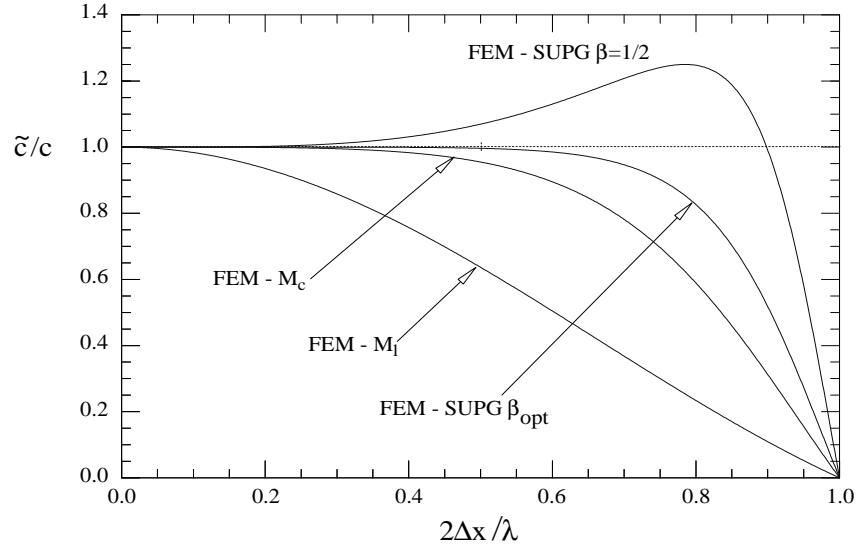


Figure 3.2: Non-dimensional phase speed for finite element method with a consistent mass matrix (FEM -  $\mathbf{M}_c$ ), lumped mass (FEM -  $\mathbf{M}_l$ ), consistent mass matrix and FEM-SUPG with  $\beta_{opt}$  and  $\beta = 1/2$ .

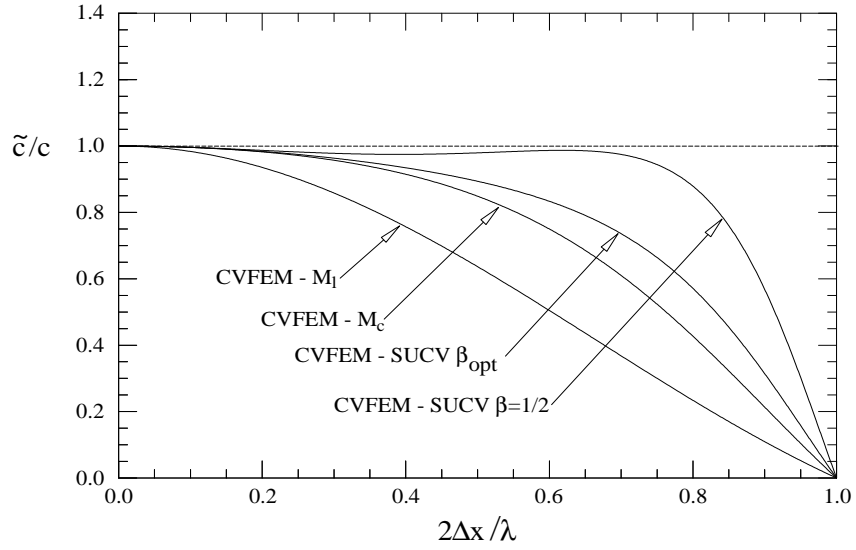


Figure 3.3: Non-dimensional phase speed for control-volume finite element method with a consistent mass matrix (CVFEM -  $\mathbf{M}_c$ ), lumped mass (CVFEM -  $\mathbf{M}_l$ ), consistent mass matrix and SUCV with  $\beta_{opt}$  and  $\beta = 1/2$ .

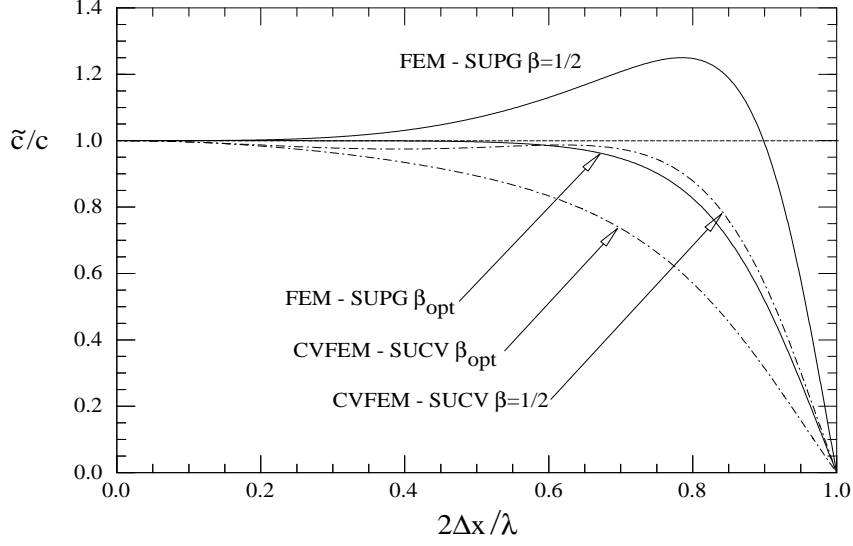


Figure 3.4: Non-dimensional phase speed for control-volume finite element and finite element methods using streamline upwinding (CVFEM-SUCV and FEM-SUPG).

suggesting that the stabilization parameter should be selected based on the Peclet number.

The Peclet number dependence may be scaled out of the problem by using the stabilization parameter suggested by Brooks and Hughes [5] which in one-dimension is

$$\tau = \beta \frac{\Delta x \xi}{u}, \quad (3.1)$$

where

$$\xi = \coth(\mathbf{P}_e) - \frac{1}{\mathbf{P}_e}. \quad (3.2)$$

Figure 3.7 shows that  $\xi$  approaches unity for large Peclet number and goes to zero rapidly for  $\mathbf{P}_e \leq 3$ . Tezduyar [26] has suggested a doubly-asymptotic approximation to  $\xi$  as a more computationally efficient alternative to Eq. (3.2). The influence of the Peclet-number-adjusted stabilization on the phase speed is shown in Figure 3.8 for FEM-SUPG and in Figure 3.9 for CVFEM-SUCV. In both cases, moderate to large leading phase errors are introduced in the mid-range of the discrete spectrum.

### Asymptotic Truncation Error and Resolution Estimates

Asymptotic truncation error in phase speed can be determined by taking the limit as  $k\Delta x \rightarrow 0$  in the analytical expressions given in Table 3.2. Asymptotic

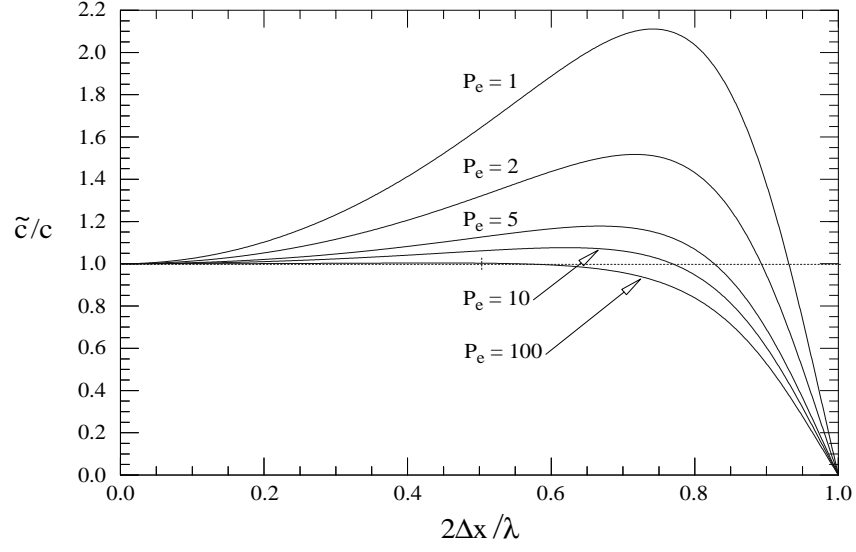


Figure 3.5: Non-dimensional phase speed for finite element method with a consistent mass matrix and FEM-SUPG with  $\beta_{opt}$  for  $\mathbf{P}_e = 1, 2, 5, 10, 100$ .

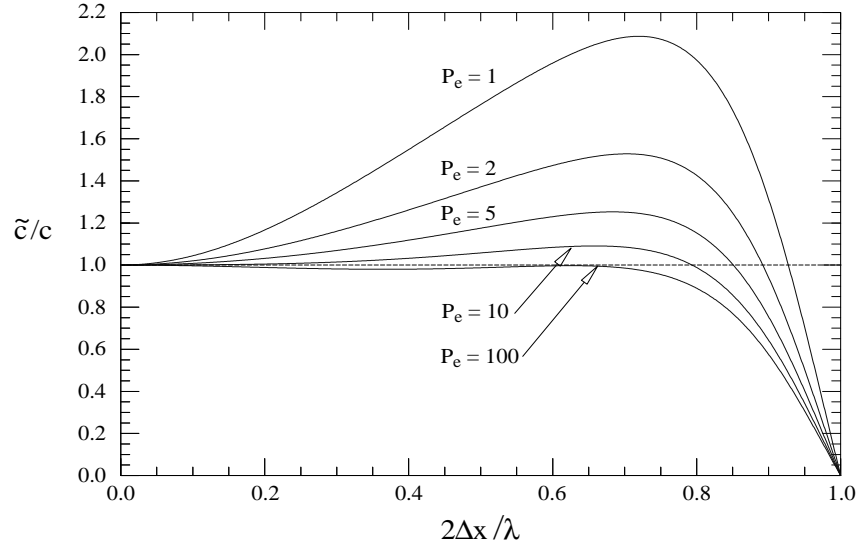


Figure 3.6: Non-dimensional phase speed for control-volume finite element method with a consistent mass matrix and SUCV with  $\beta = 1/2$  for  $\mathbf{P}_e = 1, 2, 5, 10, 100$ .

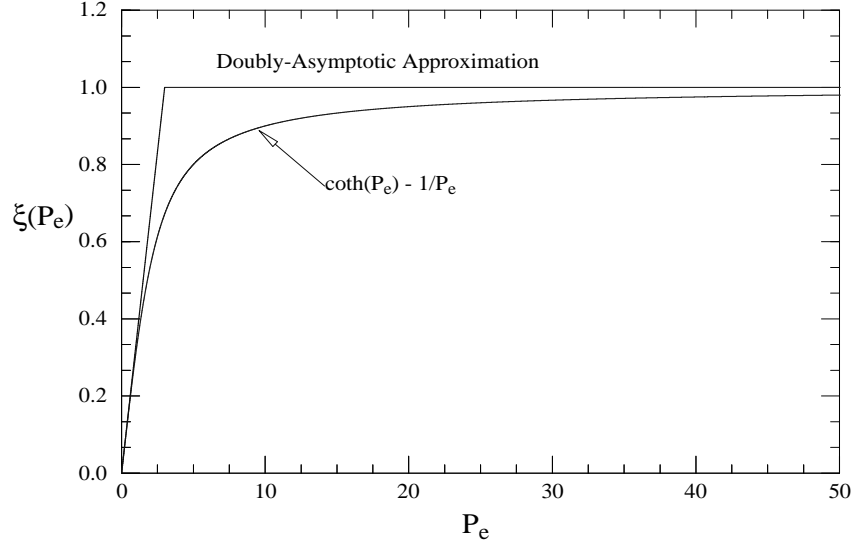


Figure 3.7: Doubly-asymptotic stabilization parameter for FEM-SUPG – see Tezduyar [26].

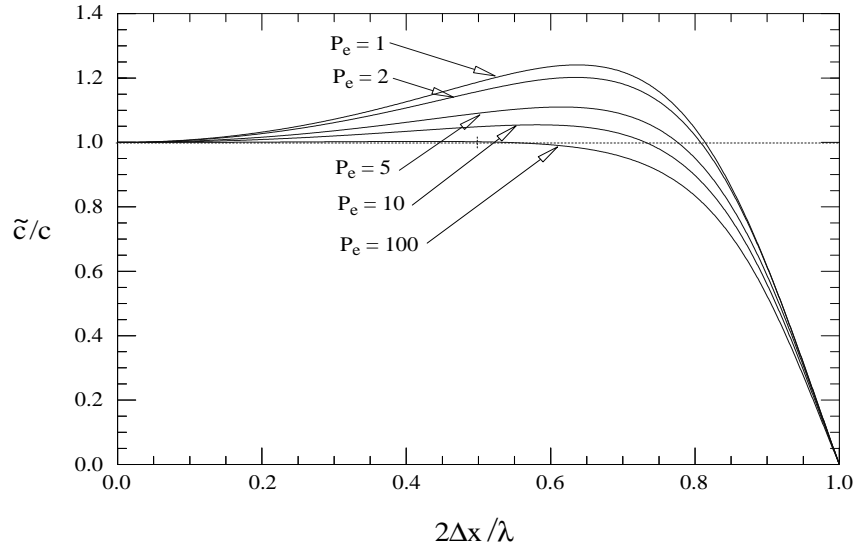


Figure 3.8: Non-dimensional phase speed for the finite element method with a consistent mass matrix and FEM-SUPG using  $\beta_{opt}$  and  $\xi = \coth(P_e) - 1/P_e$  for  $P_e = 1, 2, 5, 10, 100$ .



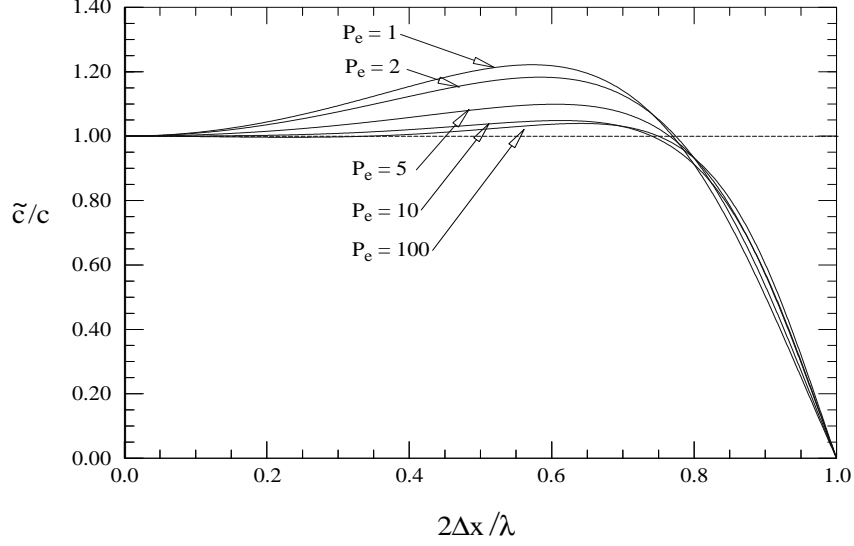


Figure 3.9: Non-dimensional phase speed for control-volume finite element method with a consistent mass matrix and SUCV with  $\beta = 1/2$  and  $\xi = \coth(\mathbf{P}_e) - 1/\mathbf{P}_e$  for  $\mathbf{P}_e = 1, 2, 5, 10, 100$ .

representations for SOU, Fromm, TOU and QUICK are given by

$$\frac{\tilde{c}}{c} \sim 1 - \frac{1}{6} \frac{n-8}{n-2} (k\Delta x)^2 \quad (3.3)$$

for  $n = 4, 6, 8$ , and  $10$ , respectively. These methods are 2nd-order, except for TOU which is 4th-order (with a leading coefficient of  $-1/30$ ). The asymptotic results for the finite-volume/finite-difference methods may be verified by forming the Taylor series approximations for the skew-symmetric parts of the advection operators.

**Remark.** The first-order upwind scheme yields a centered skew-symmetric second-order advection operator, and consequently the asymptotic estimate for the truncation error based on the phase speed yields  $O(\Delta x^2)$ .

For both FEM-SUPG and CVFEM-SUCV the asymptotic representation of the non-dimensional phase speed has the form

$$\frac{\tilde{c}}{c} \sim 1 + g_2(k\Delta x)^2 + g_4(k\Delta x)^4 + O((k\Delta x)^6). \quad (3.4)$$

In the limit of pure advection, i.e.,  $\mathbf{P}_e \rightarrow \infty$ ,  $g_2 \equiv 0$  as shown by Gresho and Sani [11] (see Eq. (2.6-180)) for FEM-SUPG. By choosing  $\beta = 1/\sqrt{15}$ ,

$$g_4 = \frac{\beta^2}{12} - \frac{1}{180}, \quad (3.5)$$

can also be made zero resulting in a 6th-order accurate method.

For SUCV  $g_2$  is independent of  $\beta$ , with an asymptotic representation of

$$\frac{\tilde{c}}{c} \sim 1 - \frac{1}{24}(k\Delta x)^2 + \left(\frac{\beta^2}{8} - \frac{7}{960}\right)(k\Delta x)^4 + O((k\Delta x)^6). \quad (3.6)$$

Therefore for SUCV there is no  $\beta$  that will result in a higher order formula or optimal phase speed behavior in terms of  $k\Delta x$ . However, a heuristically optimal value of  $\beta = 1/2$  gives a dispersion curve that approaches FEM-SUPG (see Figures 3.6 and 3.5) although the truncation error is only  $O(\Delta x^2)$  and there are lagging errors in the mid-range wavelengths.

If the lumped-mass approximation is applied to either FEM-SUPG or CVFEM-SUCV, i.e., row-sum-lumping of the original symmetric mass matrix, and not the skew-symmetric portion induced by the stabilization, the asymptotic truncation error reverts to,

$$\frac{\tilde{c}}{c} \sim 1 - \frac{1}{6}(k\Delta x)^2 + \left(\frac{\beta^2}{4} + \frac{1}{120}\right)(k\Delta x)^4 + O((k\Delta x)^6) \quad (3.7)$$

which for  $\beta = 0$  gives the formula for the centered finite difference scheme (equivalent to lumped mass FEM and CVFEM).

In addition to the asymptotic truncation error, the phase error analysis may be used to estimate the required resolution for a given level of “acceptable” error. The resolution requirements for a 5% and 1% error in phase are shown with the asymptotic truncation error estimates in Table 3.3. Estimates for resolution requirements for additional finite difference methods may be found in Gresho and Sani[11] (see pg. 155). The best phase accuracy for the least grid resolution is provided by FEM-SUPG with  $\beta_{opt}$  while the worst case is the second-order upwind method which, despite its second-order accuracy, requires more resolution than the first-order upwind method for an equivalent error.

Although the CVFEM variants yield competitive resolution estimates for the 5% error, as the error bands are tightened, the CVFEM methods do not perform as well as their FEM counterparts. This is due to the large lagging phase error thru the midrange of the discrete spectrum (see Figure 3.3) which results in an increase in the resolution requirement of from 3 to 5 relative to the finite element method. Ultimately, the CVFEM-SUCV method will require nearly an order of magnitude more resolution for the same accuracy as the FEM-SUPG method with the optimal stabilization chosen for each method.

Method	Asymptotic T.E.	$\lambda/\Delta x$ for	
		5% Error	1% Error
FOU	$O(\Delta x^2)$	11.4	25.6
SOU	$O(\Delta x^2)$	15.8	36.2
TOU	$O(\Delta x^4)$	5.46	8.35
QUICK	$O(\Delta x^2)$	6.83	13.5
Fromm's	$O(\Delta x^2)$	3.96	17.4
FEM – $\mathbf{M}_c$	$O(\Delta x^4)$	3.93	5.61
FEM – $\mathbf{M}_l$	$O(\Delta x^2)$	11.4	25.6
FEM - SUPG $\beta_{opt}$	$O(\Delta x^6)$	2.88	4.76
FEM - SUPG $\beta = 1/2$	$O(\Delta x^4)$	4.39	6.78
CVFEM – $\mathbf{M}_c$	$O(\Delta x^2)$	6.24	13.1
CVFEM – $\mathbf{M}_l$	$O(\Delta x^2)$	11.4	25.6
CVFEM - SUCV $\beta_{opt}$	$O(\Delta x^2)$	5.71	12.8
CVFEM - SUCV $\beta = 1/2$	$O(\Delta x^2)$	2.69	11.8

Table 3.3: Asymptotic estimates of truncation error and resolution requirements based on the phase error for pure advection. (Note that the FEM-SUPG and CVFEM-SUCV results are presented only for a consistent mass matrix  $\mathbf{M}_c$ .)

## 3.2 Group Speed

In one-dimension, the non-dimensional group velocity is

$$\tilde{v}_g = \frac{\partial \tilde{\omega}}{\partial k}. \quad (3.8)$$

For a non-dispersive medium, the group velocity is identical to the phase speed. However, as already discussed, the discretization procedures considered here result in a dispersive representation of the continuum problem, i.e., the phase speed is a function of the wavenumber. Thus, using Eq. (2.20), Eq. (3.8) may be written in terms of the wavelength-dependent phase speed as

$$\tilde{v}_g = \tilde{c}(k) + k \frac{\partial \tilde{c}}{\partial k}. \quad (3.9)$$

Therefore, the group speed will only be identical to the phase speed, the ideal situation, when

$$k \frac{\partial \tilde{c}}{\partial k} = 0. \quad (3.10)$$

This can occur in the limit as  $k \rightarrow 0$ , i.e., a constant mode, or when the slope of the phase curve with respect to the wavenumber is zero – a situation that we desire in the limit of  $k \rightarrow 0$ .

Indeed, methods like FEM and FEM-SUPG with a consistent mass matrix and the associated higher-order phase speed accuracy do a good job of emulating this behavior, but fail at the short wavelengths where the slope of the phase speed curve changes rapidly as the phase speed goes to zero at  $2\Delta x/\lambda = 1$ , the Nyquist limit. The consequence of this is reflected in the group speed which will become large and negative at the grid Nyquist limit. Thus, the better the phase speed behavior through the discrete spectrum, the worse the group speed will be for  $2\Delta x$  wavelengths. This is reflected in the results that follow. The fact that these unresolvable modes disperse rapidly from the main signal could be construed as an advantage.

The group speed results for all the methods considered here are shown in Table 3.4. The non-dimensional group speed for all of the finite difference methods are shown in Figure 3.10, the FEM group results are presented in Figure 3.11 – 3.13, while those for CVFEM are presented in Figure 3.14 – 3.16.

All of the methods considered here exhibit large negative group speed for  $2\Delta x$  wavelengths. The large leading phase errors for the second-order upwind (SOU) method are reflected in the large (relative to the other FD methods) leading group errors and the large negative group speed at the grid Nyquist limit. The negative group speed at the Nyquist limit is a direct consequence of the fact that the phase speed decreases rapidly with respect to wavenumber as the Nyquist limit ( $2\Delta x/\lambda$  is approached. Thus, for SOU, the leading phase error in the mid-range of the discrete spectrum leads to larger group for  $0.7 \leq 2\Delta x/\lambda \leq 1.0$  relative to the other FDM methods.

Similar effects are observed in general for the FEM and CVFEM methods, but are somewhat more pronounced for the consistent mass and SUPG/SUCV variants. Again, this is due to the fact that phase speed remains faithful to the physical phase velocity over a larger range of the discrete spectrum. For the FEM-SUPG method with  $\beta = 1/2$  for which  $\tilde{v}_g/c = -12$  for the  $2\Delta x$  wavelengths. The phase-error minimizing value of the stabilization parameter,  $\beta_{opt} = 1/\sqrt{15}$  reduces this large negative group velocity at the Nyquist limit.

Figure 3.12 shows the FEM-SUPG group speed for variable Peclet number, and Figure 3.13 shows the FEM-SUPG results using the Peclet number adjusted stabilization parameter. The effect of the Peclet number scaling is to reduce large negative group speed for  $\mathbf{P}_e \leq 2$ . Similar results for the CVFEM and CVFEM-SUCV methods may be seen in Figures 3.14 – 3.16.

## Asymptotic Truncation Error and Resolution Estimates

Asymptotic truncation error in the group speed can be determined by taking the limit as  $k\Delta x \rightarrow 0$  in the analytical expressions given in Table 3.4. The

Method	Group Speed ( $\tilde{v}_g/c$ )
FOU	$\cos(k\Delta x)$
SOU	$2\cos(k\Delta x) - \cos(2k\Delta x)$
TOU	$\frac{1}{3}[4\cos(k\Delta x) - \cos(2k\Delta x)]$
QUICK	$\frac{1}{4}[5\cos(k\Delta x) - \cos(2k\Delta x)]$
Fromm's	$\frac{1}{2}[3\cos(k\Delta x) - \cos(2k\Delta x)]$
FEM	$\frac{3(1+2\cos(k\Delta x))}{(2+\cos(k\Delta x))^2}$
FEM-SUPG	$\frac{[\mathcal{M}(k\Delta x) + (2\beta^2 + \beta/\mathbf{P}_e)(1 - \cos(k\Delta x))]\left[\frac{4}{9} + \frac{1}{12}(7 - 3\beta^2)\cos(k\Delta x) + \frac{(9\beta^2 - 1)}{36}\cos 3(k\Delta x)\right]}{(\mathcal{M}^2(k\Delta x) + \beta^2 \sin^2(k\Delta x))^2}$
CVFEM	$+ \left(\frac{\beta}{\mathbf{P}_e} + 2\beta^2 - \frac{1}{3}\right) \frac{\sin^2(k\Delta x)}{\mathcal{M}^2(k\Delta x) + \beta^2 \sin^2(k\Delta x)}$
CVFEM-SUCV	$\frac{4(1+3\cos(k\Delta x))}{(3+\cos(k\Delta x))^2}$
	$\frac{[\mathcal{M}(k\Delta x) + (2\beta^2 + \beta/\mathbf{P}_e)(1 - \cos(k\Delta x))]\left[\frac{3}{8} + \frac{(41 - 16\beta^2)}{64}\cos(k\Delta x) + \frac{(16\beta^2 - 1)}{64}\cos 3(k\Delta x)\right]}{(\mathcal{M}^2(k\Delta x) + \beta^2 \sin^2(k\Delta x))^2}$
	$+ \left(\frac{\beta}{\mathbf{P}_e} + 2\beta^2 - \frac{1}{4}\right) \frac{\sin^2(k\Delta x)}{\mathcal{M}^2(k\Delta x) + \beta^2 \sin^2(k\Delta x)}$

Table 3.4: Formulae for one-dimensional group speed.

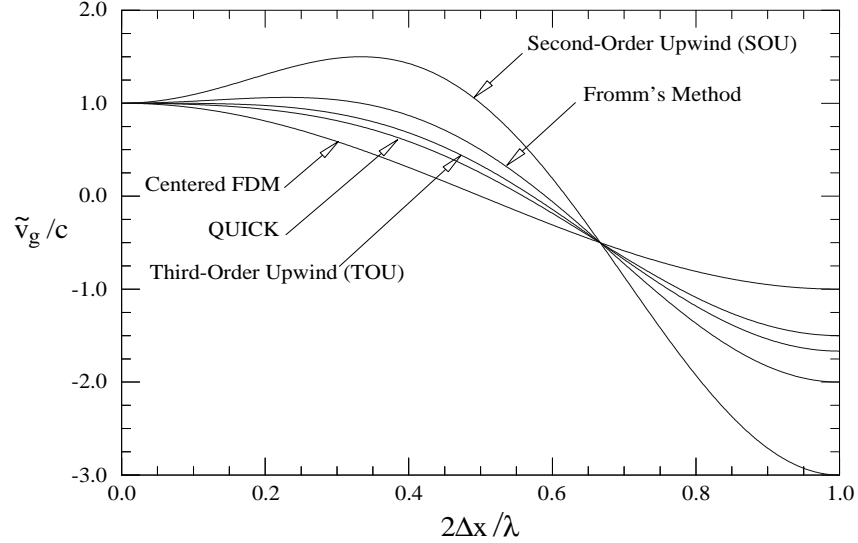


Figure 3.10: Non-dimensional group speed for a variety of finite-difference (node-centered finite-volume) methods.

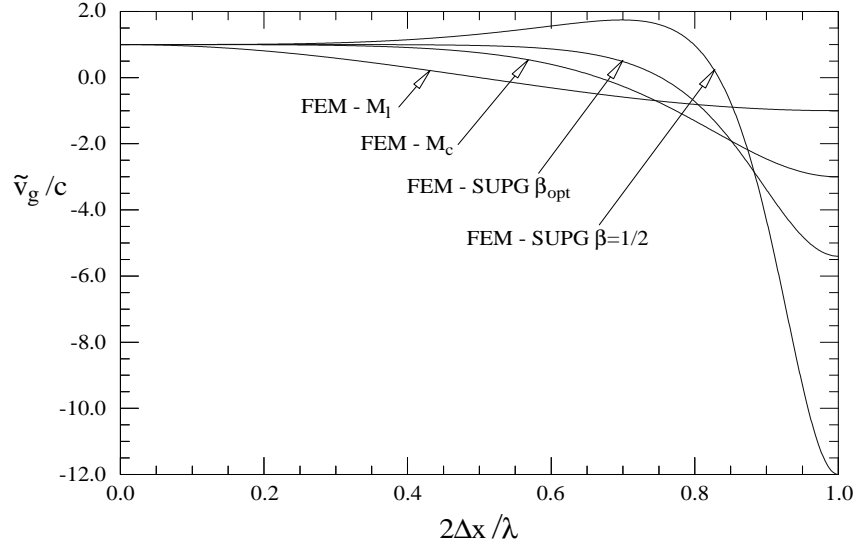


Figure 3.11: Non-dimensional group speed for finite element method using a consistent mass matrix (FEM -  $\mathbf{M}_c$ ), lumped mass (FEM -  $\mathbf{M}_l$ ), consistent mass matrix and SUPG with  $\beta_{opt}$  and  $\beta = 1/2$ .

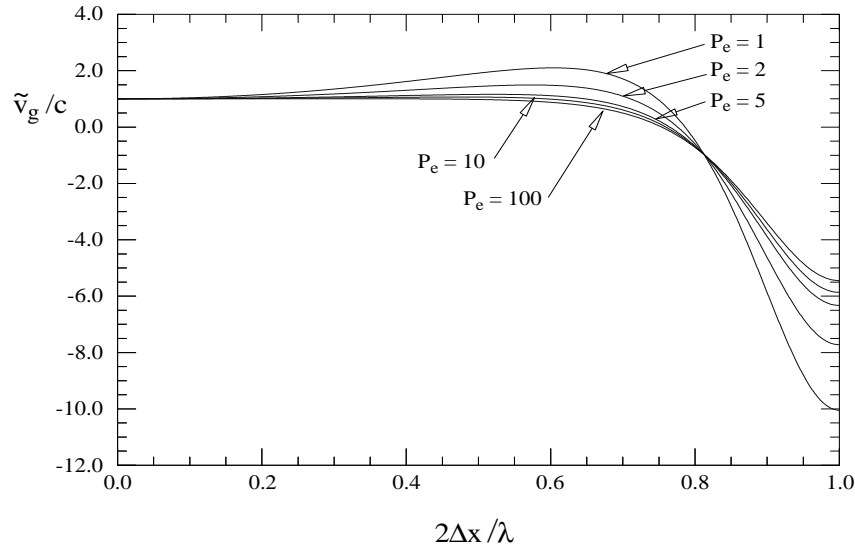


Figure 3.12: Non-dimensional group speed for finite element method using a consistent mass matrix and SUPG with  $\beta_{opt}$  for  $P_e = 1, 2, 5, 10, 100$ .

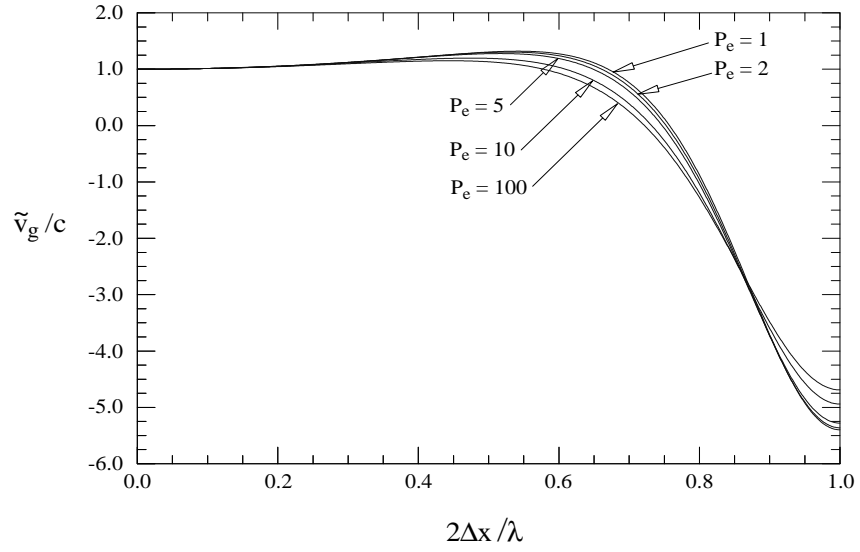


Figure 3.13: Non-dimensional group speed for finite element method using a consistent mass matrix and SUPG using  $\beta_{opt}$  and  $\xi = \coth(\mathbf{P}_e) - 1/\mathbf{P}_e$  for  $\mathbf{P}_e = 1, 2, 5, 10, 100$ .

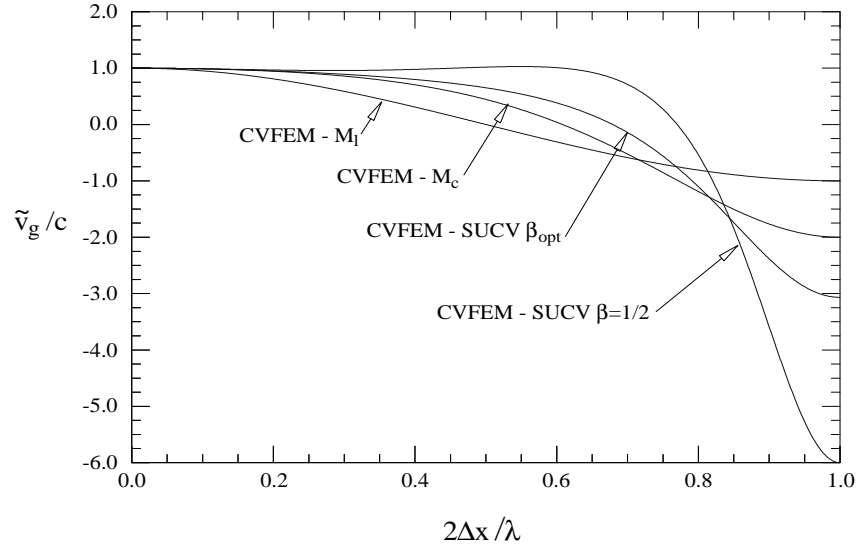


Figure 3.14: Non-dimensional group speed for control-volume finite element method using a consistent mass matrix (CVFEM -  $\mathbf{M}_c$ ), lumped mass (CVFEM -  $\mathbf{M}_l$ ), consistent mass matrix and SUCV with  $\beta_{opt}$  and  $\beta = 1/2$ .

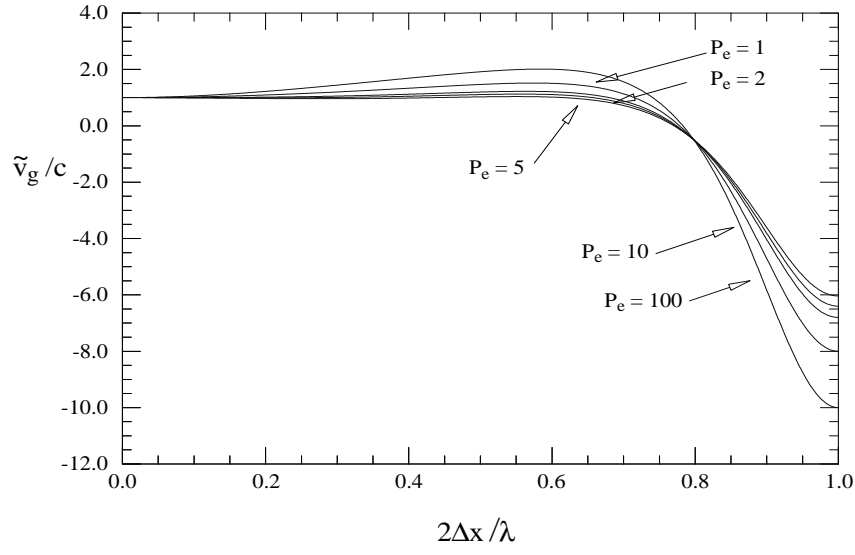


Figure 3.15: Non-dimensional group speed for control-volume finite element method with a consistent mass matrix and SUCV with  $\beta = 1/2$  for  $\mathbf{P}_e = 1, 2, 5, 10, 100$ .

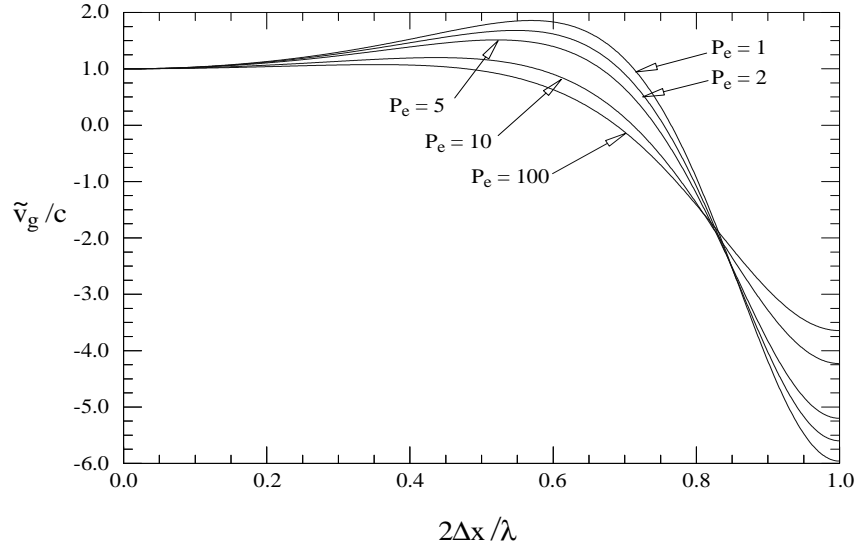


Figure 3.16: Non-dimensional group speed for control-volume finite element method using a consistent mass matrix and SUCV with  $\beta = 1/2$  and  $\xi = \coth(\mathbf{P}_e) - 1/\mathbf{P}_e$  for  $\mathbf{P}_e = 1, 2, 5, 10, 100$ .



first and second-order upwind methods are both  $O(\Delta x^2)$  in group speed. The asymptotic form of the group speed for Fromm, TOU and QUICK is

$$\frac{v_g}{c} \sim 1 + \frac{1}{2} \frac{4-n}{n-1} (k\Delta x)^2, \quad (3.11)$$

for  $n = 3, 4$  and  $5$ , respectively. Thus, Fromm and QUICK are also second order in group, while TOU is 4th order (with a coefficient of  $-1/6$ ).

For FEM-SUPG the asymptotic group speed representation is,

$$\frac{v_g}{c} \sim 1 + \frac{3\beta}{2\mathbf{P}_e} (k\Delta x)^2 + \frac{15\beta - 180\beta^2 + 2\mathbf{P}_e(15\beta^2 - 1)}{72\mathbf{P}_e} (k\Delta x)^4. \quad (3.12)$$

For  $\beta_{opt}$  and infinite  $\mathbf{P}_e$ , the group speed is 6th-order accurate – similar to the phase speed.

For  $\beta = 0$ , the asymptotic representation for FEM is recovered,

$$\frac{v_g}{c} \sim 1 - \frac{1}{36} (k\Delta x)^4, \quad (3.13)$$

which is 4th-order accurate.

For SUCV the asymptotic representation is

$$\frac{v_g}{c} \sim 1 + \left( \frac{3\beta}{2\mathbf{P}_e} - \frac{1}{8} \right) (k\Delta x)^2 + \left( \frac{-7}{192} + \frac{5\beta^2}{8} - \frac{5\beta^2}{2\mathbf{P}_e} \right) (k\Delta x)^4. \quad (3.14)$$

For  $\beta = 0$  the asymptotic representation of group speed for CVFEM is recovered,

$$\frac{v_g}{c} \sim 1 - \frac{1}{8} (k\Delta x)^2 - \frac{7}{192} (k\Delta x)^4. \quad (3.15)$$

Both CVFEM and CVFEM-SUCV are second-order accurate in the group speed.

The resolution requirements for a 5% and 1% error in group speed are shown with the asymptotic truncation error estimates in Table 3.5. The best group speed accuracy for the least grid resolution is provided by FEM-SUPG with  $\beta_{opt}$  while the worst case is the second-order upwind method which, despite its second-order accuracy, requires more resolution than the first-order upwind method. Again, the CVFEM method exhibits reasonable resolution requirements for a 5% error in the group. However, for a 1% error, the resolution requirements increase significantly due to lagging group speed in the midrange of the discrete spectrum. For CVFEM-SUCV with  $\beta = 1/2$ , the resolution requirements are about a factor of 4 times higher than for the FEM-SUPG method with the optimal stabilization parameter – a factor of 16 more in three dimensions for equivalent error.

Method	Asymptotic T.E.	$\lambda/\Delta x$ for	
		5% Error	1% Error
FOU	$O(\Delta x^2)$	19.7	44.4
SOU	$O(\Delta x^2)$	27.7	62.7
TOU	$O(\Delta x^4)$	8.29	12.6
QUICK	$O(\Delta x^2)$	11.2	22.9
Fromm's	$O(\Delta x^2)$	11.8	30.8
FEM – $\mathbf{M}_c$	$O(\Delta x^4)$	5.70	8.31
FEM – $\mathbf{M}_l$	$O(\Delta x^2)$	19.7	44.4
FEM - SUPG $\beta_{opt}$	$O(\Delta x^6)$	3.75	4.62
FEM - SUPG $\beta = 1/2$	$O(\Delta x^4)$	6.70	10.3
CVFEM – $\mathbf{M}_c$	$O(\Delta x^2)$	10.4	22.5
CVFEM – $\mathbf{M}_l$	$O(\Delta x^2)$	19.7	44.4
CVFEM - SUCV $\beta_{opt}$	$O(\Delta x^2)$	9.88	22.2
CVFEM - SUCV $\beta = 1/2$	$O(\Delta x^2)$	3.13	21.3

Table 3.5: Asymptotic estimates of truncation error and resolution requirements based on the group error for pure advection. (Note that the SUPG and SUCV results are presented only for a consistent mass matrix  $\mathbf{M}_c$ .)

### 3.3 Discrete Diffusivity

Attention is now turned to the behavior of the discrete, wavelength-dependent diffusivity. The process of discretization introduces a wavelength dependence into the discrete thermal diffusivity even when a constant thermal diffusivity is prescribed for the continuum. The wavelength dependent behavior of the discrete diffusivity indicates that individual modes that comprise a temperature profile will diffuse at different rates. The degree to which the rate of diffusion varies with wavelength is a function of the method chosen.

The formulae for the non-dimensional discrete diffusivity are presented in Table 3.6. All of the finite difference and finite volume methods use second-order centered approximations for the diffusion operator and yield identical discrete diffusivities as indicated by the single FDM/FVM entry in Table 3.6. The FEM/CVFEM ( $\beta = 0$ ) with lumped mass matrix ( $\mathcal{M}(k\Delta x) = 1$ ) also revert to the FDM/FVM formula.

The non-dimensional discrete diffusivity for the FEM, CVFEM (and FDM) methods are presented in Figure 3.17, and the results for FEM-SUPG and CVFEM-SUCV are presented in Figure 3.18. The ideal non-dimensional discrete diffusivity would be unity for the entire discrete wavelength spectrum. Thus, the deviation of the non-dimensional discrete diffusivity  $\tilde{\alpha}/\alpha$  from unity may be interpreted as an error in discrete diffusivity relative to

Method	Discrete Diffusivity ( $\tilde{\alpha}/\alpha$ )
FDM / FVM	$2 [1 - \cos(k\Delta x)] / (k\Delta x)^2$
FEM / CVFEM	$\frac{2\mathcal{M}(k\Delta x)(1 - \cos(k\Delta x))}{(k\Delta x)^2[\mathcal{M}^2(k\Delta x) + \beta^2 \sin^2(k\Delta x)]}$

Table 3.6: Formulae for one-dimensional discrete diffusivity.

the continuum value of the diffusivity.

The consistent mass FEM method (FEM- $\mathbf{M}_c$ ) exhibits an over-diffusive nature over the entire discrete spectrum, and the consistent mass CVFEM method (CVFEM- $\mathbf{M}_c$ ) is over-diffusive in the mid-range of the discrete spectrum. In contrast, the process of mass lumping yields discrete diffusivities for FEM and CVFEM that are under-diffusive for all discrete wavelengths. The FEM-SUPG and CVFEM-SUCV methods exhibit a sensitivity to the magnitude of the stabilization parameter,  $\beta$ . This demonstrates that a phase-error minimizing optimal value of the stabilization parameter for pure advection is not an optimal choice for thermal diffusion.

The finite volume schemes considered all share a common second-order centered discretization representation of the diffusion term in Eq. (2.1) with an  $O(\Delta x^2)$  truncation error as shown in Table 3.7. In one-dimension, the lumped-mass FEM, lumped-mass CVFEM, and node-centered finite volume schemes all yield equivalent discrete diffusivities (Figure 3.17). Thus, the discrete diffusivity for FOU, SOU, TOU, etc. will be the same as the lumped mass result of Figure 3.17. Similarly, a node-centered finite volume scheme that introduces a consistent mass matrix yields a discrete diffusivity that is identical to the FEM method with a consistent mass. Note that the consistent mass CVFEM and CFEM-SUCV (with  $\beta_{opt}$ ) schemes yield the least error over the spectrum of dimensionless wave number (see Figures 3.17 and 3.18).

### Asymptotic Truncation Error and Resolution Estimates

The asymptotic truncation error estimates for discrete diffusivity are summarized in Table 3.7. The mass-lumped FVM (or FDM) methods considered all share the same central difference approximation for the diffusion, resulting in the following asymptotic representation of discrete diffusivity

$$\frac{\tilde{\alpha}}{\alpha} \sim 1 - \frac{1}{12}(k\Delta x)^2 + \frac{1}{360}(k\Delta x)^4. \quad (3.16)$$

For FEM-SUPG (and FEM when  $\beta = 0$ ), the asymptotic formula for the discrete diffusivity is

$$\frac{\tilde{\alpha}}{\alpha} \sim 1 - \left(\beta^2 - \frac{1}{12}\right)(k\Delta x)^2 + \left(\beta^4 - \frac{1}{12}\beta^2 + \frac{1}{360}\right)(k\Delta x)^4. \quad (3.17)$$

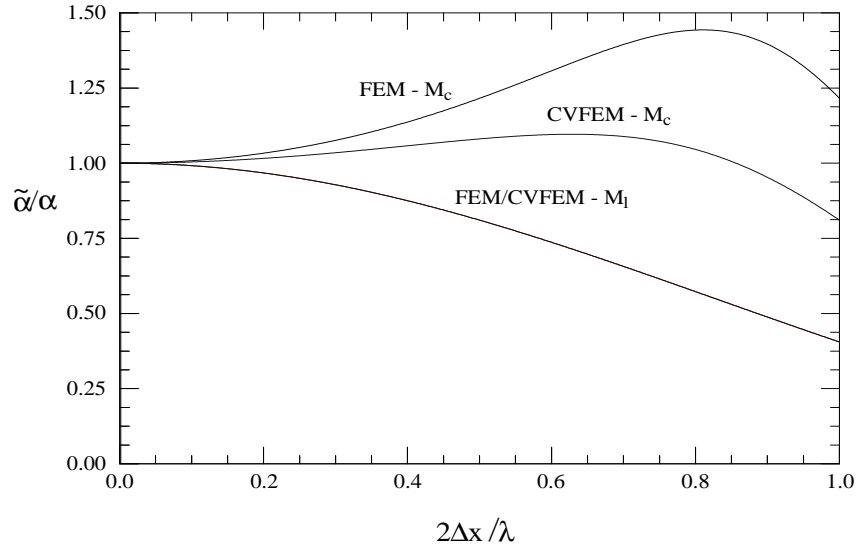


Figure 3.17: Non-dimensional discrete diffusivity for Galerkin finite element (FEM) and control-volume finite element methods (CVFEM).

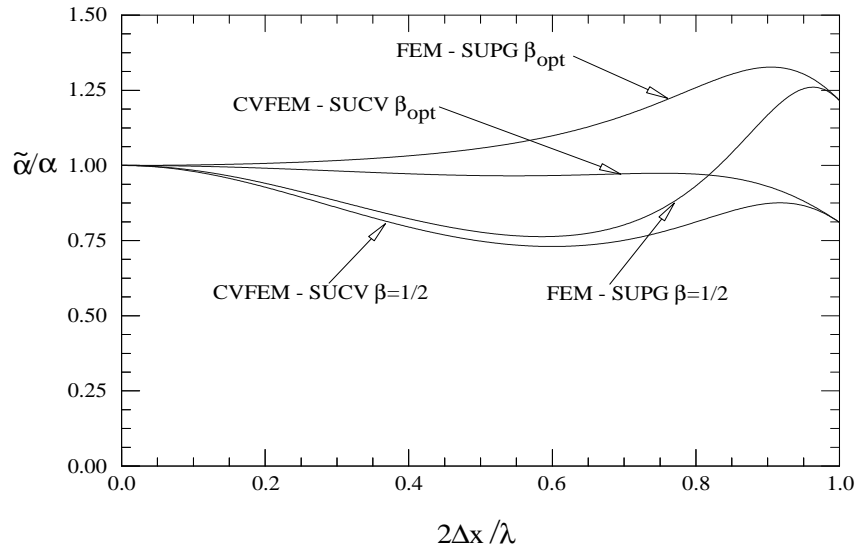


Figure 3.18: Non-dimensional discrete diffusivity for FEM with SUPG and CVFEM with SUCV.

Method	Asymptotic T.E.	$\lambda/\Delta x$ for	
		5% Error	1% Error
FDM – Centered			
FEM – $\mathbf{M}_l$	$O(\Delta x^2)$	8.03	18.1
CVFEM – $\mathbf{M}_l$			
FEM – $\mathbf{M}_c$	$O(\Delta x^2)$	8.19	18.2
FEM-SUPG ( $\beta_{opt}$ )	$O(\Delta x^2)$	4.20	8.37
FEM-SUPG ( $\beta = 1/2$ )	$O(\Delta x^2)$	11.0	25.5
CVFEM – $\mathbf{M}_c$	$O(\Delta x^2)$	5.45	12.8
CVFEM-SUCV ( $\beta_{opt}$ )	$O(\Delta x^2)$	2.30	9.52
CVFEM-SUCV ( $\beta = 1/2$ )	$O(\Delta x^2)$	12.3	28.4

Table 3.7: Asymptotic estimates of truncation error and resolution requirements based on the discrete diffusivity for thermal diffusion.

For CVFEM-SUCV (and CVFEM when  $\beta = 0$ ), the asymptotic form of the discrete diffusivity is

$$\frac{\tilde{\alpha}}{\alpha} \sim 1 - \left( \beta^2 - \frac{1}{24} \right) (k\Delta x)^2 + \left( \beta^4 + \frac{1}{24}\beta^2 - \frac{7}{2880} \right) (k\Delta x)^4. \quad (3.18)$$

All of the finite-element based methods are 2nd-order for discrete diffusivity. CVFEM has the smallest leading coefficient.

Finally, use of a lumped mass matrix (lumping the original mass matrix only) with FEM-SUPG or CVFEM-SUCV stabilization yields the following discrete diffusivity

$$\frac{\tilde{\alpha}}{\alpha} \sim 1 - \left( \beta^2 + \frac{1}{12} \right) (k\Delta x)^2 + \left( \beta^4 + \frac{5}{12}\beta^2 + \frac{1}{360} \right) (k\Delta x)^4, \quad (3.19)$$

which is identical to the discrete diffusivity for the centered difference method for  $\beta = 0$ .

The resolution requirements for a 5% and 1% error in discrete diffusivity are shown with the asymptotic truncation error estimates in Table 3.7. The best diffusivity accuracy for the least grid resolution is provided by FEM-SUPG (in term of the 1% error) with  $\beta_{opt}$ . The worst accuracy is obtained with the  $\beta = 1/2$  CVFEM-SUCV formulation with more than 28 grid points required per wavelength to yield a discrete diffusivity error of 1%. Nearly as bad is the FEM-SUPG,  $\beta = 1/2$  formulation.

### 3.4 Artificial Diffusivity

Artificial diffusion can be added to a method either explicitly, e.g., via an explicit second-order or fourth-order operator, or it can be a by-product of

Method	Artificial Diffusivity ( $(\mathbf{P}_e^{art})^{-1} = 2\alpha_{art}/c\Delta x$ )
FOU	$2[1 - \cos(k\Delta x)]/(k\Delta x)^2$
SOU	$[3 + \cos(2k\Delta x) - 4\cos(k\Delta x)]/(k\Delta x)^2$
TOU	$[3 + \cos(2k\Delta x) - 4\cos(k\Delta x)]/3(k\Delta x)^2$
QUICK	$[3 + \cos(2k\Delta x) - 4\cos(k\Delta x)]/4(k\Delta x)^2$
Fromm's	$[3 + \cos(2k\Delta x) - 4\cos(k\Delta x)]/2(k\Delta x)^2$
FEM / CVFEM	$\frac{4\beta[\mathcal{M}(k\Delta x)(1 - \cos(k\Delta x)) - \sin^2(k\Delta x)/2]}{(k\Delta x)^2[\mathcal{M}^2(k\Delta x) + \beta^2 \sin^2(k\Delta x)]}$

Table 3.8: Formulae for one-dimensional artificial diffusivity.

an upwind advective discretization (e.g., first-order upwinding). Although in general artificial diffusion is not a desirable feature of a method, it can be useful in removing unwanted numerical artifacts such as high frequency dispersion errors in convection-dominated problems. For hyperbolic conservation laws, i.e., pure advection in the context of this work, a “properly tuned” artificial viscosity can be used to select the appropriate weak physical solution when non-smooth data is present.

The formulae for dimensionless artificial diffusion as a function of dimensionless wavenumber are shown in Table 3.8 for all the methods considered here.<sup>2</sup> In our opinion, an ideal artificial diffusivity should only be active in the high-frequency, short-wavelength portion of the discrete spectrum, near the Nyquist grid limit for example, and be negligible otherwise. In this respect, Figure 3.19, which shows artificial diffusion for the FDM methods, illustrates the well-known problem with the first-order-upwind method. It behaves in the opposite manner to the ideal, maximizing the artificial diffusion as the grid is refined ( $k\Delta x \rightarrow 0$ ). The higher order finite difference methods approximate the desired spectral behavior, although they produce rather large amounts of artificial diffusion even in the mid-range frequencies when compared to the FEM-based methods shown in Figure 3.20. These methods come closest to the ideal spectral behavior, with artificial diffusion remaining small (relative to its value at the Nyquist limit) until  $2\Delta x/\lambda > 0.7$  permitting the signals with “good” phase behavior to survive the side-effects of the artificial diffusivity. The central difference method, FEM, and CVFEM contain no artificial diffusion and hence do not appear in these figures.

### Asymptotic Truncation Error Estimates

The order of truncation error in the artificial diffusivity for the various methods is shown in Table 3.9. The order of truncation error indicates how quickly

---

<sup>2</sup>A factor of 1/2 is missing in the  $\sin^2 k\Delta x$  term in the numerator of the artificial diffusion formula given in Gresho and Sani [11] for FEM (see Eq. 2.6-78).

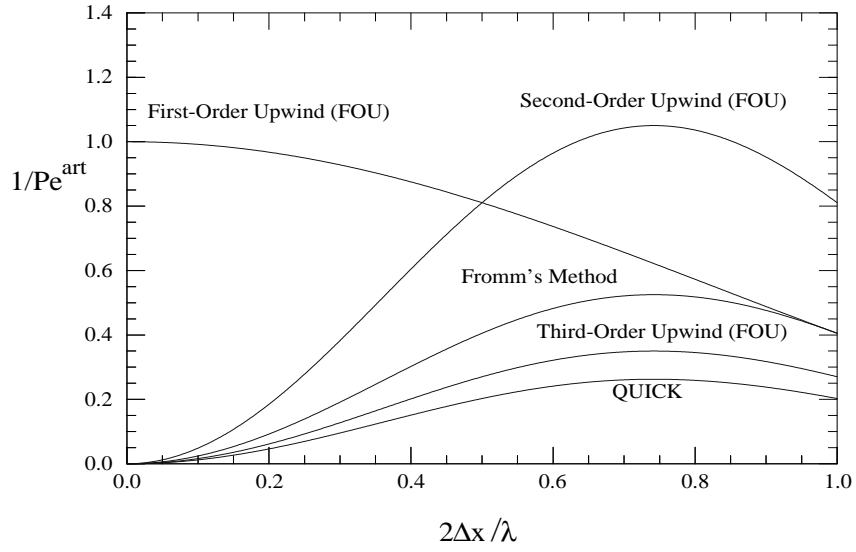


Figure 3.19: Non-dimensional artificial diffusivity for a variety of finite-difference (node-centered finite-volume) methods.

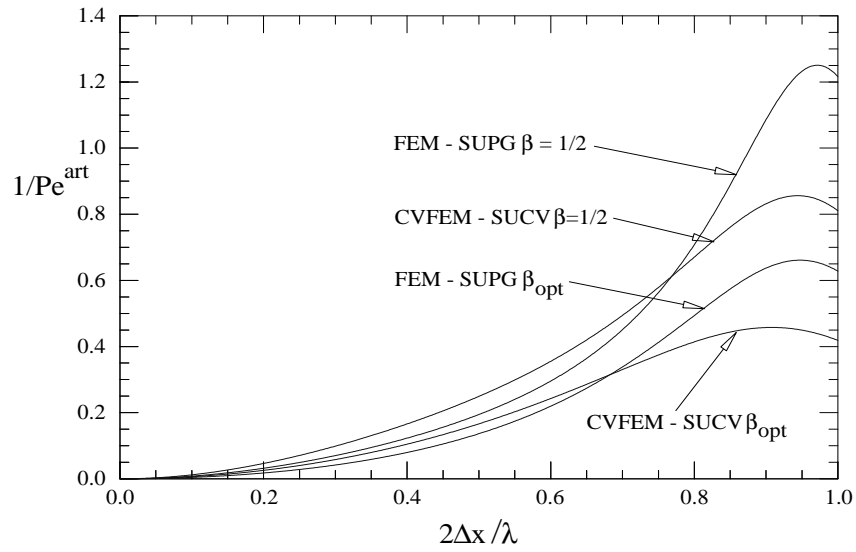


Figure 3.20: Non-dimensional artificial diffusivity for FEM-SUPG and CVFEM-SUCV.

the artificial diffusivity approaches zero as a function of the non-dimensional wave number.

Recall that the non-dimensional artificial diffusivity may be written as

$$\frac{1}{\mathbf{P}_e^{art}} = \frac{2\alpha_{art}}{c\Delta x}. \quad (3.20)$$

The asymptotic representation of dimensionless artificial diffusivity for first-order upwind (FOU) is identical to the dimensionless discrete diffusivity in Eq. (3.16),

$$\frac{2\alpha_{art}}{c\Delta x} \sim 1 - \frac{1}{12}(k\Delta x)^2 + \frac{1}{360}(k\Delta x)^4. \quad (3.21)$$

However, here the constant (unity) leading term in the asymptotic expansion indicates that the artificial viscosity approaches a constant quantity independent of  $k\Delta x$ . As demonstrated by the artificial viscosity results for FOU in Figure 3.19, a fixed amount of artificial viscosity is present even in the as  $\Delta x \rightarrow 0$ . Thus, a first-order upwind approximation yields an inconsistent approximation to the pure advection problem, albeit a consistent approximation for some advection-diffusion problem with finite diffusivity.

The asymptotic expansion for SOU, Fromm, TOU and QUICK is

$$\frac{2\alpha_{art}}{c\Delta x} \sim \frac{1}{n} \left( \frac{1}{2}(k\Delta x)^2 - \frac{1}{12}(k\Delta x)^4 + \frac{1}{160}(k\Delta x)^6 \right) \quad (3.22)$$

for  $n=1,2,3$  and 4, respectively. In contrast to FOU, these methods are all 2nd-order. Recall that central difference, FEM and CVFEM introduce no artificial diffusion. The asymptotic form for FEM-SUPG is

$$\frac{2\alpha_{art}}{c\Delta x} \sim 4\beta \left[ \frac{(k\Delta x)^2}{24} + \frac{1}{144} (1 - 6\beta^2) (k\Delta x)^4 + O((k\Delta x)^6) \right]. \quad (3.23)$$

Using the optimal value of  $\beta (= 1/\sqrt{15})$ , the formula becomes,

$$\frac{2\alpha_{art}}{c\Delta x} = \frac{1}{\sqrt{15}} \left[ \frac{(k\Delta x)^2}{6} + \frac{(k\Delta x)^4}{60} \right]. \quad (3.24)$$

For CVFEM-SUCV, the asymptotic form is

$$\frac{2\alpha_{art}}{c\Delta x} \sim 4\beta \left[ \frac{(k\Delta x)^2}{16} + \frac{1}{192} (1 - 12\beta^2) (k\Delta x)^4 + O((k\Delta x)^6) \right]. \quad (3.25)$$

Using  $\beta = 1/2$ , which is near-optimal for dispersion, the formula becomes

$$\frac{2\alpha_{art}}{c\Delta x} = \frac{(k\Delta x)^2}{8} - \frac{(k\Delta x)^4}{48} \quad (3.26)$$



Method	Asymptotic T.E.
FOU	$O(1)$
SOU	$O(\Delta x^2)$
TOU	$O(\Delta x^2)$
QUICK	$O(\Delta x^2)$
Fromm's	$O(\Delta x^2)$
FEM - SUPG $\beta_{opt}$	$O(\Delta x^2)$
FEM - SUPG $\beta = 1/2$	$O(\Delta x^2)$
CVFEM - SUCV $\beta_{opt}$	$O(\Delta x^2)$
CVFEM - SUCV $\beta = 1/2$	$O(\Delta x^2)$

Table 3.9: Asymptotic estimates of truncation error for artificial diffusivity.

Thus, even though they are both 2nd-order, FEM-SUPG has the smaller leading coefficient; this is reflected in Figure 3.20.

Finally, if the mass matrix is lumped in either of SUPG or SUCV prior to applying the stabilization schemes, we get

$$\frac{2\alpha_{art}}{c\Delta x} \sim \frac{\beta}{2} \left[ (k\Delta x)^2 - \left( \frac{1}{6} + \beta^2 \right) (k\Delta x)^4 + O((k\Delta x)^6) \right]. \quad (3.27)$$

### 3.5 Effects of Artificial Diffusivity

The effect of wavenumber dependent artificial diffusivity on the quadratic temperature,  $QT$ , is outlined in this section. Damping of quadratic temperature is presented here in terms of the incremental quadratic temperature,  $\Delta QT$  (as developed for the second-order upwind method). Recall  $\Delta QT = -1$  indicates that a signal is completely damped over the advective time scale,  $\tau = \Delta x/c$  and is undisturbed if  $\Delta QT = 0$ .

As noted above, an ideal artificial diffusivity (and hence energy damping) should only be active in the high-frequency, short-wavelength portion of the discrete spectrum. In this respect, Figure 3.21, which shows  $\Delta QT$  for the FDM methods, illustrates that this general behavior is respected. The higher order SOU and Fromm's methods approximate the desired spectral behavior, although they produce rather large amounts of damping even in the mid-range frequencies when compared to the FEM-based methods shown in Figure 3.22. Conversely, QUICK and TOU both perform quite well in the low frequency range, but do not completely damp high-frequency signals ( $2\Delta x/\lambda = 1$ ) over the advective time-scale.

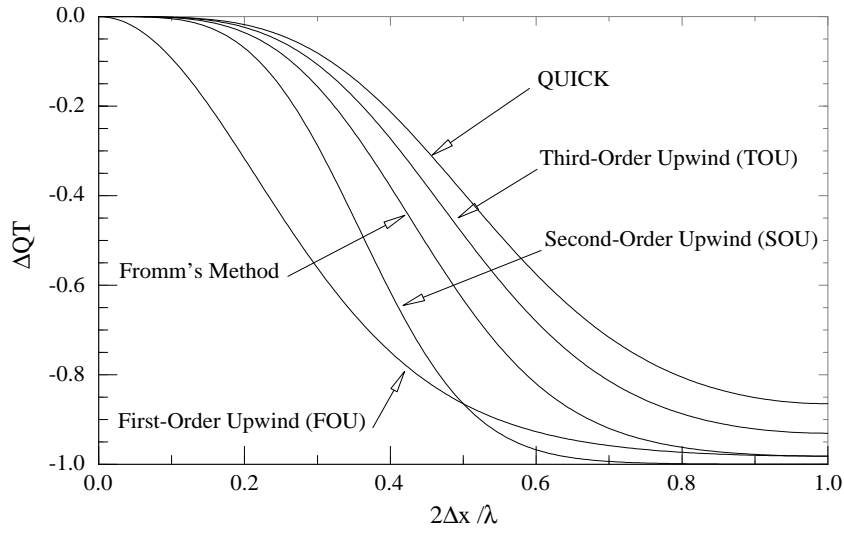


Figure 3.21: Non-dimensional change in incremental quadratic temperature,  $\Delta QT$ , for a variety of finite-difference (node-centered finite-volume) methods.

In contrast, The FEM-based schemes appear to be nearly ideal (relative to the other methods presented here), with modest damping at low-frequencies, long-wavelengths, complete damping of the high-frequency, short-wavelength signals and a smooth transition in the mid-frequency range. Again, an assessment of the “best” damping characteristics depends on the complex interplay between artificial diffusivity, phase and group speeds.

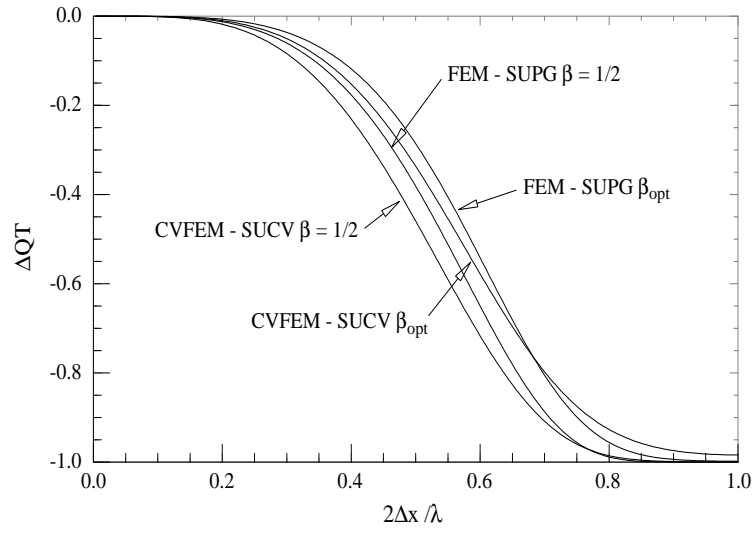


Figure 3.22: Non-dimensional change in incremental quadratic temperature,  $\Delta QT$ , for FEM-SUPG and CVFEM-SUCV with  $\beta = \beta_{opt}$  and  $1/2$ .



# Chapter 4

## Two-Dimensional Results

This chapter presents the two-dimensional discrete phase speed, and discrete and artificial diffusivities for the finite difference, finite volume and finite element methods outlined in §2.3. For these methods, the effect of grid aspect ratio,  $\gamma = \Delta y/\Delta x$ , on the noted numerical artifacts is examined for the range of discrete dimensionless wavenumber. Metrics which provide integrated (over  $\theta$  and  $2\Delta x/\lambda$ ) measures of anisotropy and error are introduced to allow for a quantitative methods comparison.

Relative to the one-dimensional results of Chapter 3, the 2-D results add propagation direction,  $\theta$ , to the parameter space. The addition of  $\theta$  significantly increases the complexity of the phase speed and diffusivity results. (The group speed direction,  $\Theta$ , is also a relevant parameter, but the associated analyses are not included here due to space limitations.) In order to present these results, polar plots are used as shown by the representative plot of phase speed (on a unit aspect ratio grid) in Figure 4.1.

Here, the non-dimensional phase speed,  $\tilde{c}/c$ , is associated with the radial coordinate, and the propagation direction,  $\theta$ , by the azimuthal coordinate. Polar curves at fixed non-dimensional wavenumber are plotted with each curve representing the dimensionless phase speed for that wavenumber. In this work, curves at  $2\Delta x/\lambda = 0, 0.2, 0.4, 0.6, 0.8$  and  $1.0$  are plotted on each polar plot. Figure 4.1 clearly demonstrates the anisotropic behavior (i.e.,  $\theta$  dependence) of the non-dimensional phase speed as  $\tilde{c}/c$  varies with propagation direction,  $\theta$ . For this example, the anisotropy becomes more pronounced as dimensionless wavenumber increases from 0 to 1.

### 4.1 Metrics

Although polar plots such as that shown in Figure 4.1 suggest the degree of anisotropy and accuracy of an individual method, a quantitative comparison is desired. For this reason, two metrics are introduced. The first metric is

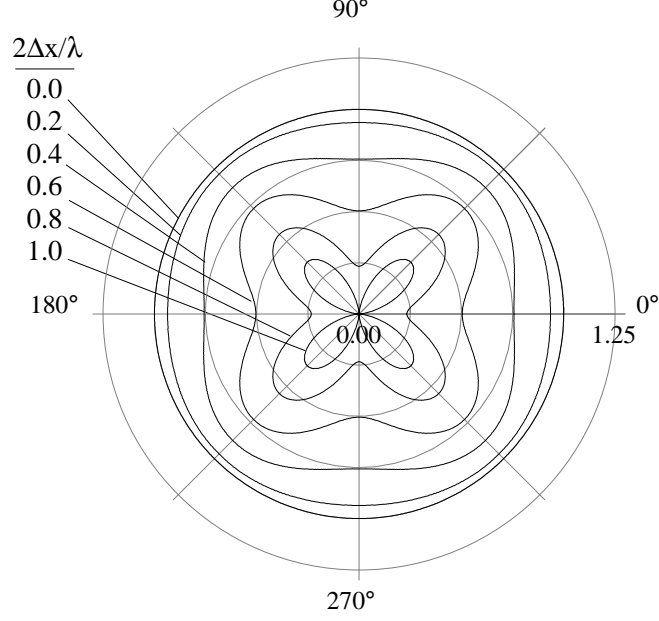


Figure 4.1: Non-dimensional phase speed ( $\tilde{c}/c$ ; radial coordinate) as a function of  $\theta$  (azimuthal coordinate).

the coefficient of variation,

$$\varsigma(2\Delta x/\lambda) = \frac{\sigma(2\Delta x/\lambda)}{\overline{G(2\Delta x/\lambda)}}, \quad (4.1)$$

which provides a measure of the anisotropy of a method for a given dimensionless wavenumber. In Eq. (4.1),  $G$  is a generic variable representing  $\tilde{c}/c$ ,  $\tilde{\alpha}/\alpha$  or  $1/\mathbf{P}_e^{art}$  while,

$$\overline{G(2\Delta x/\lambda)} = \frac{1}{2\pi} \int_0^{2\pi} G(2\Delta x/\lambda, \theta) d\theta \quad (4.2)$$

is its mean and,

$$\sigma(2\Delta x/\lambda) = \sqrt{\frac{1}{2\pi} \int_0^{2\pi} \left( G(2\Delta x/\lambda, \theta) - \overline{G(2\Delta x/\lambda)} \right)^2 d\theta} \quad (4.3)$$

its standard deviation at some  $2\Delta x/\lambda$ .

It is clear from Eq. (4.1) – (4.3) that an isotropic scheme yields  $\varsigma(2\Delta x/\lambda) = 0$  because  $G(2\Delta x/\lambda, \theta) = \overline{G(2\Delta x/\lambda)}$  for all  $\theta$ . Similarly, large values of  $\varsigma$  correlate to a high degree of anisotropy so that a direct comparison between methods can be made at a given wavelength, and between wavelengths for a given method. For the scheme represented by Figure 4.1,  $\varsigma = 0.0, 1.2 \times 10^{-2}$ ,

$5.0 \times 10^{-2}$ ,  $1.3 \times 10^{-1}$ ,  $2.9 \times 10^{-1}$  and  $7.0 \times 10^{-1}$  for  $2\Delta x/\lambda = 0, 0.2, 0.4, 0.6, 0.8$  and  $1.0$ , respectively. As indicated by  $\varsigma(0)$  and suggested by the figure, the scheme is perfectly isotropic in the limit of infinite wavelength (i.e.,  $2\Delta x/\lambda = 0$ ). As wavelength decreases, the method becomes increasingly anisotropic. At the Nyquist limit, the method demonstrates the greatest anisotropy in this measure.

The average value of the coefficient of variation,

$$\bar{\varsigma} = \int_0^1 \varsigma(2\Delta x/\lambda) d(2\Delta x/\lambda) \quad (4.4)$$

is also employed here and provides a single number, independent of  $2\Delta x/\lambda$ , which may also be used for comparison of discretization schemes. Again, a larger value of  $\bar{\varsigma}$  indicates (on average) greater anisotropy while  $\bar{\varsigma} = 0$  is representative of a method that is isotropic for all wavelengths.

While the  $\varsigma$  and  $\bar{\varsigma}$  metrics provide a quantitative measure of a method's anisotropy in phase, and discrete and artificial diffusivity, they do not provide a measure of the error associated with a discretization. Indeed, it is possible for a discretization scheme to have significant error in phase or diffusivity, while still demonstrating isotropic behavior. In the case of phase speed, this (unlikely) result is characterized by a perfectly isotropic phase which differs from the ideal such that  $\tilde{c}(2\Delta x/\lambda) = \tilde{c}(2\Delta x/\lambda, \theta) \neq c$ . For this reason, we introduce a second metric, the RMS error metric,

$$\varepsilon(2\Delta x/\lambda) = \sqrt{\frac{1}{2\pi} \int_0^{2\pi} (G(2\Delta x/\lambda, \theta) - g(2\Delta x/\lambda, \theta))^2 d\theta}. \quad (4.5)$$

This metric measures the azimuthal deviation of  $G$  from its true (i.e. physical) value  $g$ . In terms of dimensionless phase speed and discrete diffusivity,  $g = 1$ . Hence, an ideal scheme will have  $\varepsilon(2\Delta x/\lambda) = 0$  for all wavelengths  $0 \leq 2\Delta x/\lambda < 1$ . For the scheme represented by Figure 4.1,  $\varepsilon = 0.0, 5.0 \times 10^{-2}, 1.9 \times 10^{-1}, 3.9 \times 10^{-1}, 6.2 \times 10^{-1}$  and  $8.3 \times 10^{-1}$  for  $2\Delta x/\lambda = 0, 0.2, 0.4, 0.6, 0.8$  and  $1.0$  respectively.

The average value of  $\varepsilon$  over  $2\Delta x/\lambda$ ,

$$\bar{\varepsilon} = \int_0^1 \varepsilon(2\Delta x/\lambda) d(2\Delta x/\lambda) \quad (4.6)$$

is also employed here as it provides a single error metric that facilitates methods comparison. Larger values of  $\bar{\varepsilon}$  indicate larger errors for the method. The method of Figure 4.1 yields  $\bar{\varepsilon} = 3.3 \times 10^{-2}$  in terms of phase speed.

## 4.2 Phase Speed

This section begins with a presentation of the analytic expressions for the non-dimensional phase speed for all the semi-discrete methods considered. A summary of the phase speed results in terms of polar plots and the anisotropy and error metrics follows. These results demonstrate the aspect ratio, wavelength and propagation angle dependence of the individual methods and provide a means of comparison between methods.

### 4.2.1 2D Phase Speed Formulae

Owing to the linear nature of the advection-diffusion equation, the trial solution and the Cartesian grid, the two-dimensional dispersion formulae for some, but not all, of the methods can be written (and, more importantly, understood) in terms of the one-dimensional formulae presented in the previous section. This presentation of the dimensionless phase speed provides a simple generalization with respect to the corresponding one-dimensional versions of the phase-speed for each of the semi-discrete methods. The methods that can be put into this form include FEM, CVFEM, CD, SOU, TOU, Fromm, and QUICK. The phase speed for these methods can be written in the following form,

$$\frac{\tilde{c}}{c} = \cos^2 \theta F_{\tilde{c}}^{1D}(k\Delta x \cos \theta) + \sin^2 \theta F_{\tilde{c}}^{1D}(\gamma k\Delta x \sin \theta), \quad (4.7)$$

where  $F_{\tilde{c}}^{1D}(\vartheta)$  denotes the dimensionless phase speed formula for the corresponding one-dimensional case. The one-dimensional formulae are presented in Table 3.2, in which  $\vartheta$  denotes the dimensionless wavenumber argument in the function,  $k\Delta x$ . As an example, for FEM

$$F_{\tilde{c}}^{1D}(\vartheta) = \frac{\sin(\vartheta)}{\vartheta} \frac{3}{2 + \cos(\vartheta)},$$

and hence the phase speed formula is (c.f. [11], Eq. (2.6-200))

$$\begin{aligned} \frac{\tilde{c}}{c} &= \cos^2 \theta \frac{\sin(k\Delta x \cos \theta)}{k\Delta x \cos \theta} \frac{3}{2 + \cos(k\Delta x \cos \theta)} \\ &+ \sin^2 \theta \frac{\sin(\gamma k\Delta x \sin \theta)}{\gamma k\Delta x \sin \theta} \frac{3}{2 + \cos(\gamma k\Delta x \sin \theta)}. \end{aligned} \quad (4.8)$$

As expected, the one-dimensional formula is recovered along the coordinate directions (i.e.  $\theta = 0, \pi/2, \pi$ , and  $3\pi/2$ ), in terms of the corresponding mesh increment ( $\Delta x$  or  $\Delta y$ ) for the coordinate direction. Furthermore, for modes (and flow orientation) directed along the diagonal ( $\theta = \pi/4$ ) of



a square grid ( $\gamma = 1$ ), the two-dimensional formula also reverts to the one-dimensional result, but on with an effective grid spacing of  $\Delta x_{eff} = \Delta x \sqrt{2}/2$ ,

$$\frac{\tilde{c}}{c} = \frac{\sin(k\Delta x_{eff})}{k\Delta x_{eff}} \frac{3}{2 + \cos(k\Delta x_{eff})}. \quad (4.9)$$

In general, the one-dimensional behavior can be expected in the phase speed whenever  $\tan \theta = 1/\gamma$ . This occurs when the wave is propagating in a direction normal to the diagonals of the grid. In this case  $\Delta x \cos \theta = \Delta y \sin \theta$  and hence Eq. (4.7) reduces to

$$\frac{\tilde{c}}{c} = F_{\tilde{c}}^{1D}(k\Delta x \cos \theta). \quad (4.10)$$

This is the one-dimensional phase speed on a grid with an effective spacing of  $\Delta x \cos \theta$  (or equivalently, an effective wavenumber).

In the results to be presented in the following discussion, the effect of this “enhanced” resolution along the directions normal to the grid diagonals will be realized by a reduced phase error compared to those along the coordinate directions. As we shall see, other two dimensional dispersion quantities share this one-dimensional result along these preferential grid orientations.

**Remark.** When considering grids with aspect ratios other than unity, the appropriate Nyquist frequency of the mesh must be based on the larger of  $\Delta x$  or  $\Delta y$ , i.e., the coarsest mesh spacing. Hence, in the foregoing two-dimensional formulae, and in subsequent dispersion formulae, only  $\gamma \leq 1$  are valid. These formulae may be used for  $\gamma > 1$ , but one must first exchange  $x$  and  $y$  and then use our results for the inverse aspect ratio.

As suggested above, several of the methods considered **cannot** be written in the form of Eq. (4.7). These include the central difference (CD) with consistent mass (CD- $\mathbf{M}_c$ ), the LSR schemes, SUPG, and SUCV. As we shall show, the component functions are analogous to their one-dimensional counterparts, though not the same. The component functions are composed of products of  $x$ - and  $y$ -components of the dimensionless wavenumber.

The CD- $\mathbf{M}_c$  method is an *ad hoc* method. It can be motivated by assuming linear variation of the unknown over the control volumes when developing the time term, but uses standard CD for the advection operator. Its phase speed is given by

$$\frac{\tilde{c}}{c} = \frac{16}{(3 + \cos \theta_x)(3 + \cos \theta_y)} \left( \cos^2 \theta \frac{\sin \theta_x}{\theta_x} + \sin^2 \theta \frac{\sin \theta_y}{\theta_y} \right) \quad (4.11)$$

where we have introduced the notation

$$\theta_x = k\Delta x \cos \theta, \text{ and, } \theta_y = k\Delta y \sin \theta = \gamma k\Delta x \sin \theta. \quad (4.12)$$

This formula does not have the general form of Eq. (4.7). That is, it does not revert to the one-dimensional formula when the wave propagation direction is at right angles to the mesh diagonals. For the one-dimensional case (e.g.  $\theta = 0$ ) the phase speed for CVFEM is recovered, as it should, since the two methods are identical for this case. If the mass matrix is lumped, then the leading factor on the right hand side of the two-dimensional formula is unity, and the formula reverts to the phase speed for the CD method,

$$\frac{\tilde{c}}{c} = \left( \cos^2 \theta \frac{\sin \theta_x}{\theta_x} + \sin^2 \theta \frac{\sin \theta_y}{\theta_y} \right) \quad (4.13)$$

which of course follows the simple form of Eq. (4.7).

The phase speed for LSR(0) is given by,

$$\begin{aligned} \frac{\tilde{c}}{c} = & \cos^2 \theta \frac{1}{12\theta_x} [2 \sin \theta_x (7 + 2 \cos \theta_y) - \sin 2\theta_x (1 + 2 \cos \theta_y)] \\ & + \sin^2 \theta \frac{1}{12\theta_y} [2 \sin \theta_y (7 + 2 \cos \theta_x) - \sin 2\theta_y (1 + 2 \cos \theta_x)] \end{aligned} \quad (4.14)$$

This scheme also does not follow the general form of Eq. (4.7), as it contains cross terms from the  $x$ - and  $y$ -component functions. These cross-terms arise because the advection stencils (see Appendix A) include terms from all neighboring grid points. This is also true for the FEM and CVFEM operators, however the symbols factor conveniently to eliminate the cross terms. In contrast, the FDM/FVM methods (FOU, SOU, TOU, Fromm and QUICK), have component operators which include only terms along the coordinate directions. Incidentally, the corresponding one-dimensional phase speed for LSR(0) is obtained along the coordinate directions. For example, the  $x$ -direction ( $\theta = 0$ ) formula is

$$\frac{\tilde{c}}{c} = \frac{1}{4\theta_x} (6 \sin \theta_x - \sin 2\theta_x). \quad (4.15)$$

This is the one-dimensional version of Fromm's method.

The phase speed for LSR(-1) is:

$$\begin{aligned} \frac{\tilde{c}}{c} = & \cos^2 \theta \frac{1}{6\theta_x} [4(2 + \cos \theta_y) \sin \theta_x - (1 + 2 \cos \theta_y) \sin 2\theta_x] \\ & + \sin^2 \theta \frac{1}{6\theta_y} [4(2 + \cos \theta_x) \sin \theta_y - (1 + 2 \cos \theta_x) \sin 2\theta_y] \end{aligned} \quad (4.16)$$

which also contains mixed terms in the component functions. Along the coordinate directions (i.e. in one dimension) the phase speed is,

$$\frac{\tilde{c}}{c} = \frac{1}{2\theta_x}(4\sin\theta_x - \sin 2\theta_x), \quad (4.17)$$

which, incidentally, is the one-dimensional formula for SOU.

The phase speed formulae for SUPG and SUCV are given by,

$$\begin{aligned} \frac{\tilde{c}}{c} = & \frac{(\cos^2\theta \mathcal{G}(\theta_x) + \sin^2\theta \mathcal{G}(\theta_y))}{\left[1 + \beta^2(\theta_x + \theta_y)^2 (\cos^2\theta \mathcal{G}(\theta_x) + \sin^2\theta \mathcal{G}(\theta_y))^2\right]} \times \\ & \left[1 + \frac{\beta_\theta}{2} \left( \left( \frac{1}{Pe_x} + 2\beta_\theta \cos^2\theta \right) \mathcal{F}(\theta_x) + \frac{4\cos\theta \sin\theta}{\gamma} \beta_\theta \mathcal{G}(\theta_x) \mathcal{G}(\theta_y) \right. \right. \\ & \left. \left. + \left( \frac{1}{Pe_y} + 2\beta_\theta \sin^2\theta \right) \mathcal{F}(\theta_y) \right) \right] \end{aligned} \quad (4.18)$$

where

$$\begin{aligned} \mathcal{F}(\vartheta) &= \frac{2(1 - \cos\vartheta)}{\mathcal{M}(\vartheta)} \\ \mathcal{G}(\vartheta) &= \frac{\sin\vartheta}{\vartheta} \frac{1}{\mathcal{M}(\vartheta)} \\ \beta_\theta &= \beta(\cos\theta + \gamma \sin\theta) \\ Pe_x &= \frac{c\Delta x}{2\alpha}, \quad Pe_y = \frac{c\Delta y}{2\alpha} \end{aligned} \quad (4.19)$$

and  $\mathcal{M}(\vartheta)$  is the symbol for the mass matrix operator, given in Table 3.1. In this formula, the stabilization parameter  $\tau$  in Eq. (A.29) is written as

$$\tau = \frac{\beta_\theta \Delta x}{c}. \quad (4.20)$$

While not of the form in Eq. (4.7), the component terms in this formula are similar to the respective one-dimensional terms in Table 3.2 and the two-dimensional formula reverts to the one-dimensional formula along the coordinate directions and also reverts to the FEM or CVFEM expressions for  $\beta = 0$ .

### 4.2.2 2D Phase Speed Results

The phase speed results for our two-dimensional semi-discretizations are presented in Figures 4.2 to 4.15. Figures (a) and (b) for each semi-discretization present  $\tilde{c}/c$  for grid aspect ratios of  $\gamma = 1$  and  $\gamma = 1/2$  respectively. As

in the example polar plot (Figure 4.1) phase speed curves are plotted for  $2\Delta x/\lambda = 0, 0.2, 0.4, 0.6, 0.8$  and  $1.0$ . In the absence of phase errors, the ideal semi-discrete phase speed would exactly replicate the continuous phase speed for the entire discrete spectrum from the limit  $\Delta x \rightarrow 0$  to the grid Nyquist limit. Hence, in the ideal case, the phase speed curves would be circular, each giving  $\tilde{c}/c = 1$ . However, all of the methods considered here introduce either leading or lagging phase speeds, the magnitudes of which are dependent on wavelength, grid aspect ratio and propagation direction.

Several points regarding the semi-discretizations are noted before beginning the discussion of results. First, phase speed for the FEM-SUPG (Figures 4.3 and 4.4) and CVFEM-SUCV (Figures 4.6 and 4.7) are presented for pure advection, i.e., when  $\mathbf{P}_e \rightarrow \infty$ . Second, results for the lumped mass variants of FEM and CVFEM are not included here as their results are significantly degraded relative to their consistent mass counterparts (see §3.1 for examples of the effects of mass lumping). Finally, the reader is reminded that the FOU scheme may be decomposed into a centered second-order advection scheme with concomitant second-order artificial viscosity. For this reason, phase speed results for the FOU and “Centered FDM” scheme are identical and so presented as one result.

Several characteristics are evident from the series of figures presented here. First, the figures clearly indicate anisotropic wave propagation for all schemes considered with the  $\gamma = 1/2$  cases demonstrating less  $\theta$ -dependence than their  $\gamma = 1$  counterparts. Indeed, the  $\gamma = 1$  cases all show quarter-symmetry while the  $\gamma = 1/2$  discretizations show half-symmetry, both behaviors being consistent with the symmetry of their respective spatial grids. It is also evident from the figures that this anisotropy generally increases with increasing  $2\Delta x/\lambda$ . This observation is demonstrated quantitatively in Tables 4.1 and 4.2 where the coefficient of variation of the phase speed,  $\varsigma_{\tilde{c}}$ , and its mean  $\overline{\varsigma}_{\tilde{c}}$  are presented. The tables show that  $\varsigma_{\tilde{c}}$  generally grows with increasing  $2\Delta x/\lambda$ . In terms of the  $\overline{\varsigma}_{\tilde{c}}$  metric, and relative to the grid aspect ratio,  $\gamma = 1/2$  minimizes  $\theta$ -dependence for all but the LSR semi-discretizations. Finally, it is evident from a method-to-method comparison of  $\overline{\varsigma}_{\tilde{c}}$  that FEM-SUPG and CVFEM-SUCV minimize anisotropic behavior irrespective of grid aspect ratio given the proper choice of stabilization parameter. Note that the LSR schemes provide good isotropy for the  $\gamma = 1$  case but become significantly more anisotropic (relative to the other methods) for  $\gamma = 1/2$ .

The series of figures in this section also provides information concerning the phase error of each method. As suggested by the anisotropy discussion above, this error is dependent on wavenumber as well as propagation angle. Indeed the methods generally demonstrate a minimum error along the  $\theta = \pi/4$  and  $\pi/2$  directions for the unit and  $1/2$  aspect ratio cases respectively. These ‘preferential’ directions are a result of the better resolving power of the

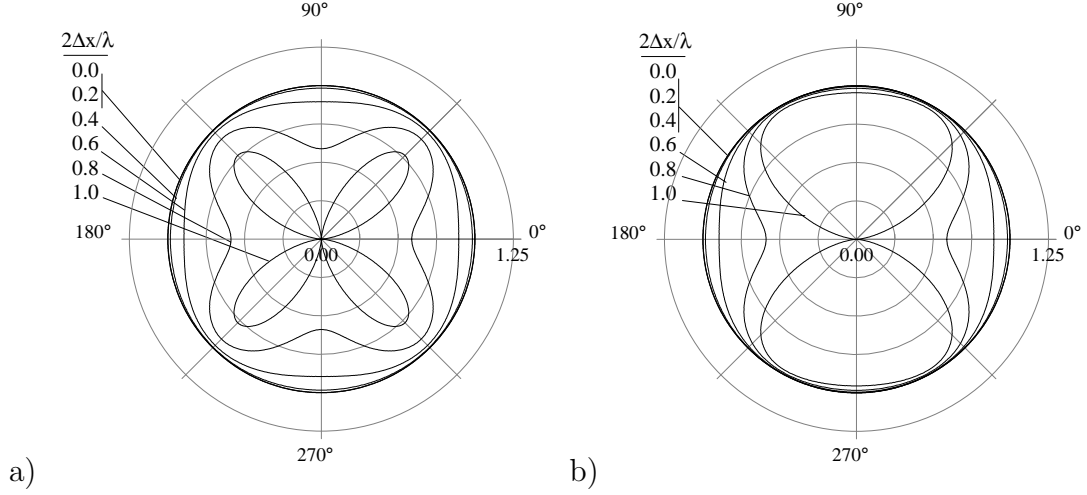


Figure 4.2: Non-dimensional phase speed ( $\tilde{c}/c$ ; radial) as a function of  $\theta$  (azimuthal) for the consistent mass Galerkin finite element method (FEM -  $\mathbf{M}_c$ ) with a)  $\gamma = 1$  and b)  $\gamma = 1/2$ .

grid in these directions (cf. §4.2.1). A quantitative measure of the discrete phase errors is presented in Tables 4.3 and 4.4. As with  $\varsigma_{\tilde{c}}$ , the phase errors,  $\varepsilon_{\tilde{c}}$ , generally increase with increasing  $2\Delta x/\lambda$ , peaking at the Nyquist limit. In terms of the  $\overline{\varepsilon}_{\tilde{c}}$  metric, the  $\gamma = 1/2$  results minimize phase errors relative to the unit aspect ratio cases for all but the LSR cases. Finally, it is evident from a comparison of  $\overline{\varepsilon}_{\tilde{c}}$  between methods, that FEM-SUPG and CVFEM-SUCV minimize errors, for either  $\gamma$ , given the proper choice of stabilization parameter ( $\beta = \beta_{opt}$  and  $1/2$  for SUPG and SUCV respectively). Note that FOU demonstrates by far the worst phase error (in terms of  $\overline{\varepsilon}_{\tilde{c}}$ ) relative to the other semi-discretizations, regardless of aspect ratio.

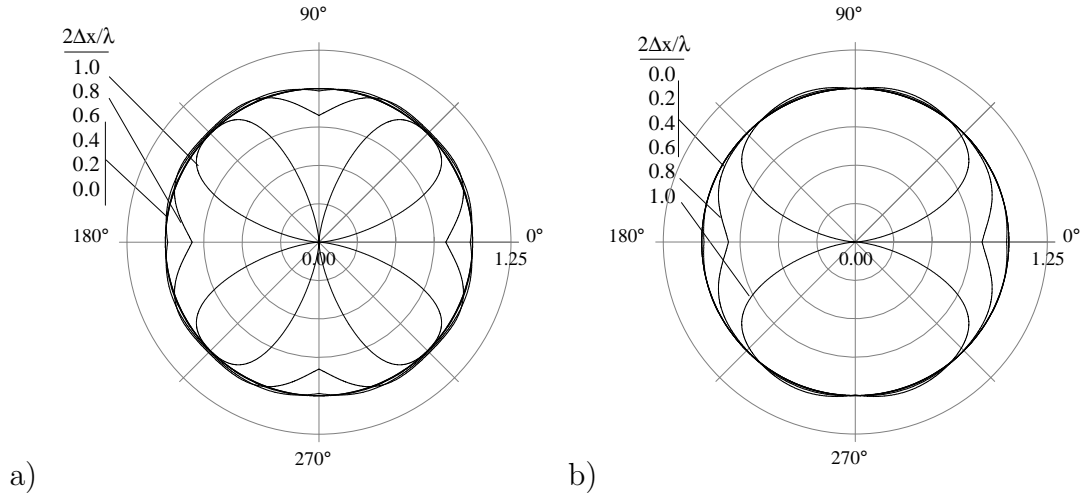


Figure 4.3: Non-dimensional phase speed ( $\tilde{c}/c$ ; radial) as a function of  $\theta$  (azimuthal) for consistent mass matrix finite element method SUPG with  $\beta_{opt}$ ; a)  $\gamma = 1$  and b)  $\gamma = 1/2$ .

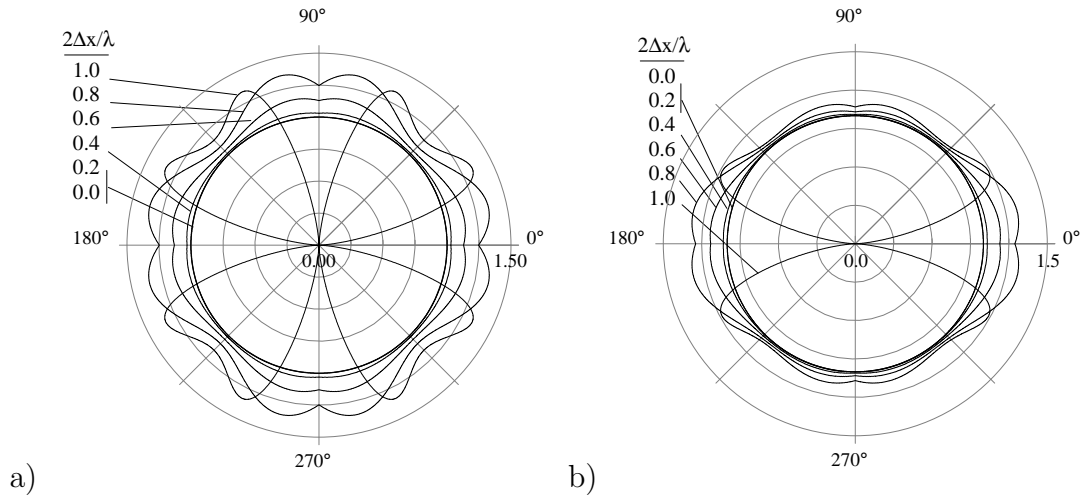


Figure 4.4: Non-dimensional phase speed ( $\tilde{c}/c$ ; radial) as a function of  $\theta$  (azimuthal) for consistent mass matrix finite element method SUPG with  $\beta = 1/2$ ; a)  $\gamma = 1$  and b)  $\gamma = 1/2$ .

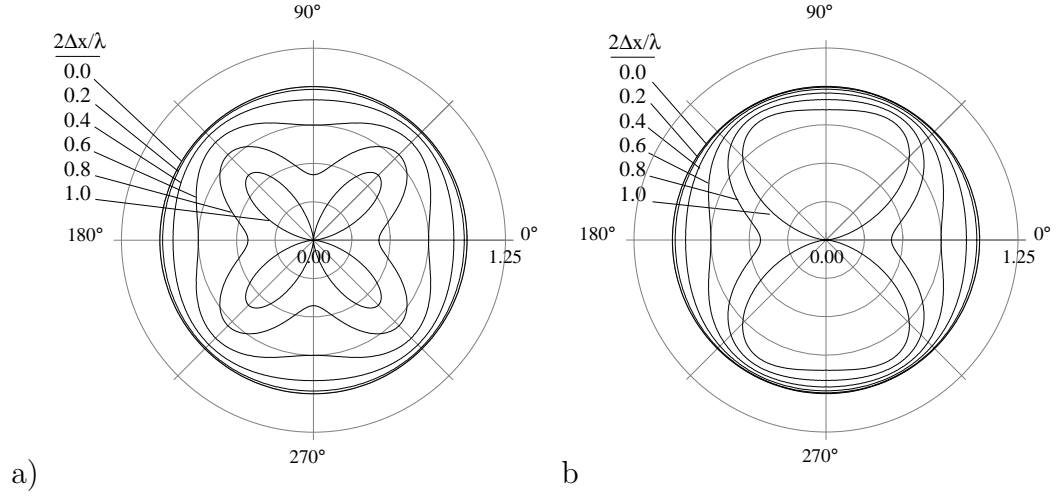


Figure 4.5: Non-dimensional phase speed ( $\tilde{c}/c$ ; radial) as a function of  $\theta$  (azimuthal) for the consistent mass control volume finite element method (CVFEM) with a)  $\gamma = 1$  and b)  $\gamma = 1/2$ .

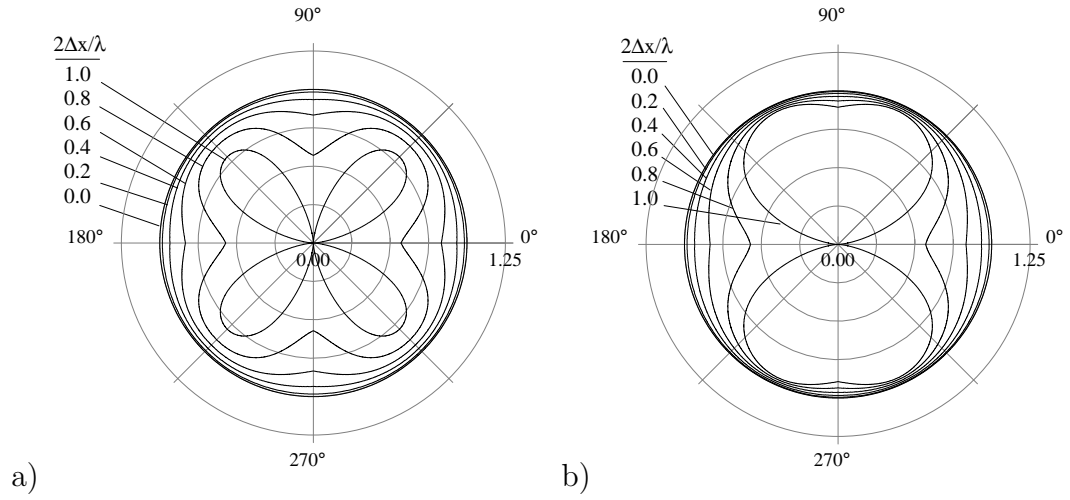


Figure 4.6: Non-dimensional phase speed ( $\tilde{c}/c$ ; radial) as a function of  $\theta$  (azimuthal) for consistent mass matrix control volume finite element method SUCV with  $\beta_{opt}$ ; a)  $\gamma = 1$  and b)  $\gamma = 1/2$ .

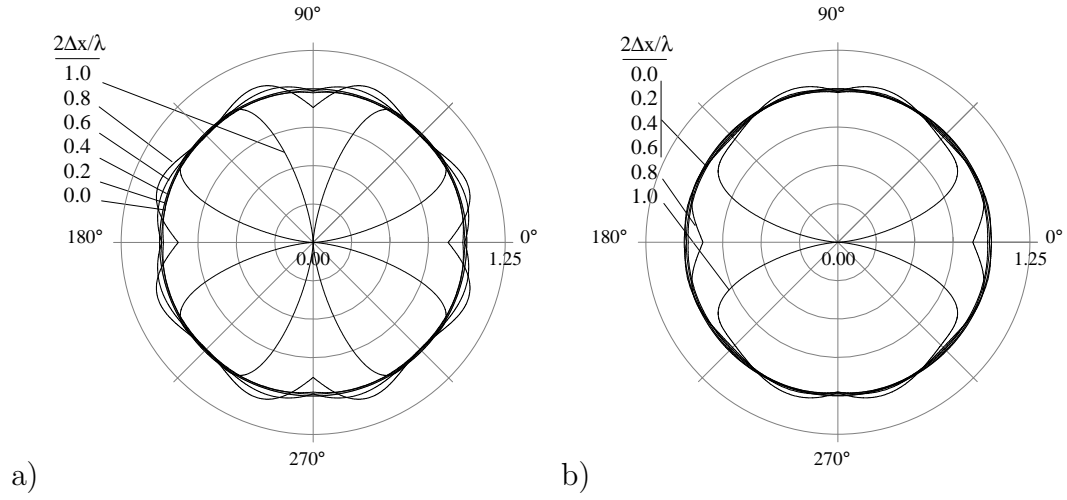


Figure 4.7: Non-dimensional phase speed ( $\tilde{c}/c$ ; radial) as a function of  $\theta$  (azimuthal) for consistent mass matrix control volume finite element method SUCV with  $\beta = 1/2$ ; a)  $\gamma = 1$  and b)  $\gamma = 1/2$ .

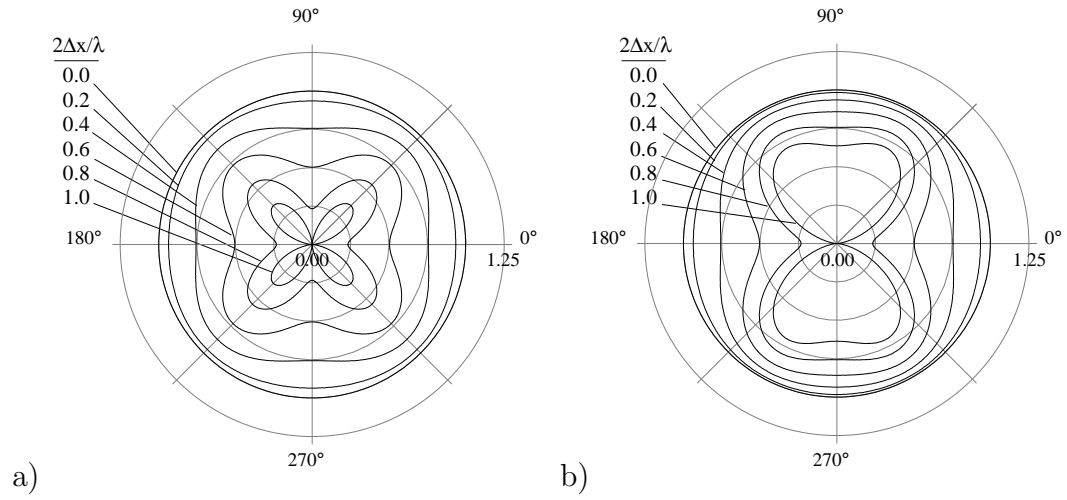


Figure 4.8: Non-dimensional phase speed ( $\tilde{c}/c$ ; radial) as a function of  $\theta$  (azimuthal) for the central difference method (also FOU). Results for aspect ratios of a)  $\gamma = 1$  and b)  $\gamma = 1/2$  are shown.



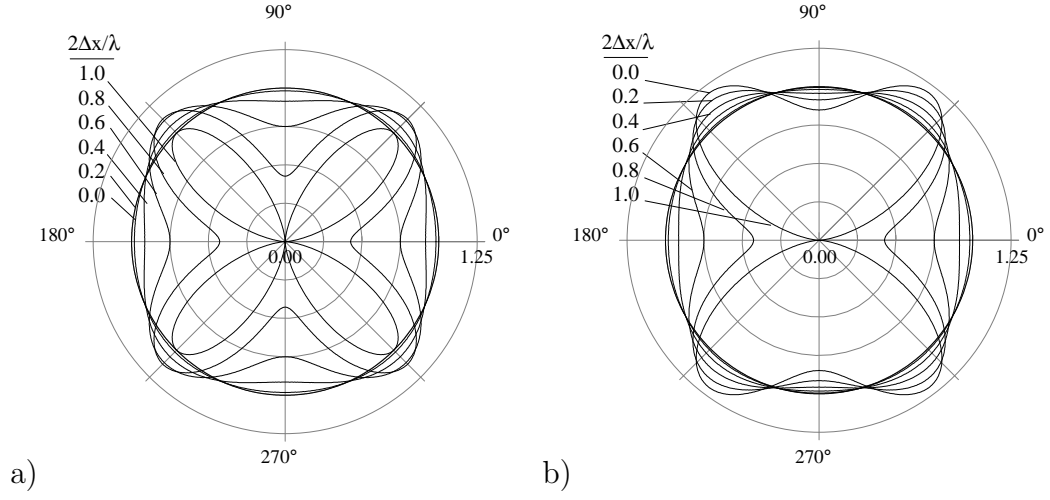


Figure 4.9: Non-dimensional phase speed ( $\tilde{c}/c$ ; radial) as a function of  $\theta$  (azimuthal) for the consistent mass matrix central difference discretization (CD- $\mathbf{M}_c$ ). Results for aspect ratios of a)  $\gamma = 1$  and b)  $\gamma = 1/2$  are shown.

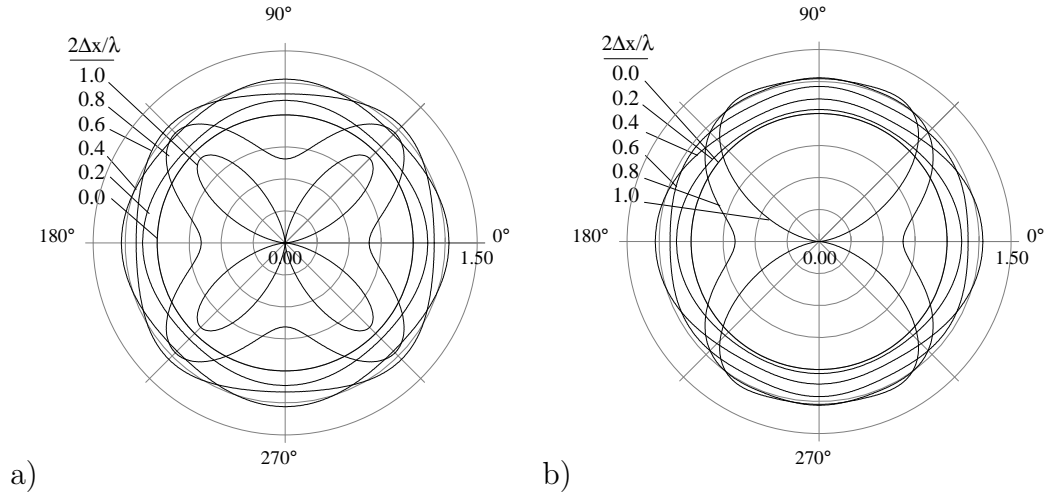


Figure 4.10: Non-dimensional phase speed ( $\tilde{c}/c$ ; radial) as a function of  $\theta$  (azimuthal) for the second-order upwind finite difference discretization (SOU). Results are shown for aspect ratios of a)  $\gamma = 1$  and b)  $\gamma = 1/2$ .

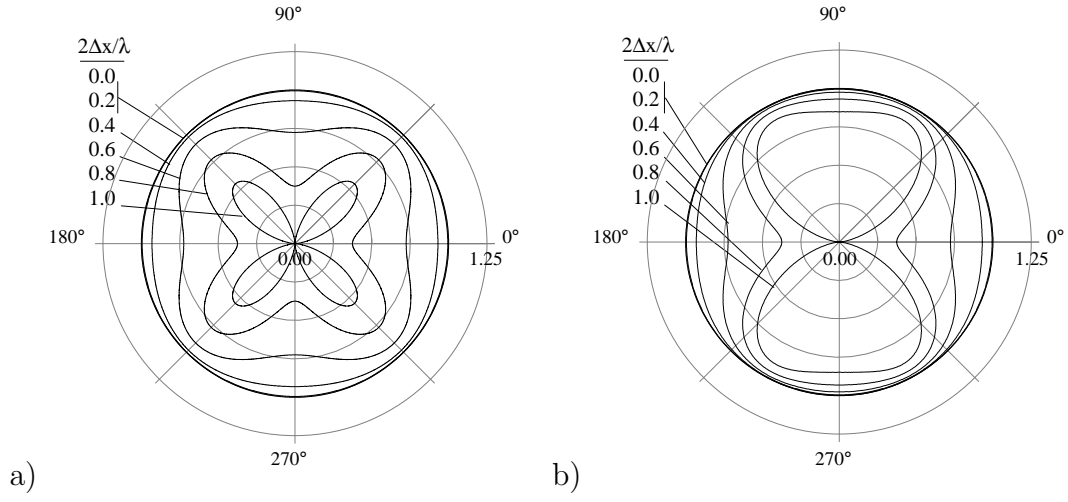


Figure 4.11: Non-dimensional phase speed ( $\tilde{c}/c$ ; radial) as a function of  $\theta$  (azimuthal) for the finite difference discretization with third-order-upwind differencing. Results for aspect ratios of a)  $\gamma = 1$  and b)  $\gamma = 1/2$  are shown.

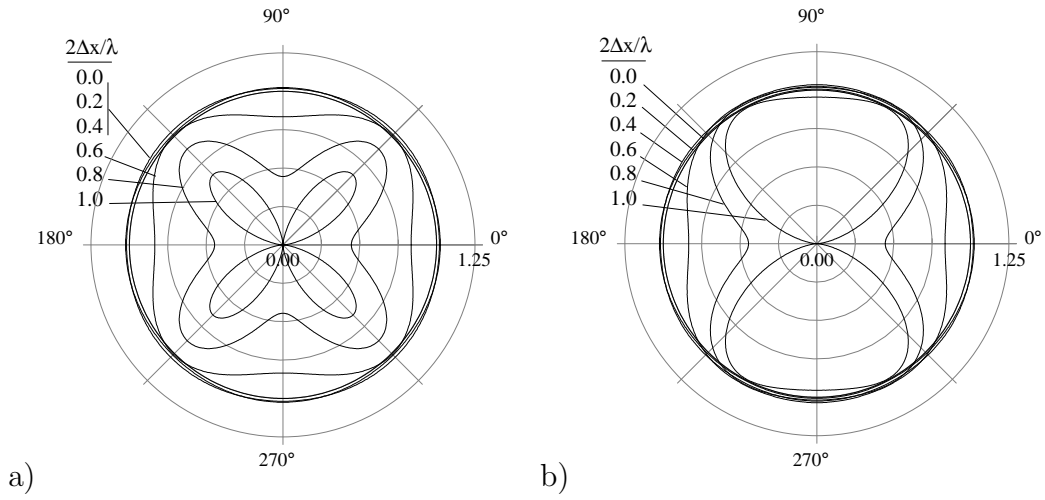


Figure 4.12: Non-dimensional phase speed ( $\tilde{c}/c$ ; radial) as a function of  $\theta$  (azimuthal) for Fromm's method. Results for a)  $\gamma = 1$  and b)  $\gamma = 1/2$  are shown.

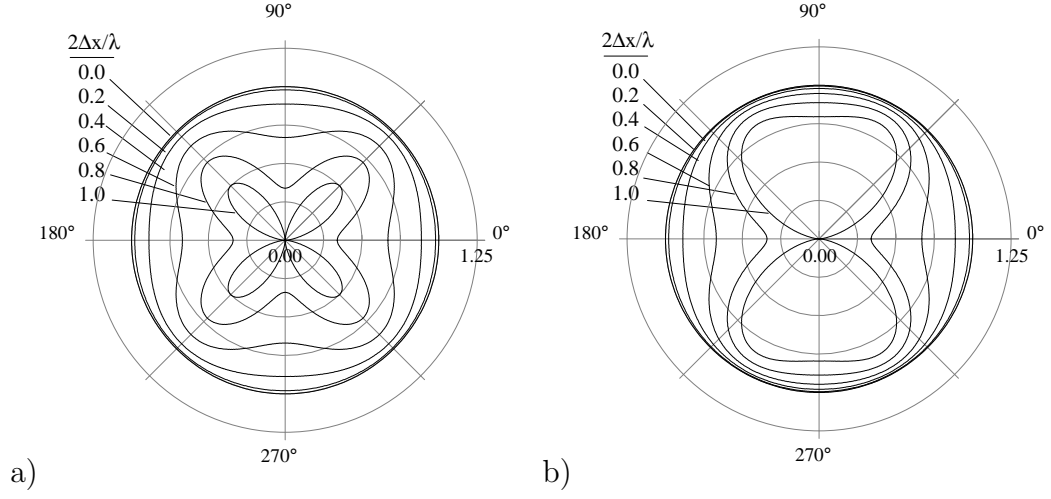


Figure 4.13: Non-dimensional phase speed ( $\tilde{c}/c$ ; radial) as a function of  $\theta$  (azimuthal) for the QUICK scheme with a)  $\gamma = 1$  and b)  $\gamma = 1/2$ .

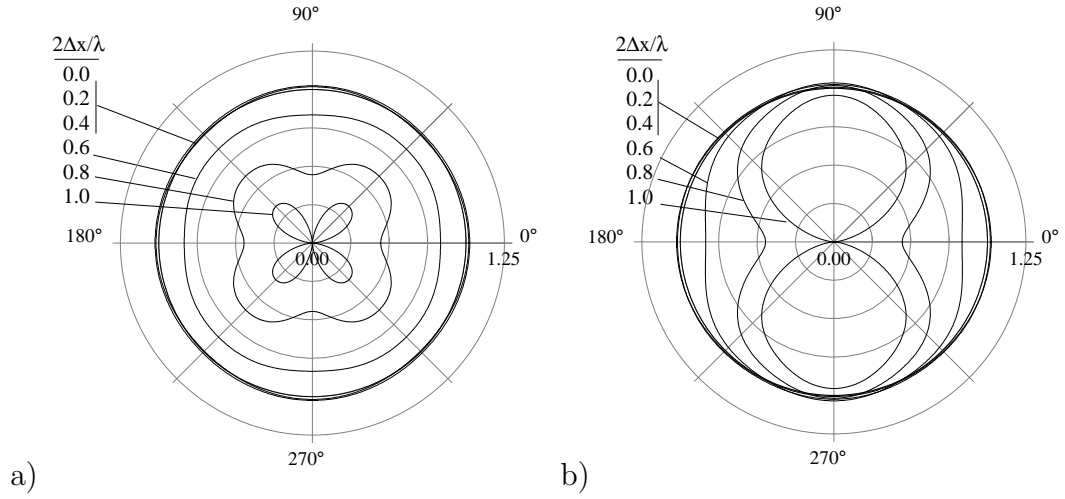


Figure 4.14: Non-dimensional phase speed ( $\tilde{c}/c$ ; radial) as a function of  $\theta$  (azimuthal) for the node-centered finite volume method with least squares gradient reconstruction ( $\theta = 1.$ ,  $\kappa = 0$ ) with a)  $\gamma = 1$  and b)  $\gamma = 1/2$ .

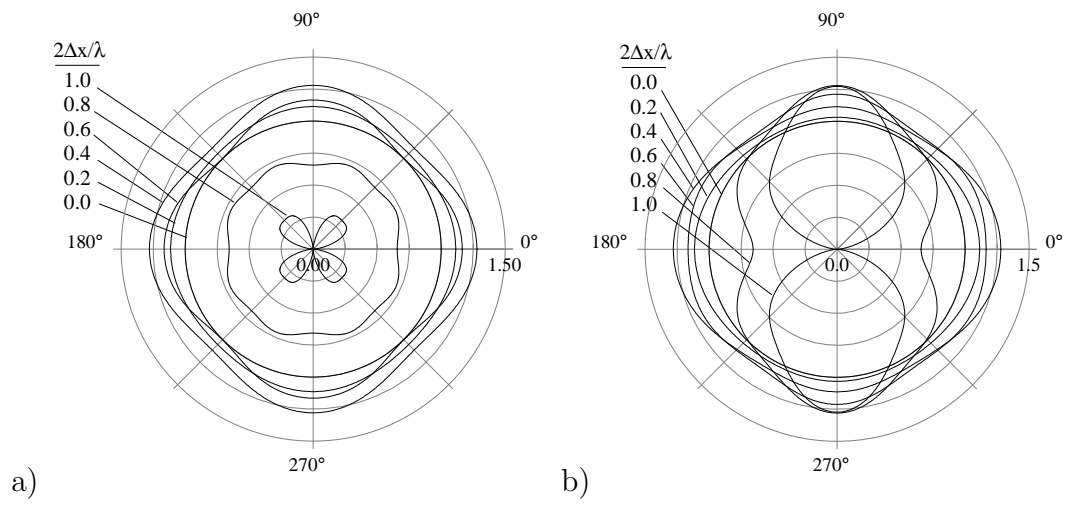


Figure 4.15: Non-dimensional phase speed ( $\tilde{c}/c$ ; radial) as a function of  $\theta$  (azimuthal) for the node-centered finite volume method with least squares gradient reconstruction ( $\theta = 1.$ ,  $\kappa = -1$ ) with a)  $\gamma = 1$  and b)  $\gamma = 1/2$ .

Method	$\varsigma_{\bar{c}}$ as a function of $2\Delta x/\lambda$						$\overline{\varsigma_{\bar{c}}}$
	0.0	0.2	0.4	0.6	0.8	1.0	
FEM- $\mathbf{M}_c$	0.0	2.43e-4	4.60e-3	3.14e-2	1.55e-1	7.45e-1	1.13e-1
SUPG $\beta_{opt}$	0.0	9.36e-5	1.48e-3	8.64e-3	6.44e-2	6.43e-1	7.92e-2
SUPG $\beta = 1/2$	0.0	6.13e-4	8.79e-3	3.68e-2	7.56e-2	5.32e-1	7.75e-2
CVFEM- $\mathbf{M}_c$	0.0	3.26e-3	1.79e-2	6.48e-2	2.11e-1	7.40e-1	1.33e-1
SUCV $\beta_{opt}$	0.0	2.95e-3	1.27e-2	3.82e-2	1.41e-1	6.80e-1	1.07e-1
SUCV $\beta = 1/2$	0.0	2.17e-3	4.37e-3	1.77e-2	4.92e-2	5.81e-1	7.28e-2
FDM FOU	0.0	1.19e-2	5.06e-2	1.29e-1	2.85e-1	7.00e-1	1.65e-1
FDM- $\mathbf{M}_c$	0.0	1.19e-2	5.21e-2	1.38e-1	3.22e-1	7.60e-1	1.81e-1
SOU	0.0	1.72e-2	2.39e-2	3.53e-2	2.15e-1	7.72e-1	1.36e-1
TOU	0.0	1.31e-3	1.85e-2	8.22e-2	2.47e-1	7.38e-1	1.44e-1
Fromm's	0.0	3.62e-3	5.71e-3	6.66e-2	2.36e-1	7.50e-1	1.37e-1
QUICK	0.0	3.86e-3	2.56e-2	9.16e-2	2.55e-1	7.31e-1	1.48e-1
LSR(0)	0.0	4.68e-3	8.14e-3	1.31e-2	1.12e-1	6.36e-1	9.13e-2
LSR(-1)	0.0	1.92e-2	4.81e-2	5.29e-2	2.46e-2	5.86e-1	8.75e-2

Table 4.1: Coefficient of Variation of phase speed,  $\varsigma_{\bar{c}}$ , as a function of  $2\Delta x/\lambda$ , and its average,  $\overline{\varsigma_{\bar{c}}}$ , for the two-dimensional,  $\gamma = 1$  semi-discretizations.

Method	$\varsigma_{\bar{c}}$ as a function of $2\Delta x/\lambda$						$\overline{\varsigma_{\bar{c}}}$
	0.0	0.2	0.4	0.6	0.8	1.0	
FEM- $\mathbf{M}_c$	0.0	3.11e-4	5.75e-3	3.72e-2	1.63e-1	5.30e-1	9.42e-2
SUPG $\beta_{opt}$	0.0	3.65e-5	4.90e-4	3.81e-3	5.37e-2	4.44e-1	5.61e-2
SUPG $\beta = 1/2$	0.0	8.44e-4	1.12e-2	4.43e-2	8.85e-2	3.55e-1	6.45e-2
CVFEM- $\mathbf{M}_c$	0.0	5.17e-3	2.65e-2	8.64e-2	2.37e-1	5.51e-1	1.26e-1
SUCV $\beta_{opt}$	0.0	4.68e-3	1.89e-2	5.03e-2	1.51e-1	4.91e-1	9.40e-2
SUCV $\beta = 1/2$	0.0	3.50e-3	4.67e-3	8.47e-3	2.83e-2	4.04e-1	4.94e-2
FDM FOU	0.0	1.91e-2	7.79e-2	1.82e-1	3.39e-1	5.62e-1	1.80e-1
FDM- $\mathbf{M}_c$	0.0	8.82e-3	3.99e-2	1.11e-1	2.60e-1	5.22e-1	1.36e-1
SOU	0.0	3.02e-2	5.80e-2	1.23e-2	2.07e-1	5.71e-1	1.18e-1
TOU	0.0	1.70e-3	2.41e-2	1.04e-1	2.76e-1	5.65e-1	1.38e-1
Fromm's	0.0	6.62e-3	2.17e-3	7.38e-2	2.54e-1	5.67e-1	1.24e-1
QUICK	0.0	5.94e-3	3.65e-2	1.21e-1	2.90e-1	5.65e-1	1.47e-1
LSR(0)	0.0	6.73e-3	3.49e-3	6.80e-2	2.44e-1	5.75e-1	1.22e-1
LSR(-1)	0.0	3.04e-2	6.17e-2	2.71e-2	1.92e-1	5.95e-1	1.22e-1

Table 4.2: Coefficient of Variation of phase speed,  $\varsigma_{\bar{c}}$ , as a function of  $2\Delta x/\lambda$ , and its average,  $\overline{\varsigma_{\bar{c}}}$ , for the two-dimensional,  $\gamma = 1/2$  semi-discretizations.

Method	$\varepsilon_{\tilde{c}}$ as a function of $2\Delta x/\lambda$						$\overline{\varepsilon_{\tilde{c}}}$
	0.0	0.2	0.4	0.6	0.8	1.0	
FEM- $\mathbf{M}_c$	0.0	6.14e-4	1.12e-2	6.92e-2	2.71e-1	6.90e-1	1.39e-1
SUPG $\beta_{opt}$	0.0	2.81e-4	3.97e-3	1.46e-2	6.78e-2	5.61e-1	7.34e-2
SUPG $\beta = 1/2$	0.0	2.32e-3	2.91e-2	1.14e-1	2.62e-1	4.87e-1	1.30e-1
CVFEM- $\mathbf{M}_c$	0.0	1.35e-2	6.36e-2	1.82e-1	4.15e-1	7.45e-1	2.09e-1
SUCV $\beta_{opt}$	0.0	1.22e-2	4.54e-2	1.04e-1	2.54e-1	6.43e-1	1.47e-1
SUCV $\beta = 1/2$	0.0	9.26e-3	1.28e-2	2.18e-2	5.21e-2	5.14e-1	7.06e-2
FDM FOU	0.0	4.99e-2	1.89e-1	3.91e-1	6.17e-1	8.29e-1	3.32e-1
FDM- $\mathbf{M}_c$	0.0	1.20e-2	5.30e-2	1.46e-1	3.39e-1	6.41e-1	1.74e-1
SOU	0.0	8.97e-2	2.39e-1	2.25e-1	2.14e-1	6.60e-1	2.20e-1
TOU	0.0	3.38e-3	4.75e-2	1.94e-1	4.55e-1	7.61e-1	2.16e-1
Fromm's	0.0	1.99e-2	2.69e-2	1.02e-1	3.78e-1	7.31e-1	1.78e-1
QUICK	0.0	1.50e-2	8.27e-2	2.43e-1	4.94e-1	7.77e-1	2.44e-1
LSR(0)	0.0	1.87e-2	1.08e-2	1.47e-1	4.63e-1	8.19e-1	2.10e-1
LSR(-1)	0.0	8.73e-2	2.07e-1	1.07e-1	3.11e-1	8.10e-1	2.23e-1

Table 4.3: RMS error of discrete phase speed,  $\varepsilon_{\tilde{c}}$ , as a function of  $2\Delta x/\lambda$ , and its average,  $\overline{\varepsilon_{\tilde{c}}}$ , for the two-dimensional,  $\gamma = 1$  semi-discretizations.

Method	$\varepsilon_{\tilde{c}}$ as a function of $2\Delta x/\lambda$						$\overline{\varepsilon_{\tilde{c}}}$
	0.0	0.2	0.4	0.6	0.8	1.0	
FEM- $\mathbf{M}_c$	0.0	4.31e-4	7.86e-3	4.87e-2	1.91e-1	4.85e-1	9.80e-2
SUPG $\beta_{opt}$	0.0	7.35e-5	9.49e-4	3.95e-3	5.87e-2	4.11e-1	5.39e-2
SUPG $\beta = 1/2$	0.0	1.28e-3	1.71e-2	6.94e-2	1.52e-1	3.39e-1	8.19e-2
CVFEM- $\mathbf{M}_c$	0.0	9.58e-3	4.51e-2	1.29e-1	2.92e-1	5.24e-1	1.48e-1
SUCV $\beta_{opt}$	0.0	8.88e-3	3.45e-2	8.23e-2	1.97e-1	4.66e-1	1.11e-1
SUCV $\beta = 1/2$	0.0	7.17e-3	1.42e-2	1.24e-2	3.34e-2	3.80e-1	5.15e-2
FDM FOU	0.0	3.56e-2	1.36e-1	2.81e-1	4.46e-1	6.05e-1	2.40e-1
FDM- $\mathbf{M}_c$	0.0	8.83e-3	4.01e-2	1.12e-1	2.55e-1	4.64e-1	1.30e-1
SOU	0.0	6.43e-2	1.76e-1	1.95e-1	2.35e-1	5.07e-1	1.85e-1
TOU	0.0	2.37e-3	3.33e-2	1.36e-1	3.18e-1	5.32e-1	1.51e-1
Fromm's	0.0	1.44e-2	2.30e-2	7.63e-2	2.67e-1	5.09e-1	1.27e-1
QUICK	0.0	1.06e-2	5.84e-2	1.71e-1	3.48e-1	5.47e-1	1.72e-1
LSR(0)	0.0	1.41e-2	1.79e-2	8.00e-2	2.85e-1	5.42e-1	1.34e-1
LSR(-1)	0.0	6.38e-2	1.68e-1	1.55e-1	1.89e-1	5.16e-1	1.67e-1

Table 4.4: RMS error of discrete phase speed,  $\varepsilon_{\tilde{c}}$ , as a function of  $2\Delta x/\lambda$ , and its average,  $\overline{\varepsilon_{\tilde{c}}}$ , for the two-dimensional,  $\gamma = 1/2$  semi-discretizations.



## 4.3 Discrete Diffusivity

This section begins with a presentation of the analytic expressions for the dimensionless discrete diffusivity for all the semi-discretizations considered. A summary of the discrete diffusivity results in terms of polar plots and the anisotropy and error metrics follows. These results demonstrate the aspect ratio, wavelength and propagation angle dependence of the discrete diffusivity for the individual methods and provide a means of comparison between methods.

### 4.3.1 2D Discrete Diffusivity Formulae

Some, but not all, of the two-dimensional formulae for discrete diffusivity can be written in the same form as for phase error, Eq. (4.7), if we replace  $F_c^{1D}$  with the 1-D formula for dimensionless discrete diffusivity,  $F_{\tilde{\alpha}}^{1D}$ , given in Table 3.6. The result is,

$$\frac{\tilde{\alpha}}{\alpha} = \cos^2 \theta F_{\tilde{\alpha}}^{1D}(k\Delta x \cos \theta) + \sin^2 \theta F_{\tilde{\alpha}}^{1D}(\gamma k\Delta x \sin \theta). \quad (4.21)$$

The methods which have this form include all of the FDMs (FOU (hence CD), SOU, TOU, QUICK, and Fromm) and the LSR schemes, since they all share the same 5-point diffusion stencil. FEM and CVFEM can also be factored into this form. For example, for FEM and CVFEM

$$F_{\tilde{\alpha}}^{1D} = \frac{2(1 - \cos \vartheta)}{\vartheta^2} \frac{1}{\mathcal{M}(\vartheta)},$$

in terms of the mass matrix symbol, and hence the two-dimensional discrete diffusivity formula is

$$\begin{aligned} \frac{\tilde{\alpha}}{\alpha} = & \cos^2 \theta \frac{2(1 - \cos(k\Delta x \cos \theta))}{(k\Delta x \cos \theta)^2} \frac{1}{\mathcal{M}(\theta_x)} \\ & + \sin^2 \theta \frac{2(1 - \cos(\gamma k\Delta x \sin \theta))}{(\gamma k\Delta x \sin \theta)^2} \frac{1}{\mathcal{M}(\theta_y)}. \end{aligned} \quad (4.22)$$

Notice that the discrete diffusivities represented by Eq. (4.21) also exhibit the one-dimensional form when the mode is propagating in a direction normal to the grid diagonals, i.e., when  $\tan \theta = 1/\gamma$ . In this case Eq. (4.21) becomes

$$\frac{\tilde{\alpha}}{\alpha} = F_{\tilde{\alpha}}^{1D}(k\Delta x \cos \theta), \quad (4.23)$$

the 1-D version of discrete diffusivity on an effective mesh spacing of  $k\Delta x \cos \theta$ , the spacing between grid diagonals.

The 2-D discrete diffusivity for SUPG and SUCV is

$$\frac{\tilde{\alpha}}{\alpha} = \frac{\left[ \frac{\cos^2 \theta \mathcal{F}(\theta_x)}{\theta_x^2} + \frac{\sin^2 \theta \mathcal{F}(\theta_y)}{\theta_y^2} \right]}{\left[ 1 + \beta^2 (\theta_x + \theta_y)^2 \left( \cos^2 \theta \mathcal{G}(\theta_x) + \sin^2 \theta \mathcal{G}(\theta_y) \right)^2 \right]} \quad (4.24)$$

in terms of the functions defined in Eq. (4.19). Except for the inclusion of the  $\tau$  factor, this formula has the form Eq. (4.21), with a modified angular-dependent  $\beta$  parameter.

### 4.3.2 2D Discrete Diffusivity Results

The discrete diffusivity results for our two-dimensional semi-discretizations are presented in Figures 4.16 to 4.23. Figures (a) and (b) present  $\tilde{\alpha}/\alpha$  for grid aspect ratios of  $\gamma = 1$  and  $1/2$  respectively. Dimensionless discrete diffusivity curves are plotted for  $2\Delta x/\lambda = 0, 0.2, 0.4, 0.6, 0.8$  and  $1.0$ . In the ideal case, the discrete diffusivity would exactly replicate the continuous diffusivity for the entire discrete spectrum from the limit  $\Delta x \rightarrow 0$  to the grid Nyquist limit. Hence, in the ideal case, the discrete diffusivity curves would be circular, each giving  $\tilde{\alpha}/\alpha = 1$ . However, all of the methods considered here are either over- or under-diffusive, the magnitude of the error in diffusivity being dependent on wavelength, grid aspect ratio and propagation direction.

Several points regarding the semi-discretizations are noted before beginning the discussion of results. First, results for the lumped mass variants of FEM and CVFEM are not included here because their results are significantly degraded relative to their consistent mass counterparts. Second, as the finite difference semi-discretizations use second-order centered approximations for the diffusion operator in conjunction with a lumped mass matrix, they yield identical discrete diffusivities (the exception being FDM- $\mathbf{M}_c$  where the “consistent” mass matrix is used). For this reason, discrete diffusivity results for the lumped mass finite difference schemes considered here are identical and presented as one result labeled FDM.

Several characteristics are evident from the series of figures presented here. First, the figures clearly indicate anisotropic discrete diffusivities for all schemes considered. As with the two-dimensional phase speed results, the  $\gamma = 1$  cases all show quarter-symmetry while the  $\gamma = 1/2$  discretizations show half-symmetry. The figures also suggest that the anisotropy generally increases with increasing  $2\Delta x/\lambda$ . This observation is demonstrated quantitatively in Tables 4.5 and 4.6 where the coefficient of variation of the discrete diffusivity,  $\varsigma_{\tilde{\alpha}}$ , and its mean,  $\overline{\varsigma_{\tilde{\alpha}}}$ , are presented. The tables show that  $\varsigma_{\tilde{\alpha}}$  generally grows with increasing dimensionless wavenumber. In terms of the  $\overline{\varsigma_{\tilde{\alpha}}}$  metric, and relative to the grid aspect ratio,  $\gamma = 1/2$  minimizes  $\theta$ -dependence for all but the FEM- $\mathbf{M}_c$  and SUCV  $\beta = 1/2$  semi-discretizations.

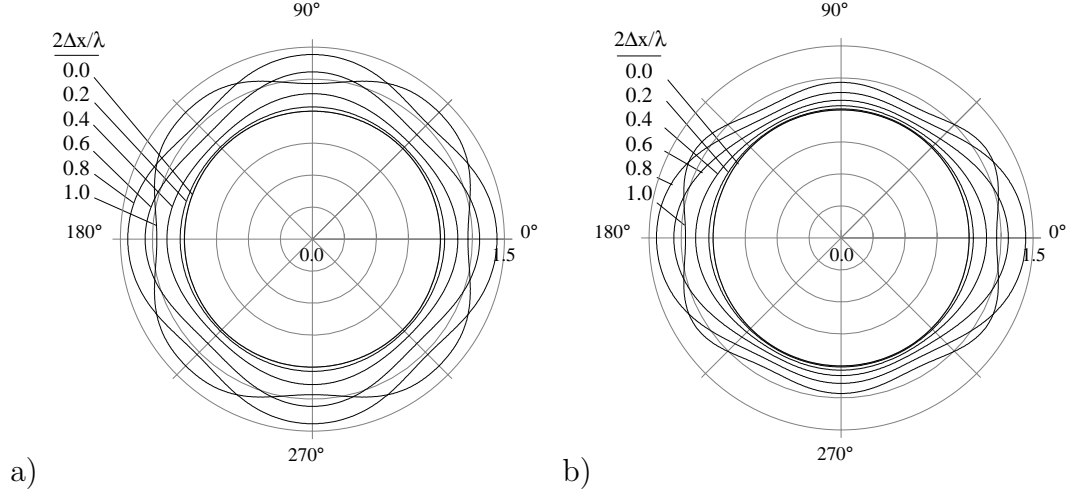


Figure 4.16: Non-dimensional discrete diffusivity for the consistent mass Galerkin finite element method with a)  $\gamma = 1$  and b)  $\gamma = 1/2$ .

Finally, it is evident from a method-to-method comparison of  $\overline{\varsigma_{\tilde{\alpha}}}$  that FEM- $\mathbf{M}_c$  and CVFEM- $\mathbf{M}_c$  minimize anisotropic behavior regardless of grid aspect ratio. Note that the SUCV and SUPG schemes can achieve equal or better anisotropy performance relative to FEM and CVFEM given the proper choice of  $\beta$  though a poor choice yields the overall worst anisotropy. It is also interesting to note that the best choice of stabilization parameter for SUCV ( $\beta = 1/2$ ) in terms of phase speed anisotropy (cf. Tables 4.1 and 4.2) is the worst choice for discrete diffusivity.

The series of figures in this section also provides information concerning the error in the discrete diffusivity relative to its continuum counterpart for each method. As suggested by the anisotropy discussion above, this error is dependent on wavenumber as well as propagation angle. A quantitative measure of the discrete diffusivity errors is presented in Tables 4.7 and 4.8. As with  $\varsigma_{\tilde{\alpha}}$ , the discrete diffusivity errors,  $\varepsilon_{\tilde{\alpha}}$ , generally increase with increasing  $2\Delta x/\lambda$ , peaking at the Nyquist limit. In terms of the  $\overline{\varepsilon_{\tilde{\alpha}}}$  metric, the  $\gamma = 1/2$  results minimize diffusivity errors relative to the unit aspect ratio cases for all the methods. Finally, it is evident from a method-to-method comparison of  $\overline{\varepsilon_{\tilde{\alpha}}}$  that CVFEM- $\mathbf{M}_c$  minimizes errors, irrespective of  $\gamma$ . Note that the SUPG and SUCV semi-discretizations yield by far the worst discrete diffusivity error (in terms of  $\overline{\varepsilon_{\tilde{\alpha}}}$ ) relative to the other semi-discretizations, irrespective of aspect ratio.

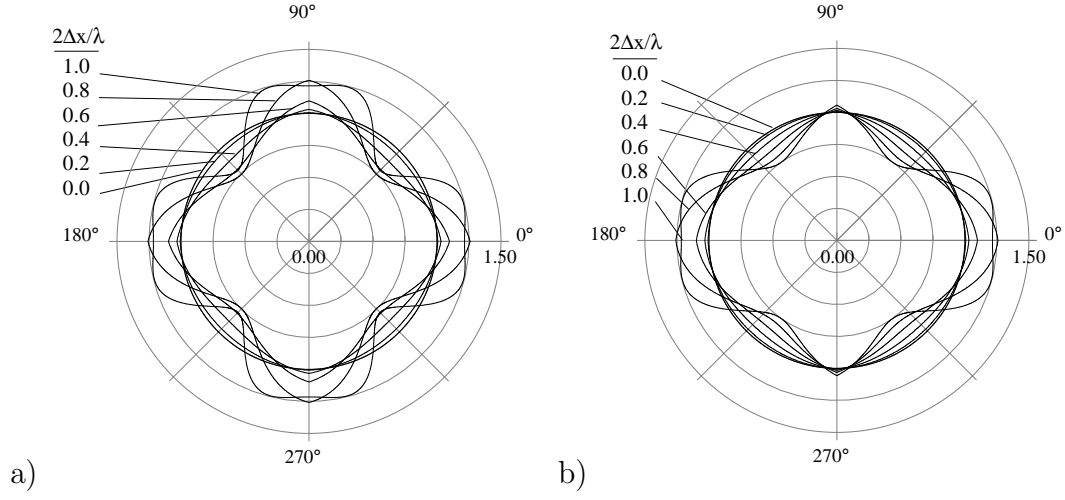


Figure 4.17: Non-dimensional discrete diffusivity ( $\tilde{\alpha}/\alpha$ ; radial) as a function of  $\theta$  (azimuthal) for consistent mass matrix finite element method SUPG with  $\beta_{opt}$  with a)  $\gamma = 1$  and b)  $\gamma = 1/2$ .

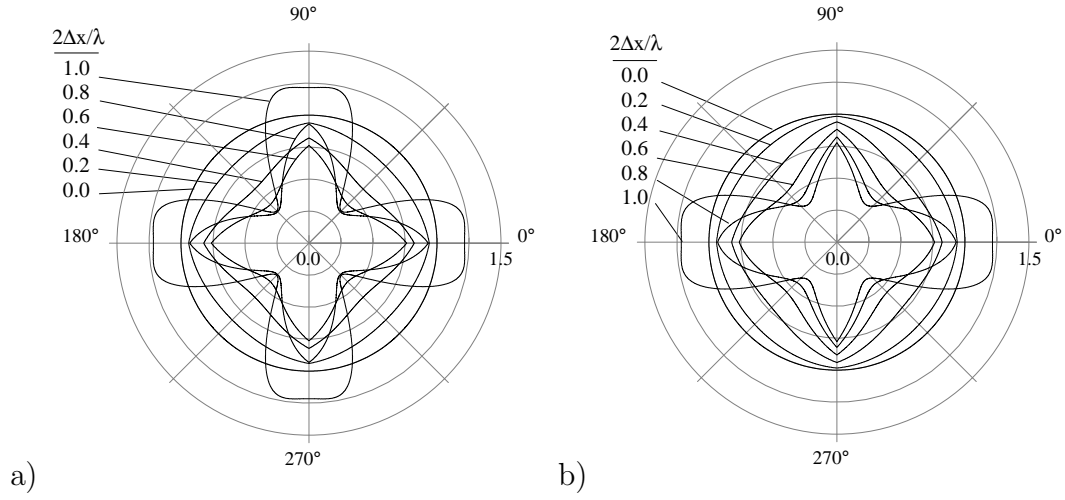


Figure 4.18: Non-dimensional discrete diffusivity ( $\tilde{\alpha}/\alpha$ ; radial) as a function of  $\theta$  (azimuthal) for consistent mass matrix finite element method SUPG with  $\beta = 1/2$  with a)  $\gamma = 1$  and b)  $\gamma = 1/2$ .

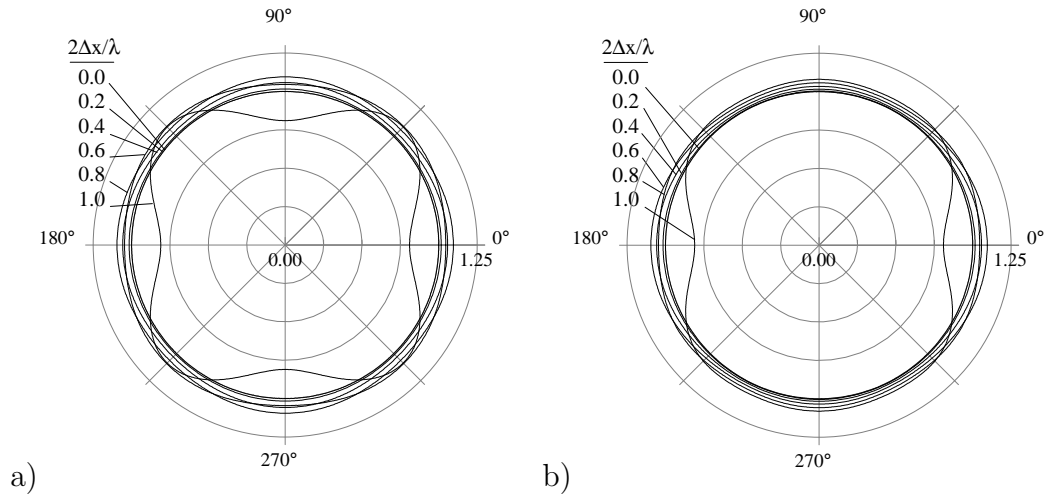


Figure 4.19: Non-dimensional discrete diffusivity for the consistent mass control volume finite element method with a)  $\gamma = 1$  and b)  $\gamma = 1/2$ .

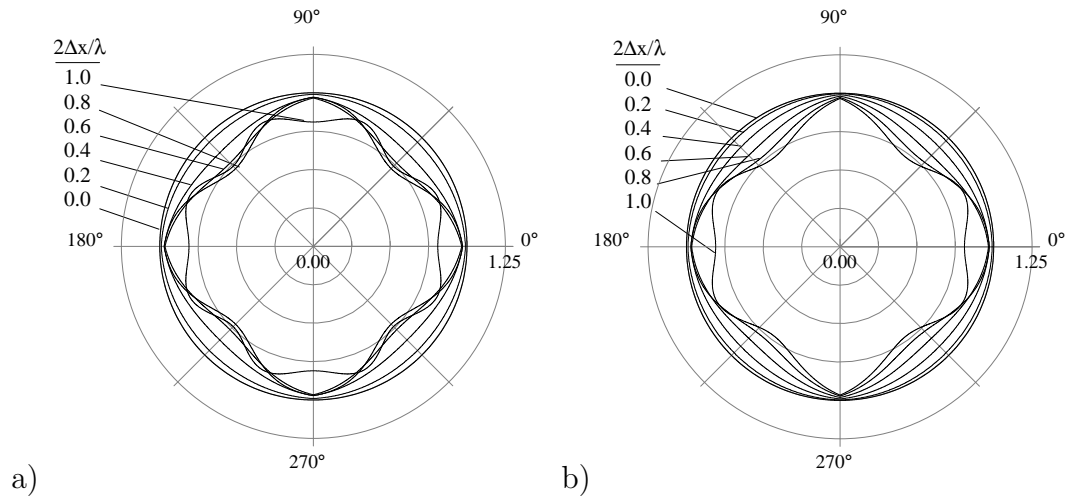


Figure 4.20: Non-dimensional discrete diffusivity ( $\tilde{\alpha}/\alpha$ ; radial) as a function of  $\theta$  (azimuthal) for consistent mass matrix control volume finite element method SUCV with  $\beta_{opt}$  with a)  $\gamma = 1$  and b)  $\gamma = 1/2$ .

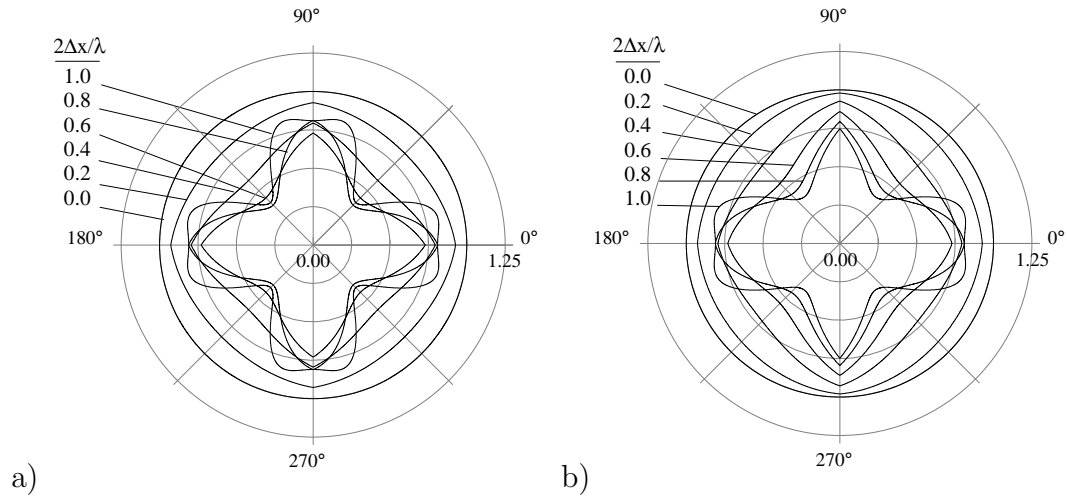


Figure 4.21: Non-dimensional discrete diffusivity ( $\tilde{\alpha}/\alpha$ ; radial) as a function of  $\theta$  (azimuthal) for consistent mass matrix control volume finite element method SUCV with  $\beta = 1/2$  with a)  $\gamma = 1$  and b)  $\gamma = 1/2$ .

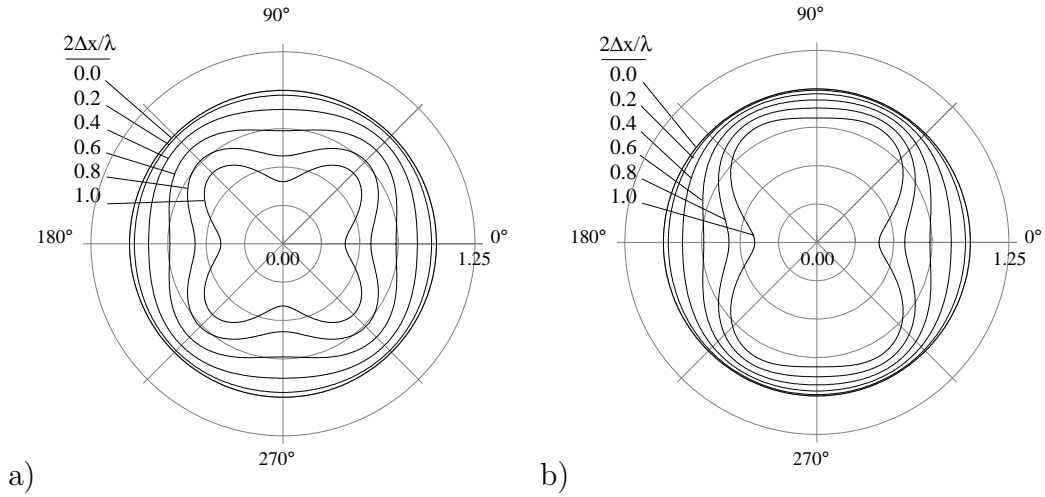


Figure 4.22: Non-dimensional discrete diffusivity for the finite difference method with first-order upwind and aspect ratios of a)  $\gamma = 1$  and b)  $\gamma = 1/2$ .

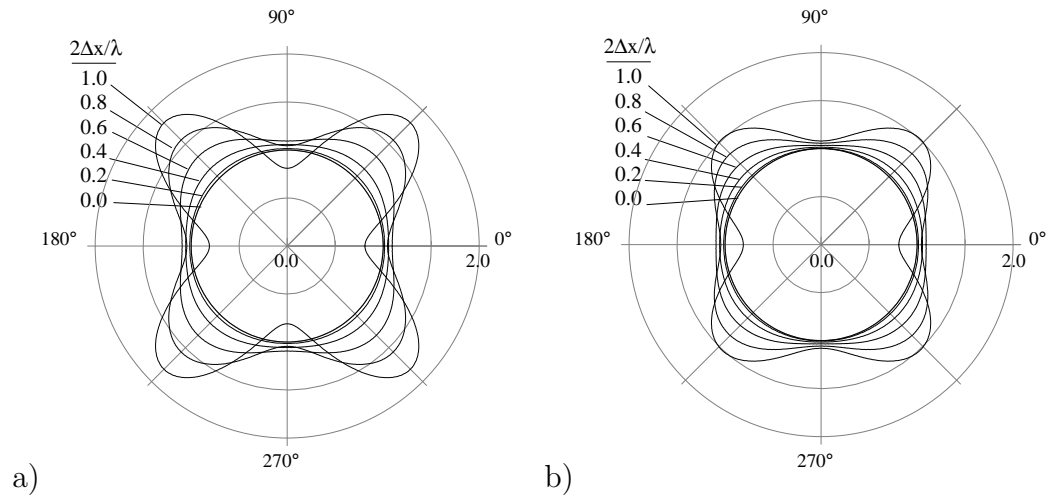


Figure 4.23: Non-dimensional discrete diffusivity ( $\tilde{\alpha}/\alpha$ ; radial) as a function of  $\theta$  (azimuthal) for the node-centered finite volume method with second order gradient approximation and consistent mass matrix with a)  $\gamma = 1$  and b)  $\gamma = 1/2$ .

Method	$\varsigma_{\bar{\alpha}}$ as a function of $2\Delta x/\lambda$						$\overline{\varsigma_{\bar{\alpha}}}$
	0.0	0.2	0.4	0.6	0.8	1.0	
FEM- $\mathbf{M}_c$	0.0	5.78e-3	2.24e-2	4.38e-2	4.35e-2	5.07e-2	2.82e-2
SUPG $\beta_{opt}$	0.0	1.35e-2	5.09e-2	1.07e-1	1.79e-1	1.56e-1	8.57e-2
SUPG $\beta = 1/2$	0.0	3.22e-2	1.02e-1	1.89e-1	3.32e-1	4.07e-1	1.72e-1
CVFEM- $\mathbf{M}_c$	0.0	5.85e-3	2.37e-2	5.47e-2	1.01e-1	1.64e-1	5.34e-2
SUCV $\beta_{opt}$	0.0	1.06e-2	3.85e-2	7.58e-2	1.04e-1	5.08e-2	5.08e-2
SUCV $\beta = 1/2$	0.0	2.17e-3	4.37e-3	1.77e-2	4.92e-2	5.81e-1	7.28e-2
FDM	0.0	1.19e-2	5.06e-2	1.29e-1	2.85e-1	7.00e-1	1.65e-1
FDM- $\mathbf{M}_c$	0.0	1.19e-2	5.21e-2	1.38e-1	3.22e-1	7.60e-1	1.81e-1

Table 4.5: Coefficient of Variation of discrete diffusivity,  $\varsigma_{\bar{\alpha}}$ , as a function of  $2\Delta x/\lambda$ , and its average,  $\overline{\varsigma_{\bar{\alpha}}}$ , for the two-dimensional,  $\gamma = 1$ , semi-discretizations considered here.



Method	$\varsigma_{\tilde{\alpha}}$ as a function of $2\Delta x/\lambda$						$\overline{\varsigma_{\tilde{\alpha}}}$
	0.0	0.2	0.4	0.6	0.8	1.0	
FEM - $\mathbf{M}_c$	0.0	9.45e-3	3.73e-2	7.78e-2	1.01e-1	4.29e-2	4.94e-2
SUPG $\beta_{opt}$	0.0	7.78e-3	3.10e-2	7.29e-2	1.48e-1	1.84e-1	7.03e-2
SUPG $\beta = 1/2$	0.0	2.37e-2	7.73e-2	1.34e-1	2.43e-1	4.48e-1	1.40e-1
CVFEM- $\mathbf{M}_c$	0.0	4.56e-3	1.58e-2	2.34e-2	7.75e-3	9.27e-2	1.96e-2
SUCV $\beta_{opt}$	0.0	6.21e-3	2.30e-2	4.78e-2	7.76e-2	7.71e-2	3.86e-2
SUCV $\beta = 1/2$	0.0	2.51e-2	7.76e-2	1.26e-1	2.01e-1	2.80e-1	1.14e-1
FDM	0.0	9.46e-3	3.78e-2	8.47e-2	1.49e-1	2.30e-1	7.92e-2
FDM- $\mathbf{M}_c$	0.0	5.58e-3	2.12e-2	4.48e-2	8.54e-2	1.79e-1	4.94e-2

Table 4.6: Coefficient of Variation of discrete diffusivity,  $\varsigma_{\tilde{\alpha}}$ , as a function of  $2\Delta x/\lambda$ , and its average,  $\overline{\varsigma_{\tilde{\alpha}}}$ , for the two-dimensional,  $\gamma = 1/2$  semi-discretizations considered here.

Method	$\varepsilon_{\tilde{\alpha}}$ as a function of $2\Delta x/\lambda$						$\overline{\varepsilon_{\tilde{\alpha}}}$
	0.0	0.2	0.4	0.6	0.8	1.0	
FEM- $\mathbf{M}_c$	0.0	2.56e-2	1.05e-1	2.38e-1	3.70e-1	3.26e-1	1.80e-1
SUPG $\beta_{opt}$	0.0	2.18e-2	7.37e-2	1.26e-1	1.76e-1	1.88e-1	9.84e-2
SUPG $\beta = 1/2$	0.0	1.20e-1	3.28e-1	4.61e-1	4.63e-1	3.78e-1	3.12e-1
CVFEM- $\mathbf{M}_c$	0.0	1.24e-2	4.56e-2	8.06e-2	7.19e-2	1.12e-1	5.33e-2
SUCV $\beta_{opt}$	0.0	3.04e-2	9.92e-2	1.60e-1	1.79e-1	1.84e-1	1.12e-1
SUCV $\beta = 1/2$	0.0	1.28e-1	3.37e-1	4.60e-1	4.65e-1	3.81e-1	3.16e-1
FDM	0.0	2.51e-2	9.69e-2	2.06e-1	3.39e-1	4.79e-1	1.81e-1
FDM- $\mathbf{M}_c$	0.0	2.54e-2	1.01e-1	2.19e-1	3.49e-1	4.51e-1	1.84e-1

Table 4.7: RMS discrete diffusivity error,  $\varepsilon_{\tilde{\alpha}}$ , as a function of  $2\Delta x/\lambda$ , and its average,  $\overline{\varepsilon_{\tilde{\alpha}}}$ , for the two-dimensional,  $\gamma = 1$  semi-discretizations considered here.

Method	$\varepsilon_{\tilde{\alpha}}$ as a function of $2\Delta x/\lambda$						$\overline{\varepsilon_{\tilde{\alpha}}}$
	0.0	0.2	0.4	0.6	0.8	1.0	
FEM- $\mathbf{M}_c$	0.0	1.83e-2	7.50e-2	1.70e-1	2.65e-1	2.46e-1	1.30e-1
SUPG $\beta_{opt}$	0.0	1.19e-2	4.32e-2	8.57e-2	1.47e-1	1.82e-1	7.57e-2
SUPG $\beta = 1/2$	0.0	7.37e-2	2.26e-1	3.56e-1	4.15e-1	4.38e-1	2.58e-1
CVFEM- $\mathbf{M}_c$	0.0	8.86e-3	3.27e-2	5.86e-2	5.79e-2	9.32e-2	4.09e-2
SUCV $\beta_{opt}$	0.0	1.75e-2	6.11e-2	1.11e-1	1.50e-1	1.91e-1	8.70e-2
SUCV $\beta = 1/2$	0.0	7.96e-2	2.37e-1	3.64e-1	4.25e-1	4.43e-1	2.65e-1
FDM	0.0	1.79e-2	6.92e-2	1.48e-1	2.43e-1	3.46e-1	1.30e-1
FDM- $\mathbf{M}_c$		1.64e-2	6.44e-2	1.38e-1	2.19e-1	3.05e-1	1.18e-1

Table 4.8: RMS discrete diffusivity error,  $\varepsilon_{\tilde{\alpha}}$ , as a function of  $2\Delta x/\lambda$ , and its average,  $\overline{\varepsilon_{\tilde{\alpha}}}$ , for the two-dimensional,  $\gamma = 1/2$  semi-discretizations considered here.

## 4.4 Artificial Diffusivity

This section examines artificial diffusivity associated with our two-dimensional semi-discretizations. As noted earlier, artificial diffusion may be added deliberately (e.g. SUPG/SUCV) or be a by-product of the discretization (e.g. first-order upwind). While in general not a desirable feature of a method, artificial diffusivity can be used to stabilize a discretization scheme. In terms of artificial diffusivity, stabilization is achieved through the annihilation (damping) of numerical artifacts such as high-frequency dispersion errors in under-resolved convection-dominated problems. In this light, an ideal artificial diffusivity function would only be active in the high frequency spectrum, near the Nyquist limit for example, and be negligible otherwise, going to zero at the long wavelength limit. This feature of artificial diffusivity is shared for both one- and two-dimensional discretizations. For the two-dimensional discretizations, it is also desirable for the artificial diffusivity have an angular variation proportional to the angular variation of phase error so that high-frequency dispersion errors are damped at the same rate, irregardless of propagation direction.

This section begins with a presentation of the analytic expressions for the non-dimensional artificial diffusivity, presented in terms of  $1/\mathbf{P}_e^{art}$  ( $= 2\alpha_{art}/c\Delta x$ ), for all the semi-discrete methods considered. A summary of the artificial diffusivity results in terms of polar plots and the anisotropy and error metrics follows. These results demonstrate the aspect ratio, wavelength and propagation angle dependence of the individual methods and provide a means of comparison between methods.

### 4.4.1 2D Artificial Diffusivity Formulae

As was the case for several of the previous two-dimensional discrete phase speed and diffusivity formulae, the two-dimensional formulae for artificial diffusivity for FEM, CVFEM, CD, SOU, TOU, Fromm, and QUICK can be written in the form,

$$\begin{aligned} \frac{2\alpha_{art}}{c} &= (\Delta x \cos \theta) \cos^2 \theta F_{\alpha_{art}}^{1D}(k\Delta x \cos \theta) \\ &+ (\Delta y \sin \theta) \sin^2 \theta F_{\alpha_{art}}^{1D}(k\Delta y \sin \theta) \end{aligned} \quad (4.25)$$

where  $F_{\alpha_{art}}^{1D}(x)$  denotes the dimensionless 1-D formula for artificial diffusivity as given in Table 3.8. In terms of the  $\mathbf{P}_e^{art}$  defined previously, the formula becomes

$$\frac{2\alpha_{art}}{c\Delta x} = \cos^3 \theta F_{\alpha_{art}}^{1D}(k\Delta x \cos \theta) + \gamma \sin^3 \theta F_{\alpha_{art}}^{1D}(\gamma k\Delta x \sin \theta) \quad (4.26)$$

Again, note that for  $\theta = \pi/4$  and  $\gamma = 1$ , we get the 1-D formula for artificial diffusivity on a smaller mesh spacing

$$\frac{2\alpha_{art}}{c(\sqrt{2}\Delta x/2)} = F_{\alpha_{art}}^{1D}(k\sqrt{2}\Delta x/2) \quad (4.27)$$

in which the dimensionless Peclet number is modified to account for the smaller mesh spacing. In general, when  $1/\gamma = \tan \theta$  (and therefore  $\Delta x \cos \theta = \Delta y \sin \theta$ ) Eq.(4.26) takes the form

$$\frac{2\alpha_{art}}{c\Delta x \cos \theta} = F_{\alpha_{art}}^{1D}(k\Delta x \cos \theta) \quad (4.28)$$

once again illustrating the 1-D nature of the artificial diffusion when the wave is propagating perpendicular to the mesh diagonals. In this case the scaling for dimensionless artificial diffusion includes the effective mesh spacing and the artificial diffusion function is the 1-D function with the effective wavenumber ( $k\Delta x \cos \theta$ ) as argument. Notice that this effective wavenumber has a restricted range ( $0 \leq 2\Delta x/\lambda \leq \cos \theta$ ) compared to the range in the 1-D case ( $0 \leq 2\Delta x/\lambda \leq 1$ ). This means, for example, that the effective Nyquist wavenumber when  $\theta = \pi/3$  say (i.e,  $\gamma = 1/\tan \theta = 1/\sqrt{3}$ ) is  $\sqrt{3}/2$ , rather than unity.

The remaining schemes do not have as simple a form as Eq. (4.26); these include the LSR schemes, SUPG and SUCV. Dimensionless artificial diffusivity for the LSR(-1) scheme is,

$$\begin{aligned} \frac{2\alpha_{art}}{c\Delta x} &= \frac{\cos^2 \theta}{3\theta_x^2} [11 + (1 + 2 \cos \theta_y) \cos 2\theta_x - 12 \cos \theta_x - 2 \cos \theta_y] \\ &+ \frac{\sin^2 \theta}{3\theta_y^2} [11 + (1 + 2 \cos \theta_x) \cos 2\theta_y - 12 \cos \theta_y - 2 \cos \theta_x] \end{aligned} \quad (4.29)$$

In 1-D this reduces to the artificial diffusion formula for SOU. The dimensionless artificial diffusion formula for LSR(0) is 1/2 times the formula for LSR(-1), which in 1-D reduces to the formula for Fromm's method. These artificial diffusion functions are similar to the simple form given above, however they do not separate into x- and y- component function but instead contain cross-terms.

The artificial diffusivity for SUPG and SUCV are given by:

$$\frac{2\alpha_{art}}{c\Delta x} = 4\beta_\theta \frac{\left[ \frac{\cos^4 \theta}{\theta_x^2 \mathcal{M}(\theta_x)} \left( (1 - \cos \theta_x) - \frac{\sin^2 \theta}{2\mathcal{M}(\theta_x)} \right) + \frac{\sin^4 \theta}{\theta_y^2 \mathcal{M}(\theta_y)} \left( (1 - \cos \theta_y) - \frac{\sin^2 \theta}{2\mathcal{M}(\theta_y)} \right) \right]}{\left[ 1 + \beta^2(\theta_x + \theta_y)^2 \left( \cos^2 \theta \mathcal{G}(\theta_x) + \sin^2 \theta \mathcal{G}(\theta_y) \right)^2 \right]} \quad (4.30)$$

in terms of the definitions in Eq. (4.19) and the symbol for the mass matrix,  $\mathcal{M}(\theta)$  given in Table 3.1. For example,  $\mathcal{M}(\theta_x) = (2 + \cos \theta_x)/3$  for SUPG, and  $\mathcal{M}(\theta_x) = (3 + \cos \theta_x)/4$  for SUCV. The similarity of the various terms to the 1-D version is clear. The formulae revert to the corresponding 1-D formulae along the coordinate directions.

#### 4.4.2 2D Artificial Diffusivity Results

The artificial diffusivity results for the two-dimensional semi-discretizations are presented in Figures 4.24 to 4.34. Figures (a) and (b) for each method present dimensionless artificial diffusivity,  $1/\mathbf{P}_e^{art}$ , for grid aspect ratios of  $\gamma = 1$  and  $1/2$  respectively. Dimensionless artificial diffusivity curves are plotted for  $2\Delta x/\lambda = 0, 0.2, 0.4, 0.6, 0.8$  and  $1.0$ .

From the series of figures presented in this section, it is clear that the artificial diffusivity displays significant anisotropy. A comparison of the different aspect ratio results for each method demonstrates greater anisotropy for the  $\gamma = 1/2$  cases. Additionally, all the methods show quarter- and half-symmetry for the  $\gamma = 1$  and  $1/2$  aspect ratio cases respectively – consistent with the symmetry of the underlying spatial grid.

Tables 4.9 and 4.10 present the coefficient of variation of dimensionless artificial diffusivity,  $\varsigma_{art}$ , and its mean,  $\overline{\varsigma_{art}}$ , and clearly demonstrate the aspect ratio dependence of the anisotropy. The tables show that  $\overline{\varsigma_{art}}$  is significantly greater for the  $\gamma = 1/2$  grids relative to their unit aspect ratio counterparts. In terms of the  $\varsigma_{art}$  metric, the finite difference schemes show decreasing anisotropy with wavenumber while the SUPG and SUCV methods generally demonstrate the opposite behavior. This SUPG/SUCV wavenumber dependence of anisotropy is not optimal because, ideally, artificial diffusivity becomes active in the high wavenumber region. It is also evident from the tables that the FOU, SOU, TOU, Fromm's and QUICK schemes produce identical anisotropy metric values as their stencils differ only by a multiplier that is independent of  $\theta$  (see Appendix A) and hence drops out of the metric calculation (see Eq. 4.1). The two LSR schemes also share a common stencil (differing by a  $\theta$ -independent multiplier) and hence also demonstrate identical anisotropy metrics.

The series of figures in this section also provides information concerning the magnitude of the artificial diffusivity of each method. As suggested by the anisotropy discussion above, artificial diffusivity is dependent on wavenumber and propagation direction. Indeed, the figures demonstrate that artificial diffusivity is generally maximized along the x and y-coordinate directions when  $\gamma = 1$ , and along the x-coordinate direction for  $\gamma = 1/2$ . Recall that these directions correspond to the worst phase speed accuracy for each of these aspect ratios. Artificial diffusivity is generally minimized along the  $\theta = \pi/4$

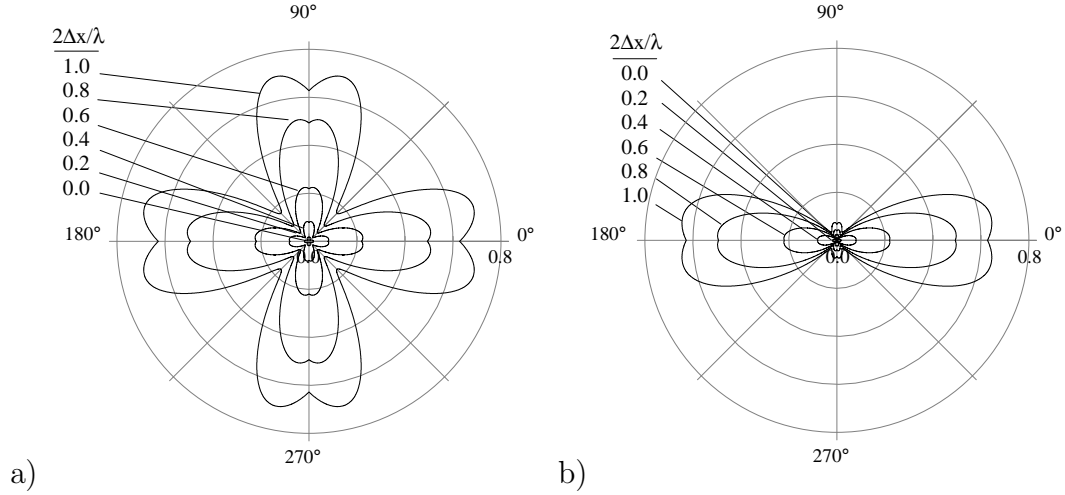


Figure 4.24: Non-dimensional artificial diffusivity ( $1/\mathbf{P}_e^{art}$ ; radial) as a function of  $\theta$  (azimuthal) for consistent mass matrix finite element method SUPG with  $\beta_{opt}$  with a)  $\gamma = 1$  and b)  $\gamma = 1/2$ .

direction when  $\gamma = 1$ , corresponding to the best dispersion accuracy for the methods considered here. Hence, the anisotropy of the artificial diffusivity is consistent with the anisotropy of the concomitant dispersive behavior. A quantitative measure of the dimensionless artificial diffusivity is presented in Tables 4.11 and 4.12 for the  $\gamma = 1$  and  $1/2$  aspect ratio cases respectively. All but the FOU semi-discretizations demonstrate generally increasing artificial diffusivity, in terms of the  $\varepsilon_{art}$  metric, with increasing wavenumber. As with the one-dimensional results, FOU demonstrates dimensionless artificial diffusivity which *decreases* with wavenumber. In terms of the  $\overline{\varepsilon_{art}}$  metric, the FOU and LSR(-1) methods show the greatest amount of damping while the SUPG, SUCV and TOU schemes produce the least artificial diffusivity as measured in this metric.

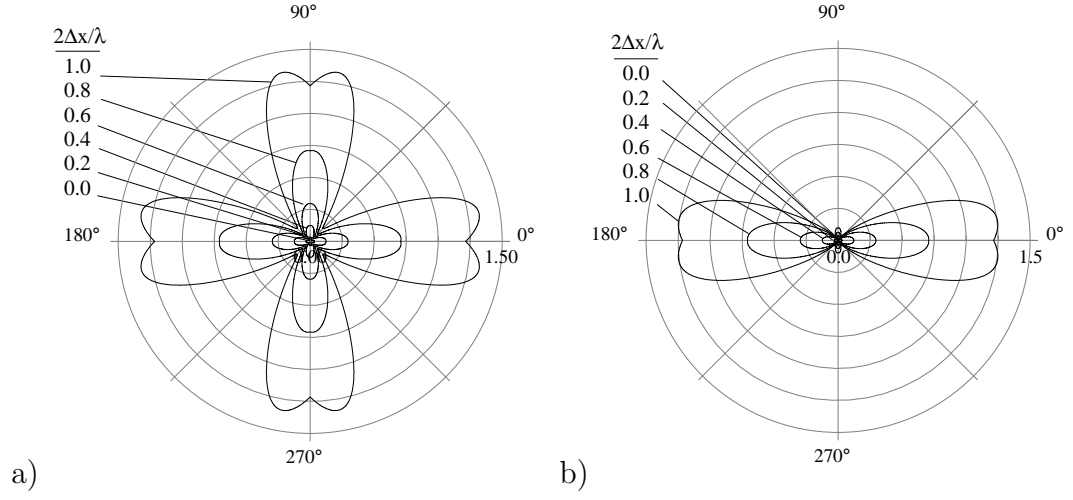


Figure 4.25: Non-dimensional artificial diffusivity ( $1/\mathbf{P}_e^{art}$ ; radial) as a function of  $\theta$  (azimuthal) for consistent mass matrix finite element method SUPG with  $\beta = 1/2$  with a)  $\gamma = 1$  and b)  $\gamma = 1/2$ .

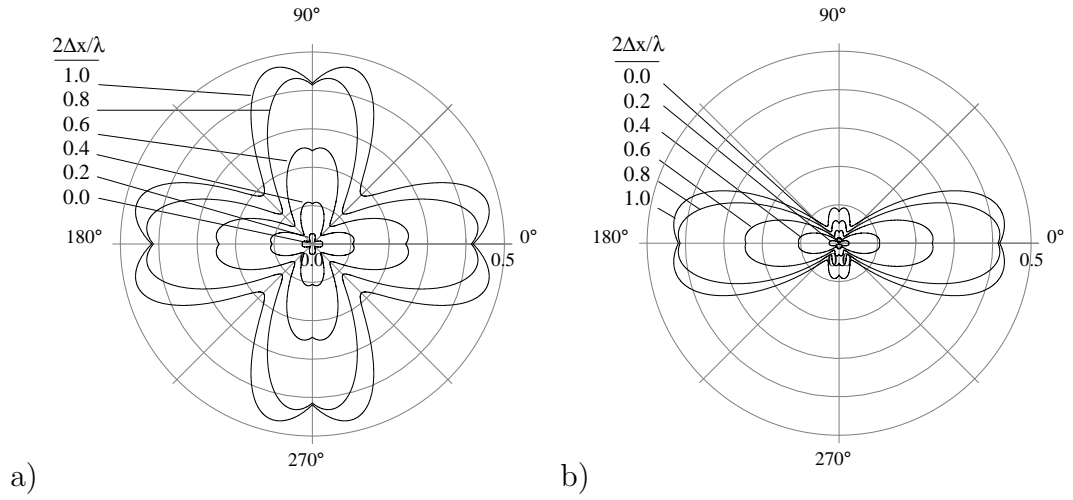


Figure 4.26: Non-dimensional artificial diffusivity ( $1/\mathbf{P}_e^{art}$ ; radial) as a function of  $\theta$  (azimuthal) for consistent mass matrix control volume finite element method SUCV with  $\beta_{opt}$  with a)  $\gamma = 1$  and b)  $\gamma = 1/2$ .

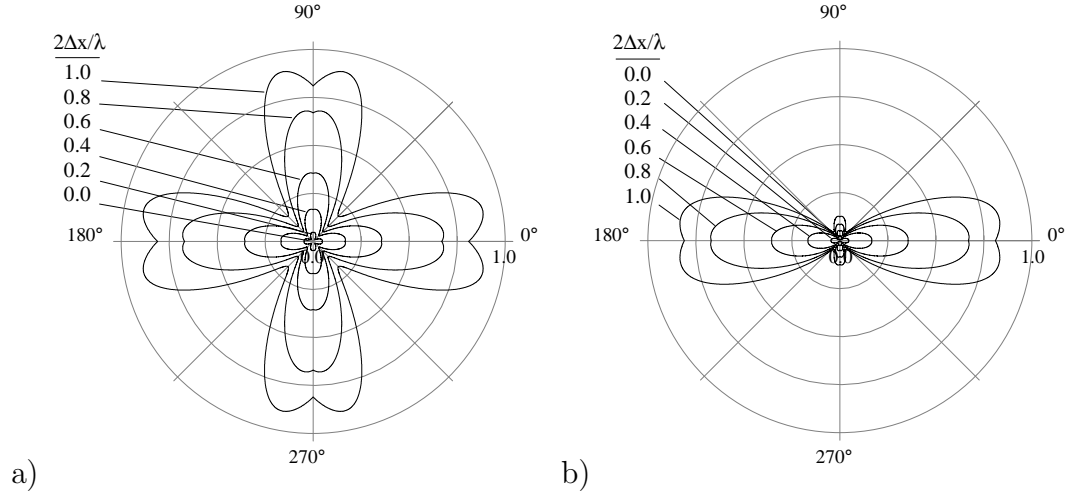


Figure 4.27: Non-dimensional artificial diffusivity ( $1/\mathbf{P}_e^{art}$ ; radial) as a function of  $\theta$  (azimuthal) for consistent mass matrix control volume finite element method SUCV with  $\beta = 1/2$  with a)  $\gamma = 1$  and b)  $\gamma = 1/2$  (right).

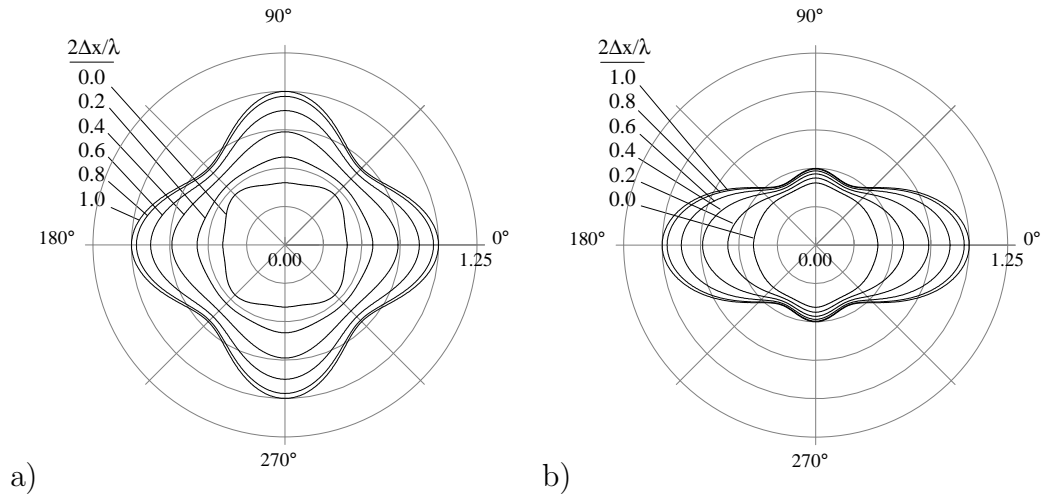


Figure 4.28: Non-dimensional artificial diffusivity ( $1/\mathbf{P}_e^{art}$ ; radial) as a function of  $\theta$  (azimuthal) for the first-order upwind (FOU) semi-discretization. Results for aspect ratios of a)  $\gamma = 1$  and b)  $\gamma = 1/2$  are shown.



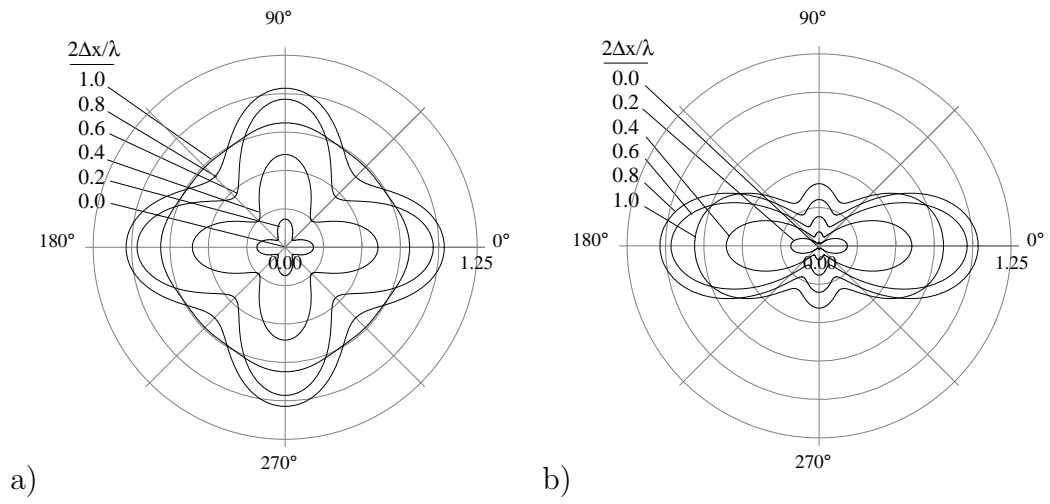


Figure 4.29: Non-dimensional artificial diffusivity ( $1/\mathbf{P}_e^{art}$ ; radial) as a function of  $\theta$  (azimuthal) for the second-order upwind (SOU) semi-discretization. Results are shown for a)  $\gamma = 1$  and b)  $\gamma = 1/2$ .

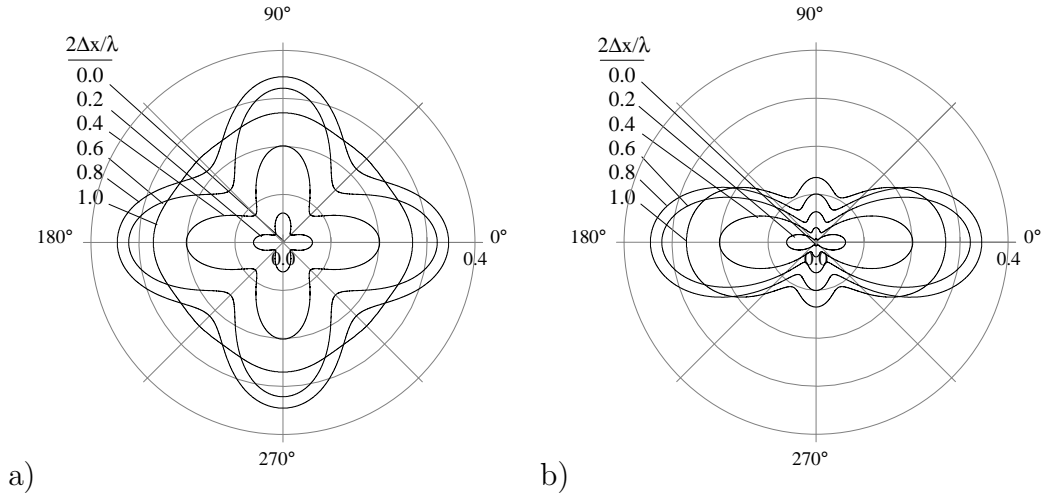


Figure 4.30: Non-dimensional artificial diffusivity ( $1/\mathbf{P}_e^{art}$ ; radial) as a function of  $\theta$  (azimuthal) for the third-order upwind (TOU) semi-discretization. Results are shown for a)  $\gamma = 1$  and b)  $\gamma = 1/2$ .

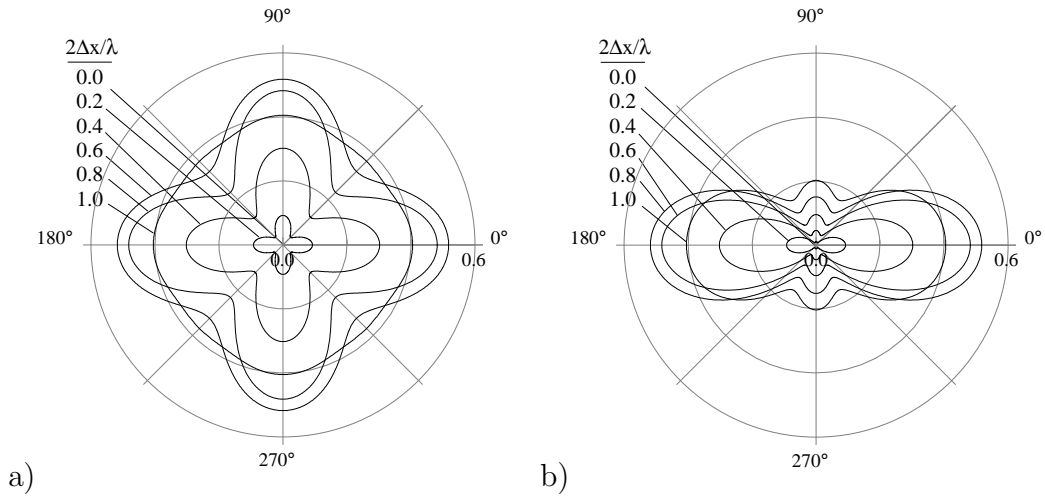


Figure 4.31: Non-dimensional artificial diffusivity ( $1/\mathbf{P}_e^{art}$ ; radial) as a function of  $\theta$  (azimuthal) for Fromm's method. Results for a)  $\gamma = 1$  and b)  $\gamma = 1/2$  are shown.

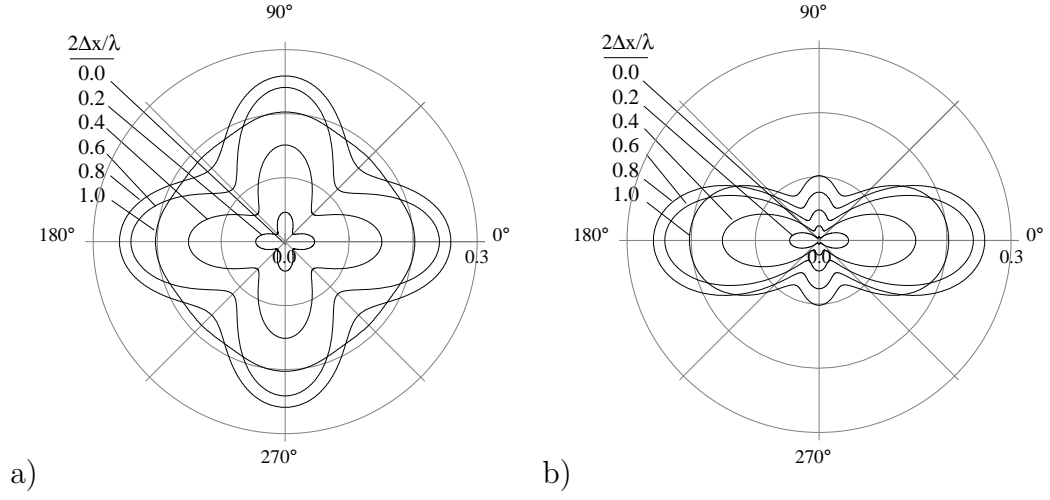


Figure 4.32: Non-dimensional artificial diffusivity ( $1/\mathbf{P}_e^{art}$ ; radial) as a function of  $\theta$  (azimuthal) for the QUICK semi-discretization. Results for a)  $\gamma = 1$  and b)  $\gamma = 1/2$  are shown.

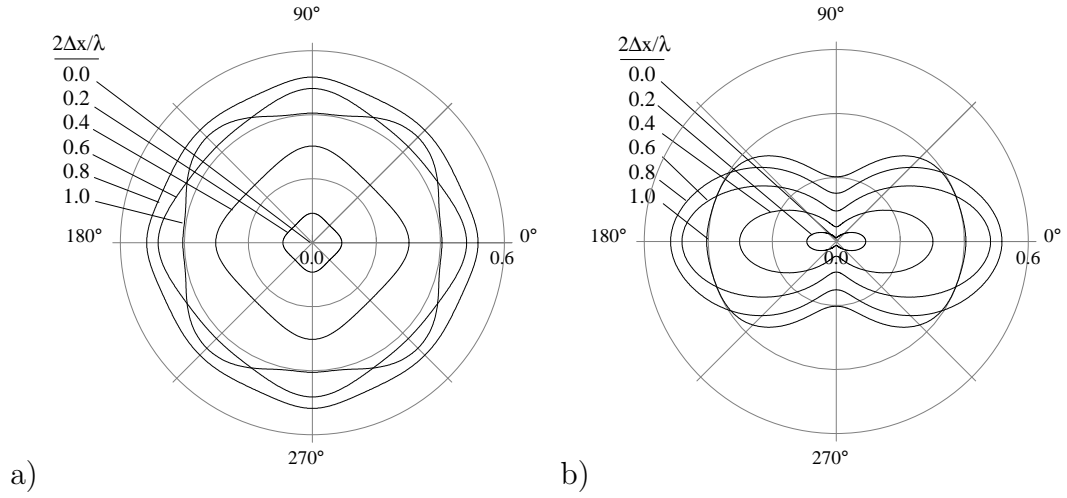


Figure 4.33: Non-dimensional artificial diffusivity ( $1/\mathbf{P}_e^{art}$ ; radial) as a function of  $\theta$  (azimuthal) for the least squares reconstruction (LSR(0);  $\theta = 1.$ ,  $\kappa = 0$ ). Results for a)  $\gamma = 1$  and b)  $\gamma = 1/2$  are shown.

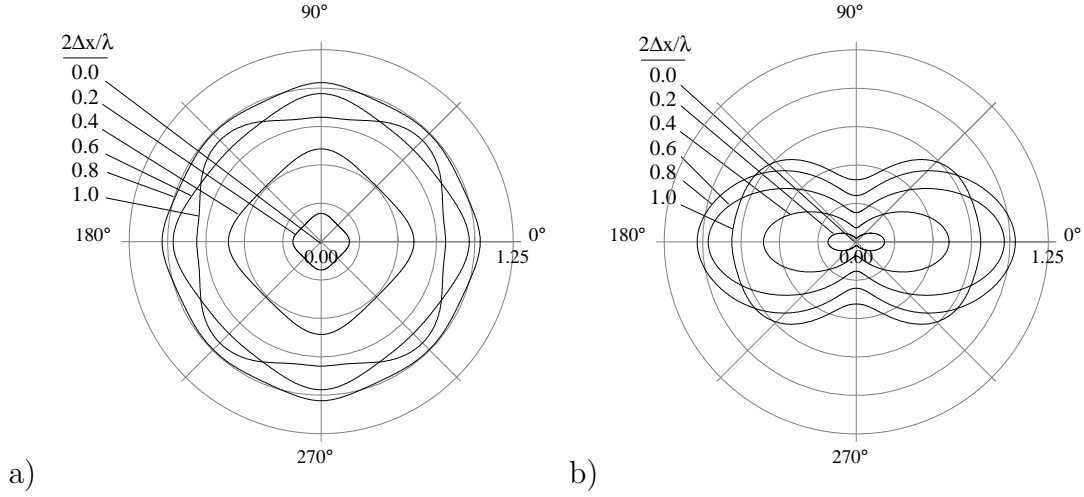


Figure 4.34: Non-dimensional artificial diffusivity ( $1/\mathbf{P}_e^{art}$ ; radial) as a function of  $\theta$  (azimuthal) for the least squares reconstruction (LSR(-1);  $\theta = 1.$ ,  $\kappa = -1$ ). Results for a)  $\gamma = 1$  and b)  $\gamma = 1/2$  are shown.

Method	$\varsigma_{art}$ as a function of $2\Delta x/\lambda$						$\overline{\varsigma_{art}}$
	0.0	0.2	0.4	0.6	0.8	1.0	
SUPG $\beta_{opt}$	0.0	3.56e-1	3.96e-1	4.51e-1	4.97e-1	4.05e-1	3.81e-1
SUPG $\beta = 1/2$	0.0	3.71e-1	4.35e-1	5.14e-1	6.12e-1	5.91e-1	4.46e-1
SUCV $\beta_{opt}$	0.0	3.52e-1	3.78e-1	4.07e-1	4.09e-1	2.90e-1	3.39e-1
SUCV $\beta = 1/2$	0.0	3.67e-1	4.20e-1	4.81e-1	5.36e-1	4.59e-1	4.08e-1
FOU	0.0	1.16e-1	9.81e-2	6.73e-2	2.16e-2	4.88e-2	7.75e-2
SOU	0.0	3.27e-1	2.98e-1	2.46e-1	1.62e-1	3.52e-2	2.11e-1
TOU	0.0	3.27e-1	2.98e-1	2.46e-1	1.62e-1	3.52e-2	2.11e-1
Fromm's	0.0	3.27e-1	2.98e-1	2.46e-1	1.62e-1	3.52e-2	2.11e-1
QUICK	0.0	3.27e-1	2.98e-1	2.46e-1	1.62e-1	3.52e-2	2.11e-1
LSR(0)	0.0	6.59e-2	5.98e-2	4.56e-2	1.64e-2	5.40e-2	4.52e-2
LSR(-1)	0.0	6.59e-2	5.98e-2	4.56e-2	1.64e-2	5.40e-2	4.75e-2

Table 4.9: Coefficient of Variation of  $1/\mathbf{P}_e^{art}$ ,  $\varsigma_{art}$ , as a function of  $2\Delta x/\lambda$ , and its average,  $\overline{\varsigma_{art}}$ , for the two-dimensional,  $\gamma = 1$  semi-discretizations considered here.

Method	$\varsigma_{art}$ as a function of $2\Delta x/\lambda$						$\overline{\varsigma_{art}}$
	0.0	0.2	0.4	0.6	0.8	1.0	
SUPG $\beta_{opt}$	0.0	8.61e-1	9.02e-1	9.67e-1	1.03	9.53e-1	8.48e-1
SUPG $\beta = 1/2$	0.0	8.54e-1	8.85e-1	9.60e-1	1.10	1.14	8.75e-1
SUCV $\beta_{opt}$	0.0	8.52e-1	8.69e-1	8.93e-1	8.93e-1	7.57e-1	7.78e-1
SUCV $\beta = 1/2$	0.0	8.46e-1	8.58e-1	9.07e-1	9.91e-1	9.50e-1	8.16e-1
FOU	0.0	2.97e-1	2.64e-1	2.08e-1	1.26e-1	2.14e-2	2.12e-1
SOU	0.0	8.40e-1	7.91e-1	7.02e-1	5.61e-1	3.49e-1	6.15e-1
TOU	0.0	8.40e-1	7.91e-1	7.02e-1	5.61e-1	3.49e-1	6.15e-1
Fromm's	0.0	8.40e-1	7.91e-1	7.02e-1	5.61e-1	3.49e-1	6.15e-1
QUICK	0.0	8.40e-1	7.91e-1	7.02e-1	5.61e-1	3.49e-1	6.15e-1
LSR(0)	0.0	6.32e-1	5.87e-1	5.07e-1	3.85e-1	2.24e-1	4.46e-1
LSR(-1)	0.0	6.32e-1	5.87e-1	5.07e-1	3.85e-1	2.24e-1	4.48e-1

Table 4.10: Coefficient of Variation of  $1/\mathbf{P}_e^{art}$ ,  $\varsigma_{art}$ , as a function of  $2\Delta x/\lambda$ , and its average,  $\overline{\varsigma_{art}}$ , for the two-dimensional,  $\gamma = 1/2$  semi-discretizations considered here.

Method	$\varepsilon_{art}$ as a function of $2\Delta x/\lambda$						$\overline{\varepsilon_{art}}$
	0.0	0.2	0.4	0.6	0.8	1.0	
SUPG $\beta_{opt}$	0.0	1.40e-2	6.03e-2	1.57e-1	3.48e-1	5.29e-1	1.69e-1
SUPG $\beta = 1/2$	0.0	2.47e-2	8.66e-2	1.92e-1	4.36e-1	9.13e-1	2.39e-1
SUCV $\beta_{opt}$	0.0	2.04e-2	8.06e-2	1.81e-1	3.14e-1	3.75e-1	1.57e-1
SUCV $\beta = 1/2$	0.0	3.60e-2	1.19e-1	2.39e-1	4.45e-1	6.50e-1	2.33e-1
FOU	8.55e-1	8.32e-1	7.67e-1	6.69e-1	5.50e-1	4.26e-1	6.92e-1
SOU	0.0	1.33e-1	4.46e-1	7.42e-1	8.58e-1	7.68e-1	5.13e-1
TOU	0.0	4.44e-2	1.49e-1	2.47e-1	2.86e-1	2.56e-1	1.71e-1
Fromm's	0.0	6.67e-2	2.23e-1	3.71e-1	4.29e-1	3.84e-1	2.56e-1
QUICK	0.0	1.04e-2	3.19e-2	4.42e-2	3.43e-2	6.75e-3	2.48e-2
LSR(0)	0.0	8.39e-2	2.76e-1	4.47e-1	5.00e-1	4.31e-1	3.05e-1
LSR(-1)	0.0	1.68e-1	5.52e-1	8.95e-1	1.00	8.63e-1	6.09e-1

Table 4.11: RMS value of  $1/\mathbf{P}_e^{art}$ ,  $\varepsilon_{art}$ , as a function of  $2\Delta x/\lambda$ , and its average,  $\overline{\varepsilon_{art}}$ , for the two-dimensional  $\gamma = 1$  semi-discretizations considered here.

Method	$\varepsilon_{art}$ as a function of $2\Delta x/\lambda$						$\overline{\varepsilon_{art}}$
	0.0	0.2	0.4	0.6	0.8	1.0	
SUPG $\beta_{opt}$	0.0	9.07e-3	3.98e-2	1.06e-1	2.34e-1	3.44e-1	1.12e-1
SUPG $\beta = 1/2$	0.0	1.63e-2	6.00e-2	1.36e-1	3.09e-1	6.08e-1	1.65e-1
SUCV $\beta_{opt}$	0.0	1.32e-2	5.31e-2	1.21e-1	2.09e-1	2.42e-1	1.03e-1
SUCV $\beta = 1/2$	0.0	2.38e-2	8.19e-2	1.68e-1	3.09e-1	4.28e-1	1.59e-1
FOU	6.66e-1	6.51e-1	6.09e-1	5.45e-1	4.70e-1	3.92e-1	5.61e-1
SOU	0.0	9.36e-2	3.13e-1	5.21e-1	6.08e-1	5.62e-1	3.63e-1
TOU	0.0	3.12e-2	1.04e-1	1.74e-1	2.03e-1	1.87e-1	1.21e-1
Fromm's	0.0	4.68e-2	1.57e-1	2.61e-1	3.04e-1	2.81e-1	1.82e-1
QUICK	0.0	2.34e-2	7.83e-2	1.30e-1	1.52e-1	1.40e-1	9.09e-2
LSR(0)	0.0	5.18e-2	1.74e-1	2.95e-1	3.53e-1	3.41e-1	2.09e-1
LSR(-1)	0.0	1.04e-1	3.49e-1	5.89e-1	7.05e-1	6.82e-1	4.18e-1

Table 4.12: RMS value of  $1/\mathbf{P}_e^{art}$ ,  $\varepsilon_{art}$ , as a function of  $2\Delta x/\lambda$ , and its average,  $\overline{\varepsilon_{art}}$ , for the two-dimensional,  $\gamma = 1/2$  semi-discretizations.

# Chapter 5

## Summary and Conclusions

This work constitutes a *first step* in a multi-methods comparison, and is intended to identify some of the relative strengths and weaknesses of multiple numerical methods in the context of advection-diffusion. This problem class has been selected because it can represent multiple limiting physical processes, and the solution methods for advection-diffusion can serve as the basic building-blocks required to assemble more complicated solution methods for nonlinear problems such as high-Reynolds number, time-dependent, viscous flow.

### Summary

As the starting point for a multi-methods analysis and comparison, we chose to apply Fourier analysis because it provides a general methodology that is capable of analyzing multiple methods in a single mathematical framework while providing a great deal of information and insight into each method. In this work, Fourier analysis has been used to investigate the following aspects of each numerical method:

- numerical dispersion, i.e., phase and group velocity errors,
- the spectral behavior of the apparent, i.e., discrete, diffusivity that is introduced by the spatial discretization and results in many schemes being under-diffusive at short-wavelengths,
- the limiting behavior of short wavelength information for both wave propagation and diffusion,
- the identification and characterization of artificial diffusivity via up-winding,

- grid bias errors in phase, group, discrete diffusivity and artificial diffusivity, and
- asymptotic convergence properties.

The results of this *first step* show that there are a number of competing methods that are all of second-order accuracy or better and that should perform adequately in the hands of an experienced analyst. While there is no *single* best method, there are at least two methods that are clearly the worst. The first-order upwind method is excessively diffusive, and the second-order upwind method is extremely dispersive.

The Galerkin finite element method and its streamline-upwind derivatives exhibit remarkable super-convergent behavior in terms of dispersive behavior, i.e., phase and group accuracy. The only other method considered that exhibited this behavior is the third-order upwind scheme. Analysis of several CVFEM methods and their streamline-upwind derivatives revealed that their behavior is strictly second-order in all of our metrics. While it appears that these methods yield good phase and group accuracy when the accuracy requirements are relaxed, the resolution requirements for an acceptable 1% error in phase and group is more than twice that of the finite element method in a one-dimensional sense (greater than a factor of eight in three dimensions).

The deleterious effects of ad-hoc mass-lumping was demonstrated (again) for the FEM and CVFEM formulations. In comparison, the FD and FVM formulations, by default, incorporate a diagonal mass matrix, i.e., they come equipped with a built-in lumped mass approximation in which the nodal time derivative are decoupled. In terms of advection-diffusion, the FD and FVM schemes represent the time-dependent terms by an equivalent lumped-capacitance. In contrast, the consistent mass matrix inherent in the FEM/CVFEM formulations represent this time-dependent terms by a distributed capacitance that more accurately reflects the physical situation in the continuum. As a consequence, the lumped-capacitance representation inherent in the FD and FVM schemes yield schemes that generally under perform in terms of phase and group speed relative to their consistent-mass FEM/CVFEM counterparts.

Several of the finite difference and finite volume methods show reasonable dispersion characteristics, however it should be noted that, except for the first-order upwind scheme, these methods all involve higher-order advection operators, i.e. they involve more than just the neighboring grid points. These methods are more difficult to deal with on unstructured meshes and many current implementations use extrapolation outside the control volume (e.g. Jessee and Fiveland [15]). The effect of this extrapolation on the resulting accuracy may be a concern and could be assessed using the methods



outlined in this report.

In terms of numerical performance for pure diffusion problems, the CVFEM scheme introduces minimal error and anisotropy in two dimensions. In contrast, the stabilized schemes, FEM-SUPG and CVFEM-SUCV, may be optimized for phase and group accuracy, but when tuned for phase accuracy, they do not perform well in terms of the discrete diffusivity, which exhibits significant anisotropic behavior. This reinforces the notion that there is no single best method that spans all problem classes.

## Conclusions

The results of this *first step* in a multi-methods comparison lead us to conclude that:

- There is no *single* best method, but there are a number of competing methods that are of second-order accuracy or better and that should perform adequately in the hands of an experienced analyst. However, the grid resolution requirements to attain a certain level of error can be vastly different.
- A single numerical method that can optimally solve all problem classes with equivalent accuracy and robustness does not exist in the set of methods considered, but the selection of an optimal numerical method must still be made based on the problem to be solved. The results presented here will hopefully provide some guidance in the selection process.
- The spatial coupling of time-derivatives yields super-convergent phase and group accuracy for the finite element methods, and as a general rule improves the phase and group accuracy of the CVPFEM methods, albeit without the super-convergent behavior.
- The 2-D dispersive properties of many of the methods may be characterized by a simple generalization relative to the corresponding 1-D behavior.
- At the hyperbolic limit, the accurate propagation of a signal depends on providing adequate resolution for all wavelengths present in the signals. Dispersive errors will occur for all of the methods considered here.
- Although not often discussed, accurate modeling of diffusion also requires providing adequate resolution for all wavelengths present in the signals. Many methods exhibit reduced apparent diffusivities for short-wavelength signals, i.e., near the grid Nyquist limit.
- The artificial viscosity, in general, damps the under-resolved parts of a signal – the specific spectral characteristics have been shown to be a function of the method. All of the higher-order methods tend to introduce minimal artificial diffusivity through the mid-range of the discrete spectrum with a peak occurring just before the Nyquist limit for the grid. This behavior may be optimized to deliver specific band-pass properties that match the dispersive properties of the method. However, to our knowledge, this type of matching has not been performed.

## Future Directions

The work presented here constitutes a first step in a multi-methods comparison intended to identify the relative strengths and weaknesses of multiple numerical methods in the context of advective-diffusive processes. The focus for this work has been on characterizing the numerical artifacts associated with spatial discretization in a spectral sense. There are, of course, other numerical methods, and analysis techniques that can be applied to a multi-methods comparison. From our perspective the logical next steps in this work should proceed as follows.

1. Extend the analysis techniques presented here to treat non-linear advection methods. This step should consider the very important total-variation diminishing (TVD) properties of non-linear methods and the concomitant introduction of an artificial diffusivity that varies in space and time. Initial efforts in this direction suggest that it is possible to bound the phase and group speed, discrete diffusivity, and artificial diffusivity in terms of flux limiters and their operating range.
2. Extend the analysis presented here to consider the fully-discrete situation for a range of time-integration methods. Gresho and Sani[12] (see section 2.7.6) present a prototypical study of fully-discrete methods, albeit a subset of the methods considered here. In addition to characterizing the fully-discrete dispersive errors, consideration of the algorithmic damping associated with time-integration schemes should be considered in conjunction with the artificial diffusivity associated with the spatial discretization. As with this work, a Fourier analysis would provide the means for placing all methods on a relatively equal footing.
3. A carefully designed suite of computational experiments should be assembled and used to assess specific methods selected based on the outcome of steps 1 and 2. This phase of the effort would focus on the development of an archival database of results that would be accessible via the world-wide web. This idea is not new, and a good prototype for this may be found in the work reported by Baptista, et al. [3]. It is anticipated that this phase of the effort could draw on results provided by a large number of researchers with appropriate quality-control measures for submitted results.



# Appendix A

## Operator Stencils

The semi-discrete equations for each of the methods considered in this work are presented here with the advection operators decomposed into symmetric and skew-symmetric components where appropriate. Each of the semi-discrete equations is presented in a stencil form based on the grid layout shown in Figure 2.2.

The generic form for the semi-discrete equations is

$$\mathbf{M}\dot{T} + \mathbf{A}_x(u)T + \mathbf{A}_y(v)T + \mathbf{K}T = 0. \quad (\text{A.1})$$

For each operator in the semi-discrete equation, the ‘stencil’ entries multiply their respective  $(m, n)$  field variables, e.g., for a generic operator A,

$$A = \begin{bmatrix} (m-2, n+2) & (m-1, n+2) & (m, n+2) & (m+1, n+2) & (m+2, n+2) \\ (m-2, n+1) & (m-1, n+1) & (m, n+1) & (m+1, n+1) & (m+2, n+1) \\ (m-2, n) & (m-1, n) & (m, n) & (m+1, n) & (m+2, n) \\ (m-2, n-1) & (m-1, n-1) & (m, n-1) & (m+1, n-1) & (m+2, n-1) \\ (m-2, n-2) & (m-1, n-2) & (m, n-2) & (m+1, n-2) & (m+2, n-2) \end{bmatrix}. \quad (\text{A.2})$$

### A.1 First-Order Upwind (FOU)

$$\begin{aligned} \Delta x \Delta y \begin{bmatrix} 0 & 0 & 0 \\ 0 & 1 & 0 \\ 0 & 0 & 0 \end{bmatrix} \dot{T} + u \Delta y \begin{bmatrix} 0 & 0 & 0 \\ -1 & 1 & 0 \\ 0 & 0 & 0 \end{bmatrix} T + v \Delta x \begin{bmatrix} 0 & 0 & 0 \\ 0 & 1 & 0 \\ 0 & -1 & 0 \end{bmatrix} T \\ + \alpha \begin{bmatrix} 0 & \frac{\Delta x}{\Delta y} & 0 \\ \frac{\Delta y}{\Delta x} & -2 \left( \frac{\Delta y}{\Delta x} + \frac{\Delta x}{\Delta y} \right) & \frac{\Delta y}{\Delta x} \\ 0 & \frac{\Delta x}{\Delta y} & 0 \end{bmatrix} T = 0. \end{aligned} \quad (\text{A.3})$$

This equation represents the stencil for the FOU method in the form presented in Eq. (A.2). The first term represents the discrete mass matrix operator, the next two terms are the  $x$ - and  $y$ -components of the advection operator, and the last term is the stencil for the discrete representation of diffusion. It is illustrative to decompose the advection operator into symmetric and skew-symmetric operators; the former represents the artificial diffusivity in the method. The symmetric and skew-symmetric portions of the first-order upwind advection operator are,

$$\mathbf{A}_x = u\Delta y \begin{bmatrix} 0 & 0 & 0 \\ -1/2 & 1 & -1/2 \\ 0 & 0 & 0 \end{bmatrix} + u\Delta y \begin{bmatrix} 0 & 0 & 0 \\ -1/2 & 0 & 1/2 \\ 0 & 0 & 0 \end{bmatrix} \quad (\text{A.4})$$

for the x-coordinate operator, and,

$$\mathbf{A}_y = v\Delta x \begin{bmatrix} 0 & -1/2 & 0 \\ 0 & 1 & 0 \\ 0 & -1/2 & 0 \end{bmatrix} + v\Delta x \begin{bmatrix} 0 & 1/2 & 0 \\ 0 & 0 & 0 \\ 0 & -1/2 & 0 \end{bmatrix} \quad (\text{A.5})$$

for the y-coordinate operator. Clearly, the first stencil on the RHS of each component equation is the symmetric contribution, and if the two symmetric components are summed with the diffusion operator, the result is the classical expression for artificial diffusivity for the first-order upwind scheme, with the form  $\alpha_{art,x} \sim u\Delta x$  and  $\alpha_{art,y} \sim v\Delta y$ .

## A.2 Second-Order Central Difference (CD)

$$\begin{aligned} \Delta x \Delta y \begin{bmatrix} 0 & 0 & 0 \\ 0 & 1 & 0 \\ 0 & 0 & 0 \end{bmatrix} \dot{T} + u\Delta y \begin{bmatrix} 0 & 0 & 0 \\ -1/2 & 0 & 1/2 \\ 0 & 0 & 0 \end{bmatrix} T + v\Delta x \begin{bmatrix} 0 & 1/2 & 0 \\ 0 & 0 & 0 \\ 0 & -1/2 & 0 \end{bmatrix} T \\ + \alpha \begin{bmatrix} 0 & \frac{\Delta x}{\Delta y} & 0 \\ \frac{\Delta y}{\Delta x} & -2 \left( \frac{\Delta y}{\Delta x} + \frac{\Delta x}{\Delta y} \right) & \frac{\Delta y}{\Delta x} \\ 0 & \frac{\Delta x}{\Delta y} & 0 \end{bmatrix} T = 0. \end{aligned} \quad (\text{A.6})$$

The components of the skew-symmetric advective operator are the second and third terms. There is no symmetric portion to this advective operator and hence no artificial diffusion in this method.

We also consider an *ad hoc* version of this scheme, referred to as a centered difference method with consistent mass (CD- $\mathbf{M}_c$ ), in which the lumped mass

term in the foregoing equation is replaced with the consistent mass matrix from CVFEM:

$$\frac{\Delta x \Delta y}{64} \begin{bmatrix} 1 & 6 & 1 \\ 6 & 36 & 6 \\ 1 & 6 & 1 \end{bmatrix} \dot{T} \quad (\text{A.7})$$

This scheme is *ad-hoc* because the spatial representation of the time derivative term is different from that for the advective and diffusive terms in order to arrive at this form.

### A.3 Second-Order Upwind (SOU)

$$\begin{aligned} \Delta x \Delta y \mathbf{M}_{\text{LM}} \dot{T} + \frac{u \Delta y}{2} \begin{bmatrix} 0 & 0 & 0 & 0 & 0 \\ 0 & 0 & 0 & 0 & 0 \\ 1 & -4 & 3 & 0 & 0 \\ 0 & 0 & 0 & 0 & 0 \\ 0 & 0 & 0 & 0 & 0 \end{bmatrix} T + \frac{v \Delta x}{2} \begin{bmatrix} 0 & 0 & 0 & 0 & 0 \\ 0 & 0 & 0 & 0 & 0 \\ 0 & 0 & 3 & 0 & 0 \\ 0 & 0 & -4 & 0 & 0 \\ 0 & 0 & 1 & 0 & 0 \end{bmatrix} T \\ + \alpha \mathbf{K}_{\text{CD}} T = 0, \end{aligned} \quad (\text{A.8})$$

where  $\mathbf{M}_{\text{LM}}$  is the lumped mass operator,

$$\begin{bmatrix} 0 & 0 & 0 \\ 0 & 1 & 0 \\ 0 & 0 & 0 \end{bmatrix} \quad (\text{A.9})$$

and  $\mathbf{K}_{\text{CD}}$  denotes the 5-pt central difference stencil for the diffusion operator, given by the last operator in the FOU stencil, Eq. (A.3). The symmetric and skew-symmetric portions of the second-order upwind advection operator are,

$$\mathbf{A}_{\text{x}} = \frac{u \Delta y}{2} \begin{bmatrix} 0 & 0 & 0 & 0 & 0 \\ 0 & 0 & 0 & 0 & 0 \\ 1/2 & -2 & 3 & -2 & 1/2 \\ 0 & 0 & 0 & 0 & 0 \\ 0 & 0 & 0 & 0 & 0 \end{bmatrix} + \frac{u \Delta y}{2} \begin{bmatrix} 0 & 0 & 0 & 0 & 0 \\ 0 & 0 & 0 & 0 & 0 \\ 1/2 & -2 & 0 & 2 & -1/2 \\ 0 & 0 & 0 & 0 & 0 \\ 0 & 0 & 0 & 0 & 0 \end{bmatrix} \quad (\text{A.10})$$

and,

$$\mathbf{A}_{\text{y}} = \frac{v \Delta x}{2} \begin{bmatrix} 0 & 0 & 1/2 & 0 & 0 \\ 0 & 0 & -2 & 0 & 0 \\ 0 & 0 & 3 & 0 & 0 \\ 0 & 0 & -2 & 0 & 0 \\ 0 & 0 & 1/2 & 0 & 0 \end{bmatrix} + \frac{v \Delta x}{2} \begin{bmatrix} 0 & 0 & -1/2 & 0 & 0 \\ 0 & 0 & 2 & 0 & 0 \\ 0 & 0 & 0 & 0 & 0 \\ 0 & 0 & -2 & 0 & 0 \\ 0 & 0 & 1/2 & 0 & 0 \end{bmatrix} \quad (\text{A.11})$$

for the  $x$ - and  $y$ -components, respectively.

## A.4 Third-Order Upwind (TOU)

$$\Delta x \Delta y \mathbf{M}_{\text{LM}} \dot{T} + \frac{u \Delta y}{12} \begin{bmatrix} 0 & 0 & 0 & 0 & 0 \\ 0 & 0 & 0 & 0 & 0 \\ 2 & -12 & 6 & 4 & 0 \\ 0 & 0 & 0 & 0 & 0 \\ 0 & 0 & 0 & 0 & 0 \end{bmatrix} T + \frac{v \Delta x}{12} \begin{bmatrix} 0 & 0 & 0 & 0 & 0 \\ 0 & 0 & 4 & 0 & 0 \\ 0 & 0 & 6 & 0 & 0 \\ 0 & 0 & -12 & 0 & 0 \\ 0 & 0 & 2 & 0 & 0 \end{bmatrix} T$$

$$+ \alpha \mathbf{K}_{\text{CD}} T = 0, \quad (\text{A.12})$$

The symmetric and skew-symmetric portions of the third-order upwind-biased scheme are,

$$\mathbf{A}_{\text{x}} = \frac{u \Delta y}{12} \begin{bmatrix} 0 & 0 & 0 & 0 & 0 \\ 0 & 0 & 0 & 0 & 0 \\ 1 & -4 & 6 & -4 & 1 \\ 0 & 0 & 0 & 0 & 0 \\ 0 & 0 & 0 & 0 & 0 \end{bmatrix} + \frac{u \Delta y}{12} \begin{bmatrix} 0 & 0 & 0 & 0 & 0 \\ 0 & 0 & 0 & 0 & 0 \\ 1 & -8 & 0 & 8 & -1 \\ 0 & 0 & 0 & 0 & 0 \\ 0 & 0 & 0 & 0 & 0 \end{bmatrix} \quad (\text{A.13})$$

and,

$$\mathbf{A}_{\text{y}} = \frac{v \Delta x}{12} \begin{bmatrix} 0 & 0 & 1 & 0 & 0 \\ 0 & 0 & -4 & 0 & 0 \\ 0 & 0 & 6 & 0 & 0 \\ 0 & 0 & -4 & 0 & 0 \\ 0 & 0 & 1 & 0 & 0 \end{bmatrix} + \frac{v \Delta x}{12} \begin{bmatrix} 0 & 0 & -1 & 0 & 0 \\ 0 & 0 & 8 & 0 & 0 \\ 0 & 0 & 0 & 0 & 0 \\ 0 & 0 & -8 & 0 & 0 \\ 0 & 0 & 1 & 0 & 0 \end{bmatrix} \quad (\text{A.14})$$

for the  $x$ - and  $y$ -components, respectively.

## A.5 Fromm's Method

$$\Delta x \Delta y \mathbf{M}_{\text{LM}} \dot{T} + \frac{u \Delta y}{4} \begin{bmatrix} 0 & 0 & 0 & 0 & 0 \\ 0 & 0 & 0 & 0 & 0 \\ 1 & -5 & 3 & 1 & 0 \\ 0 & 0 & 0 & 0 & 0 \\ 0 & 0 & 0 & 0 & 0 \end{bmatrix} T + \frac{v \Delta x}{4} \begin{bmatrix} 0 & 0 & 0 & 0 & 0 \\ 0 & 0 & 1 & 0 & 0 \\ 0 & 0 & 3 & 0 & 0 \\ 0 & 0 & -5 & 0 & 0 \\ 0 & 0 & 1 & 0 & 0 \end{bmatrix} T$$

$$+ \alpha \mathbf{K}_{\text{CD}} T = 0, \quad (\text{A.15})$$



The symmetric and skew-symmetric portions of the advection operator in the Fromm upwind-biased scheme are,

$$\mathbf{A}_x = \frac{u\Delta y}{4} \begin{bmatrix} 0 & 0 & 0 & 0 & 0 \\ 0 & 0 & 0 & 0 & 0 \\ 1/2 & -2 & 3 & -2 & 1/2 \\ 0 & 0 & 0 & 0 & 0 \\ 0 & 0 & 0 & 0 & 0 \end{bmatrix} + \frac{u\Delta y}{4} \begin{bmatrix} 0 & 0 & 0 & 0 & 0 \\ 0 & 0 & 0 & 0 & 0 \\ 1/2 & -3 & 0 & 3 & -1/2 \\ 0 & 0 & 0 & 0 & 0 \\ 0 & 0 & 0 & 0 & 0 \end{bmatrix} \quad (\text{A.16})$$

and,

$$\mathbf{A}_y = \frac{v\Delta x}{4} \begin{bmatrix} 0 & 0 & 1/2 & 0 & 0 \\ 0 & 0 & -2 & 0 & 0 \\ 0 & 0 & 3 & 0 & 0 \\ 0 & 0 & -2 & 0 & 0 \\ 0 & 0 & 1/2 & 0 & 0 \end{bmatrix} + \frac{c_y\Delta x}{4} \begin{bmatrix} 0 & 0 & -1/2 & 0 & 0 \\ 0 & 0 & 3 & 0 & 0 \\ 0 & 0 & 0 & 0 & 0 \\ 0 & 0 & -3 & 0 & 0 \\ 0 & 0 & 1/2 & 0 & 0 \end{bmatrix} \quad (\text{A.17})$$

for the  $x$ - and  $y$ -components, respectively.

## A.6 QUICK

$$\Delta x \Delta y \mathbf{M}_{\text{LM}} \dot{T} + \frac{u\Delta y}{8} \begin{bmatrix} 0 & 0 & 0 & 0 & 0 \\ 0 & 0 & 0 & 0 & 0 \\ 1 & -7 & 3 & 3 & 0 \\ 0 & 0 & 0 & 0 & 0 \\ 0 & 0 & 0 & 0 & 0 \end{bmatrix} T + \frac{v\Delta x}{8} \begin{bmatrix} 0 & 0 & 0 & 0 & 0 \\ 0 & 0 & 3 & 0 & 0 \\ 0 & 0 & 3 & 0 & 0 \\ 0 & 0 & -7 & 0 & 0 \\ 0 & 0 & 1 & 0 & 0 \end{bmatrix} T \quad (\text{A.18})$$

$$+ \alpha \mathbf{K}_{\text{CD}} T = 0,$$

The symmetric and skew-symmetric portions of the advection operator in the QUICK scheme are,

$$\mathbf{A}_x = \frac{u\Delta y}{8} \begin{bmatrix} 0 & 0 & 0 & 0 & 0 \\ 0 & 0 & 0 & 0 & 0 \\ 1/2 & -2 & 3 & -2 & 1/2 \\ 0 & 0 & 0 & 0 & 0 \\ 0 & 0 & 0 & 0 & 0 \end{bmatrix} + \frac{u\Delta y}{8} \begin{bmatrix} 0 & 0 & 0 & 0 & 0 \\ 0 & 0 & 0 & 0 & 0 \\ 1/2 & -5 & 0 & 5 & -1/2 \\ 0 & 0 & 0 & 0 & 0 \\ 0 & 0 & 0 & 0 & 0 \end{bmatrix} \quad (\text{A.19})$$

and,

$$\mathbf{A}_y = \frac{v\Delta x}{8} \begin{bmatrix} 0 & 0 & 1/2 & 0 & 0 \\ 0 & 0 & -2 & 0 & 0 \\ 0 & 0 & 3 & 0 & 0 \\ 0 & 0 & -2 & 0 & 0 \\ 0 & 0 & 1/2 & 0 & 0 \end{bmatrix} + \frac{v\Delta x}{8} \begin{bmatrix} 0 & 0 & -1/2 & 0 & 0 \\ 0 & 0 & 5 & 0 & 0 \\ 0 & 0 & 0 & 0 & 0 \\ 0 & 0 & -5 & 0 & 0 \\ 0 & 0 & 1/2 & 0 & 0 \end{bmatrix} \quad (\text{A.20})$$

for the  $x$ - and  $y$ -components, respectively.

## A.7 Node Centered Finite Volume with Least Squares Gradient Reconstruction (LSR)

Two methods that result from applying an unweighted least squares gradient reconstruction scheme were introduced in Section (2.3). The stencil for the LSR(-1) ( $\phi = 1$  and  $\kappa = -1$ ) is given by,

$$\Delta x \Delta y \mathbf{M}_{\text{LM}} \dot{T} + \frac{u\Delta y}{6} \begin{bmatrix} 0 & 0 & 0 & 0 & 0 \\ 1 & -1 & -1 & 1 & 0 \\ 1 & -10 & 11 & -2 & 0 \\ 1 & -1 & -1 & 1 & 0 \\ 0 & 0 & 0 & 0 & 0 \end{bmatrix} T + \frac{v\Delta x}{6} \begin{bmatrix} 0 & 0 & 0 & 0 & 0 \\ 0 & 1 & -2 & 1 & 0 \\ 0 & -1 & 11 & -1 & 0 \\ 0 & -1 & -10 & -1 & 0 \\ 0 & 1 & 1 & 1 & 0 \end{bmatrix} T + \alpha \mathbf{K}_{\text{CD}} T = 0. \quad (\text{A.21})$$

The symmetric and skew-symmetric portions of the LSR(-1) scheme are,

$$\mathbf{A}_x = \frac{u\Delta y}{6} \begin{bmatrix} 0 & 0 & 0 & 0 & 0 \\ 1/2 & 0 & -1 & 0 & 1/2 \\ 1/2 & -6 & 11 & -6 & 1/2 \\ 1/2 & 0 & -1 & 0 & 1/2 \\ 0 & 0 & 0 & 0 & 0 \end{bmatrix} + \frac{u\Delta y}{6} \begin{bmatrix} 0 & 0 & 0 & 0 & 0 \\ 1/2 & -1 & 0 & 1 & -1/2 \\ 1/2 & -4 & 0 & 4 & -1/2 \\ 1/2 & -1 & 0 & 1 & -1/2 \\ 0 & 0 & 0 & 0 & 0 \end{bmatrix} \quad (\text{A.22})$$

and,

$$\mathbf{A}_y = \frac{v\Delta x}{6} \begin{bmatrix} 0 & 1/2 & 1/2 & 1/2 & 0 \\ 0 & 0 & -6 & 0 & 0 \\ 0 & -1 & 11 & -1 & 0 \\ 0 & 0 & -6 & 0 & 0 \\ 0 & 1/2 & 1/2 & 1/2 & 0 \end{bmatrix} + \frac{v\Delta x}{6} \begin{bmatrix} 0 & -1/2 & -1/2 & -1/2 & 0 \\ 0 & 1 & 4 & 1 & 0 \\ 0 & 0 & 0 & 0 & 0 \\ 0 & -1 & -4 & -1 & 0 \\ 0 & 1/2 & 1/2 & 1/2 & 0 \end{bmatrix} \quad (\text{A.23})$$

The stencil for the LSR(0) ( $\phi = 1$  and  $\kappa = 0$ ) scheme is given by,

$$\Delta x \Delta y \mathbf{M}_{\text{LM}} \dot{T} + \frac{u \Delta y}{12} \begin{bmatrix} 0 & 0 & 0 & 0 & 0 \\ 1 & -1 & -1 & 1 & 0 \\ 1 & -13 & 11 & 1 & 0 \\ 1 & -1 & -1 & 1 & 0 \\ 0 & 0 & 0 & 0 & 0 \end{bmatrix} T + \frac{v \Delta x}{12} \begin{bmatrix} 0 & 0 & 0 & 0 & 0 \\ 0 & 1 & 1 & 1 & 0 \\ 0 & -1 & 11 & -1 & 0 \\ 0 & -1 & -13 & -1 & 0 \\ 0 & 1 & 1 & 1 & 0 \end{bmatrix} T$$

$$+ \alpha \mathbf{K}_{\text{CD}} T = 0. \quad (\text{A.24})$$

The symmetric and skew-symmetric portions of the LSR(0) scheme are,

$$\mathbf{A}_{\mathbf{x}} = \frac{u \Delta y}{12} \begin{bmatrix} 0 & 0 & 0 & 0 & 0 \\ 1/2 & 0 & -1 & 0 & 1/2 \\ 1/2 & -6 & 11 & -6 & 1/2 \\ 1/2 & 0 & -1 & 0 & 1/2 \\ 0 & 0 & 0 & 0 & 0 \end{bmatrix} + \frac{u \Delta y}{12} \begin{bmatrix} 0 & 0 & 0 & 0 & 0 \\ 1/2 & -1 & 0 & 1 & -1/2 \\ 1/2 & -7 & 0 & 7 & -1/2 \\ 1/2 & -1 & 0 & 1 & -1/2 \\ 0 & 0 & 0 & 0 & 0 \end{bmatrix} \quad (\text{A.25})$$

and,

$$\mathbf{A}_{\mathbf{y}} = \frac{v \Delta x}{12} \begin{bmatrix} 0 & 1/2 & 1/2 & 1/2 & 0 \\ 0 & 0 & -6 & 0 & 0 \\ 0 & -1 & 11 & -1 & 0 \\ 0 & 0 & -6 & 0 & 0 \\ 0 & 1/2 & 1/2 & 1/2 & 0 \end{bmatrix} + \frac{v \Delta x}{12} \begin{bmatrix} 0 & -1/2 & -1/2 & -1/2 & 0 \\ 0 & 1 & 7 & 1 & 0 \\ 0 & 0 & 0 & 0 & 0 \\ 0 & -1 & -7 & -1 & 0 \\ 0 & 1/2 & 1/2 & 1/2 & 0 \end{bmatrix} \quad (\text{A.26})$$

## A.8 Galerkin Finite Element Method (FEM)

The full stencil for the Galerkin Finite Element Method (FEM) reads:

$$\frac{\Delta x \Delta y}{36} \begin{bmatrix} 1 & 4 & 1 \\ 4 & 16 & 4 \\ 1 & 4 & 1 \end{bmatrix} \dot{T} + \frac{u \Delta y}{12} \begin{bmatrix} -1 & 0 & 1 \\ -4 & 0 & 4 \\ -1 & 0 & 1 \end{bmatrix} T + \frac{v \Delta x}{12} \begin{bmatrix} 1 & 4 & 1 \\ 0 & 0 & 0 \\ -1 & -4 & -1 \end{bmatrix} T$$

$$= \frac{\alpha}{6} \begin{bmatrix} \frac{\Delta y}{\Delta x} + \frac{\Delta x}{\Delta y} & 4 \frac{\Delta x}{\Delta y} - 2 \frac{\Delta y}{\Delta x} & \frac{\Delta y}{\Delta x} + \frac{\Delta x}{\Delta y} \\ 4 \frac{\Delta y}{\Delta x} - 2 \frac{\Delta x}{\Delta y} & -8 \left( \frac{\Delta y}{\Delta x} + \frac{\Delta x}{\Delta y} \right) & 4 \frac{\Delta y}{\Delta x} - 2 \frac{\Delta x}{\Delta y} \\ \frac{\Delta y}{\Delta x} + \frac{\Delta x}{\Delta y} & 4 \frac{\Delta x}{\Delta y} - 2 \frac{\Delta y}{\Delta x} & \frac{\Delta y}{\Delta x} + \frac{\Delta x}{\Delta y} \end{bmatrix} T \quad (\text{A.27})$$

The components of the skew-symmetric portion of the advective operator are the second and third terms; there is no symmetric portion to this operator.

## A.9 Finite Element Method with SUPG (FEM-SUPG)

The stencil for the Stream-Line Upwind Petrov-Galerkin (SUPG) method contains a modified mass matrix and an artificial diffusion term,

$$\begin{aligned}
& \frac{\Delta x \Delta y}{36} \begin{bmatrix} 1 & 4 & 1 \\ 4 & 16 & 4 \\ 1 & 4 & 1 \end{bmatrix} \dot{T} + \tau \frac{u \Delta y}{12} \begin{bmatrix} 1 & 0 & -1 \\ 4 & 0 & -4 \\ 1 & 0 & -1 \end{bmatrix} \dot{T} + \tau \frac{v \Delta x}{12} \begin{bmatrix} -1 & -4 & -1 \\ 0 & 0 & 0 \\ 1 & 4 & 1 \end{bmatrix} \dot{T} \\
& + \frac{u \Delta y}{12} \begin{bmatrix} -1 & 0 & 1 \\ -4 & 0 & 4 \\ -1 & 0 & 1 \end{bmatrix} T + \frac{v \Delta x}{12} \begin{bmatrix} 1 & 4 & 1 \\ 0 & 0 & 0 \\ -1 & -4 & -1 \end{bmatrix} T \\
& - \frac{\tau}{6} \begin{bmatrix} u^2 \frac{\Delta y}{\Delta x} - 3uv + v^2 \frac{\Delta x}{\Delta y} & 4v^2 \frac{\Delta x}{\Delta y} - 2u^2 \frac{\Delta y}{\Delta x} & u^2 \frac{\Delta y}{\Delta x} + 3uv + v^2 \frac{\Delta x}{\Delta y} \\ 4u^2 \frac{\Delta y}{\Delta x} - 2v^2 \frac{\Delta x}{\Delta y} & -8 \left( u^2 \frac{\Delta y}{\Delta x} + v^2 \frac{\Delta x}{\Delta y} \right) & 4u^2 \frac{\Delta y}{\Delta x} - 2v^2 \frac{\Delta x}{\Delta y} \\ u^2 \frac{\Delta y}{\Delta x} + 3uv + v^2 \frac{\Delta x}{\Delta y} & 4v^2 \frac{\Delta x}{\Delta y} - 2u^2 \frac{\Delta y}{\Delta x} & u^2 \frac{\Delta y}{\Delta x} - 3uv + v^2 \frac{\Delta x}{\Delta y} \end{bmatrix} T \\
& = \frac{\alpha}{6} \begin{bmatrix} \frac{\Delta y}{\Delta x} + \frac{\Delta x}{\Delta y} & 4 \frac{\Delta x}{\Delta y} - 2 \frac{\Delta y}{\Delta x} & \frac{\Delta y}{\Delta x} + \frac{\Delta x}{\Delta y} \\ 4 \frac{\Delta y}{\Delta x} - 2 \frac{\Delta x}{\Delta y} & -8 \left( \frac{\Delta y}{\Delta x} + \frac{\Delta x}{\Delta y} \right) & 4 \frac{\Delta y}{\Delta x} - 2 \frac{\Delta x}{\Delta y} \\ \frac{\Delta y}{\Delta x} + \frac{\Delta x}{\Delta y} & 4 \frac{\Delta x}{\Delta y} - 2 \frac{\Delta y}{\Delta x} & \frac{\Delta y}{\Delta x} + \frac{\Delta x}{\Delta y} \end{bmatrix} T \quad (\text{A.28})
\end{aligned}$$

where the two-dimensional version of the stability parameter ([5]) is

$$\tau = \beta \left( \frac{u \Delta x + v \Delta y}{u^2 + v^2} \right) \quad (\text{A.29})$$

for large  $\mathbf{P}_e$ . The  $\beta$  coefficient can be chosen to optimize the method with respect to its dispersive characteristics. The components of the skew-symmetric portions of the advective operator are given by the 4th and 5th terms, while the symmetric portion is the 6th term, which can also be written as:

$$-\frac{1}{6} \left( u^2 \frac{\Delta y}{\Delta x} \begin{bmatrix} 1 & -2 & 1 \\ 4 & -8 & 4 \\ 1 & -2 & 1 \end{bmatrix} + 3uv \begin{bmatrix} -1 & 0 & 1 \\ 0 & 0 & 0 \\ 1 & 0 & -1 \end{bmatrix} + v^2 \frac{\Delta x}{\Delta y} \begin{bmatrix} 1 & 4 & 1 \\ -2 & -8 & -2 \\ 1 & 4 & 1 \end{bmatrix} \right)$$

showing that the symmetric portion of the advective operator induced by SUPG contains a cross term and therefore cannot be resolved into  $x$ - and  $y$ -components as in the FVMs.

## A.10 Control Volume Finite Element Method (CVFEM)

The stencil for the Control Volume Finite Element Method reads:

$$\begin{aligned}
& \frac{\Delta x \Delta y}{64} \begin{bmatrix} 1 & 6 & 1 \\ 6 & 36 & 6 \\ 1 & 6 & 1 \end{bmatrix} \dot{T} + \frac{u \Delta y}{16} \begin{bmatrix} -1 & 0 & 1 \\ -6 & 0 & 6 \\ -1 & 0 & 1 \end{bmatrix} T + \frac{v \Delta x}{16} \begin{bmatrix} 1 & 6 & 1 \\ 0 & 0 & 0 \\ -1 & -6 & -1 \end{bmatrix} T \\
& = \frac{\alpha}{8} \begin{bmatrix} \frac{\Delta y}{\Delta x} + \frac{\Delta x}{\Delta y} & 6 \frac{\Delta x}{\Delta y} - 2 \frac{\Delta y}{\Delta x} & \frac{\Delta y}{\Delta x} + \frac{\Delta x}{\Delta y} \\ 6 \frac{\Delta y}{\Delta x} - 2 \frac{\Delta x}{\Delta y} & -12 \left( \frac{\Delta y}{\Delta x} + \frac{\Delta x}{\Delta y} \right) & 6 \frac{\Delta y}{\Delta x} - 2 \frac{\Delta x}{\Delta y} \\ \frac{\Delta y}{\Delta x} + \frac{\Delta x}{\Delta y} & 6 \frac{\Delta x}{\Delta y} - 2 \frac{\Delta y}{\Delta x} & \frac{\Delta y}{\Delta x} + \frac{\Delta x}{\Delta y} \end{bmatrix} T \quad (\text{A.30})
\end{aligned}$$

The advective operator contains only skew-symmetric components, given by the 2nd and 3rd terms in the equation.

## A.11 Control-Volume Finite Element Method with SUCV (CVFEM-SUCV)

The Stream-Line Upwind Control Volume (SUCV) method results in a scheme similar to SUPG:

$$\begin{aligned}
& \frac{\Delta x \Delta y}{64} \begin{bmatrix} 1 & 6 & 1 \\ 6 & 36 & 6 \\ 1 & 6 & 1 \end{bmatrix} \dot{T} + \tau \frac{u \Delta y}{16} \begin{bmatrix} 1 & 0 & -1 \\ 6 & 0 & -6 \\ 1 & 0 & -1 \end{bmatrix} \dot{T} + \tau \frac{v \Delta x}{16} \begin{bmatrix} -1 & -6 & -1 \\ 0 & 0 & 0 \\ 1 & 6 & 1 \end{bmatrix} \dot{T} \\
& + \frac{u \Delta y}{16} \begin{bmatrix} -1 & 0 & 1 \\ -6 & 0 & 6 \\ -1 & 0 & 1 \end{bmatrix} T + \frac{v \Delta x}{16} \begin{bmatrix} 1 & 6 & 1 \\ 0 & 0 & 0 \\ -1 & -6 & -1 \end{bmatrix} T \\
& - \frac{\tau}{8} \begin{bmatrix} u^2 \frac{\Delta y}{\Delta x} - 4uv + v^2 \frac{\Delta x}{\Delta y} & 6v^2 \frac{\Delta x}{\Delta y} - 2u^2 \frac{\Delta y}{\Delta x} & u^2 \frac{\Delta y}{\Delta x} + 4uv + v^2 \frac{\Delta x}{\Delta y} \\ 6u^2 \frac{\Delta y}{\Delta x} - 2v^2 \frac{\Delta x}{\Delta y} & -12 \left( u^2 \frac{\Delta y}{\Delta x} + v^2 \frac{\Delta x}{\Delta y} \right) & 6u^2 \frac{\Delta y}{\Delta x} - 2v^2 \frac{\Delta x}{\Delta y} \\ u^2 \frac{\Delta y}{\Delta x} + 4uv + v^2 \frac{\Delta x}{\Delta y} & 6v^2 \frac{\Delta x}{\Delta y} - 2u^2 \frac{\Delta y}{\Delta x} & u^2 \frac{\Delta y}{\Delta x} - 4uv + v^2 \frac{\Delta x}{\Delta y} \end{bmatrix} T \\
& = \frac{\alpha}{8} \begin{bmatrix} \frac{\Delta y}{\Delta x} + \frac{\Delta x}{\Delta y} & 6 \frac{\Delta x}{\Delta y} - 2 \frac{\Delta y}{\Delta x} & \frac{\Delta y}{\Delta x} + \frac{\Delta x}{\Delta y} \\ 6 \frac{\Delta y}{\Delta x} - 2 \frac{\Delta x}{\Delta y} & -12 \left( \frac{\Delta y}{\Delta x} + \frac{\Delta x}{\Delta y} \right) & 6 \frac{\Delta y}{\Delta x} - 2 \frac{\Delta x}{\Delta y} \\ \frac{\Delta y}{\Delta x} + \frac{\Delta x}{\Delta y} & 6 \frac{\Delta x}{\Delta y} - 2 \frac{\Delta y}{\Delta x} & \frac{\Delta y}{\Delta x} + \frac{\Delta x}{\Delta y} \end{bmatrix} T \quad (\text{A.31})
\end{aligned}$$

The skew-symmetric part of the advective operator remains the same as in CVFEM, while the symmetric portion, giving rise to artificial diffusion, is given by the 6th term in the foregoing formula. Similar to FEM, this term can be separated into three pieces, except the 4-8-4 columns and rows of SUPG go the 6-12-6, (with the same signs) in the SUCV.



# Bibliography

- [1] K. F. ALVIN AND K. C. PARK, *Frequency-window tailoring of finite element models for vibration and acoustics analysis*, in Structural Acoustics, AMD-Vol. 128, ASME, 1991, pp. 117–128.
- [2] W. K. ANDERSON AND D. L. BONHAUS, *An implicit upwind algorithm for computing turbulent flows on unstructured grids*, Computers and Fluids, 23 (1994), pp. 1–21.
- [3] A. M. BAPTISTA, E. E. ADAMS, AND P. GRESHO, *Benchmarks for the transport equation: the convection-diffusion equation and beyond*, Quantitative Skill Assessment for Coastal Ocean Models, 47 (1995), pp. 241–268.
- [4] T. BELYTSCHKO AND R. MULLEN, *On dispersive properties of finite element solutions*, in Modern Problems in Elastic Wave Propagation, J. Milovitz and J. D. Achenbach, eds., International Union of Theoretical and Applied Mechanics, John Wiley and Sons, 1978, pp. 67–82.
- [5] A. N. BROOKS AND T. J. R. HUGHES, *Streamline upwind/Petrov-Galerkin formulations for convection dominated flows with particular emphasis on the incompressible Navier-Stokes equations*, Computer Methods in Applied Mechanics and Engineering, 32 (1982), pp. 199–259.
- [6] M. A. CHRISTON, *The influence of the mass matrix on the dispersive nature of the semi-discrete, second-order wave equation*, Computer Methods in Applied Mechanics and Engineering, 173 (1999).
- [7] M. A. CHRISTON AND T. E. VOTH, *Results of von Neumann analyses for reproducing kernel semi-discretizations*, International Journal for Numerical Methods in Engineering, 47 (2000), pp. 1285–1301. (Invited paper from the Fourth World Congress on Computational Mechanics).
- [8] M. O. DEVILLE AND E. H. MUND, *Fourier analysis of finite element preconditioned collocation schemes*, SIAM Journal for Scientific and Statistical Computing, 13 (1992), pp. 596–610.

- [9] J. E. FROMM, *A method for reducing dispersion in convective difference schemes*, Journal of Computational Physics, 3 (1968), pp. 176–189.
- [10] P. M. GRESHO, S. T. CHAN, R. L. LEE, AND C. D. UPSON, *A modified finite element method for solving the time-dependent, incompressible Navier-Stokes equations. part 1: Theory*, International Journal for Numerical Methods in Fluids, 4 (1984), pp. 557–598.
- [11] P. M. GRESHO AND R. L. SANI, *Incompressible flow and the finite element method, advection-diffusion and isothermal laminar flow*, John Wiley & Sons, Chicester, England, 1998.
- [12] P. M. GRESHO, R. L. SANI, AND M. S. ENGELMAN, *Incompressible flow and the finite element method, Volume 1: Advection-Diffusion*, John Wiley & Sons, Chicester, England, 2000.
- [13] K. GROSH AND P. M. PINSKY, *Complex wave-number dispersion analysis of Galerkin and Galerkin least-squares methods for fluid-loaded plates*, Computer Methods in Applied Mechanics and Engineering, 113 (1994), pp. 67–98.
- [14] I. HARARI AND T. J. R. HUGHES, *Galerkin/least-squares finite element methods for the reduced wave equation with non-reflecting boundary conditions in unbounded domains*, Computer Methods in Applied Mechanics and Engineering, 98 (1992), pp. 411–454.
- [15] J. P. JESSEE AND W. A. FIVELAND, *A cell vertex algorithm for the incompressible Navier-Stokes equations on non-orthogonal grids*, International Journal for Numerical Methods in Fluids, 23 (1996), pp. 271–293.
- [16] S. KARNI, *On the group velocity of symmetric and upwind numerical schemes*, International Journal for Numerical Methods in Fluids, 18 (1994), pp. 1073–1081.
- [17] R. L. LEE, P. M. GRESHO, S. T. CHAN, R. L. SANI, AND M. J. P. CULLEN, *Conservation laws for primitive variable formulations of the incompressible flow equations using the Galerkin finite element method*, Tech. Rep. UCRL-82868, Lawrence Livermore National Laboratory, Livermore, California, May 1981.
- [18] B. P. LEONARD, *A stable and accurate convective modelling procedure based on quadratic upstream interpolation*, Computer Methods in Applied Mechanics and Engineering, 19 (1979), pp. 59–98.



- [19] R. MULLEN AND T. BELYTSCHKO, *Dispersion analysis of finite element semi-discretizations of the two-dimensional wave equation*, International Journal for Numerical Methods in Engineering, 18 (1982), pp. 1–29.
- [20] K. C. PARK AND D. L. FLAGGS, *A Fourier analysis of spurious mechanisms and locking in the finite element method*, Computer Methods in Applied Mechanics and Engineering, 46 (1984), pp. 65–81.
- [21] —, *A symbolic Fourier synthesis of a one-point integrated quadrilateral plate element*, Computer Methods in Applied Mechanics and Engineering, 48 (1985), pp. 203–236.
- [22] W. H. RAYMOND AND A. GARDNER, *Selective damping in a Galerkin method for solving wave problems with variable grids*, Monthly Weather Review, 104 (1976), pp. 1583–1590.
- [23] F. SHAKIB AND T. J. R. HUGHES, *A new finite element formulation for computational fluid dynamics: Ix. Fourier analysis of space-time Galerkin/least-squares algorithms*, Computer Methods in Applied Mechanics and Engineering, 87 (1991), pp. 35–58.
- [24] C. R. SWAMINATHAN AND V. R. VOLLER, *Streamline upwind scheme for control-volume finite elements, part 1. formulations*, Numerical Heat Transfer, Part B, 22 (1992), pp. 95–107.
- [25] —, *Streamline upwind scheme for control-volume finite elements, part 2. implementation and comparison with the supg finite-element scheme*, Numerical Heat Transfer, Part B, 22 (1992), pp. 109–124.
- [26] T. E. TEZDUYAR, *Stabilized Finite Element Formulations for Incompressible Flow Computations*, vol. 28, Academic Press, Inc., San Diego, California, 1992, pp. 1–44.
- [27] L. L. THOMPSON AND P. M. PINSKY, *Complex wavenumber Fourier analysis of the p-version finite element method*, Computational Mechanics, 13 (1994), pp. 255–275.
- [28] L. N. TREFETHEN, *Group velocity in finite difference schemes*, SIAM Review, 24 (1982), pp. 113–136.
- [29] B. VAN LEER, *Towards the ultimate conservative difference scheme. v. a second-order sequel to godunov's method*, Journal of Computational Physics, 32 (1979), pp. 101–136.
- [30] R. VICHNEVETSKY, *Wave propagation and reflection in irregular grid for hyperbolic equations*, Tech. Rep. MAE-1713, Department of Mechanical and Aerospace Engineering, Princeton University, July 1985.

- [31] —, *Wave propagation analysis of difference schemes for hyperbolic equations: a review*, International Journal for Numerical Methods in Fluids, 7 (1987), pp. 409–452.
- [32] —, *On wave propagation in almost periodic structures*, Applied Numerical Mathematics, 10 (1992), pp. 195–229.
- [33] R. VICHNEVETSKY AND J. B. BOWLES, *Fourier Analysis of Numerical Approximations of Hyperbolic Equations*, SIAM, Philadelphia, PA, 1982.
- [34] R. VICHNEVETSKY AND E. C. PARISER, *High order numerical Sommerfeld boundary conditions: theory and experiments*, Computers and Mathematics with Applications, 11 (1985), pp. 67–78.
- [35] R. VICHNEVETSKY AND F. D. SCHUTTER, *A frequency analysis of finite difference and finite element methods for initial value problems*, in AICA International Symposium on Computer Methods for Partial Differential Equations, Lehigh University, Bethlehem, Pennsylvania, June 1975, pp. 179–185.
- [36] R. VICHNEVETSKY AND A. W. TOMALESKY, *Spurious wave phenomena in numerical approximations of hyperbolic equations*, in Proceedings of the Fifth Annual Princeton Conference on Information Science and Systems, Princeton University, March 1971, pp. 357–363.
- [37] T. E. VOTH AND M. A. CHRISTON, *Discretization errors associated with reproducing kernel methods: One-dimensional domains*, Computer Methods in Applied Mechanics and Engineering, 190 (2001), pp. 2429–2446.

## External Distribution:

Prof. Ted Belytschko  
Mechanical Engineering Dept.  
Northwestern University  
2145 Sheridan Road  
Evanston, Illinois 60208-3111

Prof. Patrick J. Burns  
Mechanical Engineering Dept.  
Colorado State University  
Ft. Collins, CO 80523

Philip M. Gresho  
Lawrence Livermore National Laboratory  
P.O. Box 808, L-103  
Livermore, California 94551

Prof. Thomas J. R. Hughes  
TICAM  
ACE 6.412  
University of Texas  
Austin, TX 78712

Prof. G. F. Carey  
Aerospace Engr. Dept.  
WRW 301  
University of Texas  
Austin, TX 78712

Prof. Wing Kam Liu  
Mechanical Engineering Dept.  
Northwestern University  
2145 Sheridan Road  
Evanston, Illinois 60208-3111

Prof. Tayfun Tezduyar  
Dept. of Mechanical Engineering  
Rice University – MS 321  
6100 Main Street  
Houston, TX 77005-1892

Prof. Erik Thompson  
Civil Engineering Dept.  
Colorado State University  
Ft. Collins, CO 80523

Prof. Jiun-Shyan Chen  
Department of Mechanical Engineering  
The University of Iowa  
2133 Engineering Building  
Iowa City, Iowa 52242-1527

Farzin Shakib  
ACUSIM Software, Inc.  
14395 Saratoga Ave.

Suite 120  
Saratoga, CA 95070

Robert Ferencz  
Methods Development Group  
L-125  
Lawrence Livermore National Laboratory  
Livermore, California 94551

Greg Hulbert  
Mechanical Engineering  
Univ. of Michigan  
CoE/2250 CG Brown Lab  
2350 Hayward St.,  
Ann Arbor, MI 48109-2125

Jacob Fish  
Department of Civil Engineering  
Renselaer Polytechnic Institute  
Troy, NY 12180-3590

Prof. K. W. Morton  
Oxford University Computing Laboratory  
Wolfson Building  
Parks Road  
Oxford, OX1 3QD  
England

Kenneth E. Jansen  
Mechanical Engineering  
Renselaer Polytechnic Institute  
Troy, NY 12180-3590

Alvaro Coutinho  
COPPE/UFRJ  
Civil Engineering Dept.  
Federal University of Rio de Janeiro  
P.O. Box 68506  
CEP 21945-970  
Rio de Janeiro RJ Brazil

## Internal Distribution:

1	MS 0841	T. C. Bickel, 09100
1	MS 0824	A. C. Ratzel, 09110
1	MS 0847	H. S. Morgan, 09120
1	MS 0824	J. L. Moya, 09130
1	MS 0835	J. M. McGlaun, 09140
1	MS 0834	J. E. Johannes, 09114
1	MS 0836	E. S. Hertel, 09116
1	MS 0836	R. O. Griffith, 09117
1	MS 1135	L. A. Gritz, 09132
1	MS 0828	M. Pilch, 09133
1	MS 0835	S. N. Kempka, 09141
1	MS 0827	J. D. Zepper, 09143

1	MS 0321	W. J. Camp, 09200	1	MS 0835	R. J. Cochran, 09141
1	MS 0310	P. Yarrington, 09230	1	MS 0835	S. P. Domino, 09141
1	MS 0847	S. Mitchell, 09211	1	MS 0835	P. A. Sackinger, 09141
1	MS 1110	D. Womble, 9214	1	MS 0835	J. H. Strickland, 09141
1	MS 0819	E. Boucheron, 09231	1	MS 0835	S. R. Subia, 09141
1	MS 0820	P. Chavez, 09232	1	MS 0847	J. W. Swegle, 09142
1	MS 0316	S. Dosanjh, 09233	1	MS 0827	H. C. Edwards, 09143
1	MS 0316	J. Aidun, 9235	1	MS 0827	J. R. Stewart, 09143
			1	MS 9042	C. D. Moen, 08728
1	MS 1110	P. Bochev, 09214	1	MS 1186	T. A. Brunner, 01674
1	MS 1110	M. Heroux, 09214	1	MS 1186	T. A. Haill, 01674
1	MS 1110	R. Lehoucq, 09214	1	MS 1186	T. A. Mehlhorn, 01674
1	MS 1111	B. Hedrickson, 09226			
1	MS 0822	R. Haynes, 09227	1	MS 9018	Central Technical Files, 8945-1
1	MS 0819	W. Bohnhoff, 09231	2	MS 0899	Technical Library, 09616
1	MS 0819	K. Brown, 09231	1	MS 0612	Review & Approval Desk, 09612 for DOE/OSTI
1	MS 0819	K. Budge, 09231			
1	MS 0819	S. Burns, 09231			
1	MS 0819	D. Carroll, 09231			
10	MS 0819	M. Christon, 09231			
1	MS 0819	R. Drake, 09231			
1	MS 0819	C. Garasi, 09231			
1	MS 0819	D. Hensinger, 09231			
1	MS 0819	J. Robbins, 09231			
1	MS 0819	A. Robinson, 09231			
10	MS 0819	T. Voth, 09231			
1	MS 0819	M. Wong, 09231			
1	MS 0819	T. G. Trucano, 09211			
1	MS 0820	T. Bartel, 09232			
1	MS 0820	A. Farnsworth, 09232			
1	MS 0819	J. R. Weatherby, 09232			
1	MS 0316	P. Lin, 09233			
1	MS 1111	J. Shadid, 09233			
1	MS 1111	T. M. Smith, 09233			
1	MS 1110	W. Spotz, 9233			
1	MS 0316	H. Hjalmarson, 9235			
1	MS 0836	M. R. Baer, 09100			
1	MS 0826	D. K. Gartling, 09100			
1	MS 0834	T. A. Baer, 09114			
1	MS 0834	M. M. Hopkins, 09114			
10	MS 0834	M. J. Martinez, 09114			
1	MS 0834	H. K. Moffat, 09114			
1	MS 0834	R. R. Rao, 09114			
1	MS 0834	P. R. Schunk, 09114			
1	MS 0825	F. G. Blottner, 09115			
1	MS 0825	B. Hassan, 09115			
1	MS 0825	C. J. Roy, 09115			
1	MS 0847	S. W. Attaway, 09132			
1	MS 0828	B. F. Blackwell, 09133			
1	MS 0828	K. J. Dowding, 09133			
1	MS 0828	W. L. Oberkampf, 09133			
1	MS 0835	S. W. Bova, 09141			